Characterization and Imaging Diagnostics of Laser Induced Plasma from Solid Targets

Thesis submitted to

Cochin University of Science and Technology

in partial fulfillment of the requirements

for the degree of

Doctor of Philosophy

under the Faculty of Technology

Dann V J

Laser Division
International School of Photonics
Cochin University of Science and Technology
Cochin – 682 022, Kerala, India

October 2008

Characterization and Imaging Diagnostics of Laser Induced Plasma from Solid Targets
PhD thesis in the field of Laser Produced Plasma

Author

Dann V J
Research Fellow
International School of Photonics
Cochin University of Science and Technology
Cochin – 682 022, Kerala, India
email: dannvj@gmail.com

Research Advisors:

Dr. V P N Nampoori
Professor, International School of Photonics
Cochin University of Science and Technology
Cochin – 682 022, Kerala, India
email: nampoori@gmail.com

Dr. V M Nandakumaran
Professor, International School of Photonics
Cochin University of Science and Technology
Cochin – 682 022, Kerala, India
email: nandak@cusat.ac.in

Cochin University of Science and Technology
Cochin-682022, Kerala, India
www.photonics.cusat.edu

Front Cover: visualization of a thunderbolt.

October 2008

Dr. V P N Nampoori
Professor
International School of Photonics
Cochin University of Science and Technology
Cochin – 682 022

Certificate

Certified that the work presented in this thesis entitled *"***Characterization and Imaging Diagnostics of Laser Induced Plasma from Solid Targets***"* is based on the authentic record of research done by Dann V J under my guidance and supervision at the International School of Photonics, Cochin University of Science and Technology, Cochin – 682 022 and has not been included in any other thesis submitted for the award of any degree.

Cochin-22 Prof. V P N Nampoori

Date: 13th October 2008 (Supervising Guide)

Phone: +91 484 2575848. **Fax:** 0091-484-2576714. **Email:** nampoori@gmail.com

Declaration

I hereby declare that the work presented in this thesis entitled *"***Characterization and Imaging Diagnostics of Laser Induced Plasma from Solid Targets***"* is based on the original research work done by me under the supervision and guidance of ***Dr V P N Nampoori,*** *Professor,* International School of Photonics, Cochin University of Science and Technology, Cochin-682022 and has not been included in any other thesis submitted previously for the award of any degree.

Cochin – 22

Date:13th October 2008 Dann V J

Acknowledgements

First of all, let me bow my head before the Almighty God.

I am deeply indebted to *Dr V P N Nampoori*, Prof and Director ISP, who supervised my research programme and successfully guided me to the end of my work. I owe him a lot for all his kind care on me and his pleasing behaviour which made me to overcome the challenges during the period.

I am also thankful to *Dr V M Nandakumaran*, Professor, ISP, for his co-operation. I am grateful to *Prof C P Girijavallabhan*, former director of Centre of Excellence in Lasers and Optoelectronic Sciences, CUSAT, for the experimental guidance and fruitful discussions during my work. I sincerely acknowledge the invaluable helps rendered by *Prof P Radhakrishnan*, Professor, ISP. I wish to express my heartfelt thanks to *Mr. M. Kailasnath* , *Lecturer, ISP*.

It is with profound gratitude that I express my sincere thanks to *Dr Arun Anand*, (former Scientist at IPR, Gandhinagar who is presently working as a faculty member at Department of Applied Physics, MS University, Vadodara) for his motivation and support which ultimately led to the completion of my thesis. I sincerely thank him for his timely supports to explore the wonderful aspects of imaging diagnostics of plasma.

I am grateful to *Director, IPR, Gujarat*, for allowing me to pursue the dynamics of plasma expansion in magnetic field. I thank *Dr Ajaikumar* (Group Leader, LDG Group, IPR), *Dr R K Singh* and all the *members of Laser Diagnostics Group*.

The financial assistance from *CELOS, CUSAT*, funded by *UGC* India is greatly acknowledged. I thank all the *office staff* of *ISP and CELOS* for their help and encouragement.

I remember with immense gratitude, the helps rendered by *Dr Bindhu Krishnan*, (former scientist, C-MET, Thrissur) and *Dr Jaimon Yohannan* (post doctoral research fellow of CSIR, at the Department of Electronics, CUSAT) in preparing target materials for my experiments.

I am glad to think about my loving friends at ISP, *Manu Punnen John, Dr Rajesh Mandamparambil, Lyjo K Joseph, Thomas K J, Jijo P U, Sajeev D and Dr Rajesh S.*

My sincere thanks to *Prabathan P, Vinu V Namboodiri, Litty Mathew Irimpan, Sheeba M, Parvathi M R, Jayasree teacher, Rev. Sr. Dr. Ritty J Nedumpara, Dr Pramod Gopinath, Dr Deepthi A*, Dr Santhi A and *Mrs. Saritha M* for their help. *Sony George* need a special mention since he was always very supportive.

During the final days of my work, I was in the company of a group of junior members at ISP. I thank *Muralidharan, Mathew, Linesh, Sudheesh, Tintu, Jinesh, Nithyaja, Sithara, Sreelekha, Vasuja and Misha*, for their pleasant appearances and wish them all, a bright future.

I want to specially mention the support from the *authorities of Department of Collegiate Education, Kerala, Principal* and *Staff members of Government College, Kattappana* and *Government Polytechnic College, Kottayam*, at the final stages of my work. I was always encouraged by the kind consideration of my colleagues, *Dr Seno Jose, Mr. Madhavan Namboodhiri and Mr. A K Sadanandan at Government College, Kottayam.*

I have no words to express my gratitude to *Dr Thomas Lee S* and *Manoj V Mathew* for their encouragement and frank support during the initial stages of my work.

I thank *V Subramanyan Namboodiri*, research student of Department of Physics, for designing the cover page of the thesis.

I extend my heartfelt gratitude to *my parents*, who believed in me and patiently guided me to the right decisions. I thank my dear wife, *Tina* for her constant encouragement and co-operation during the tiresome moments of my research period.

Cochin, 682 022

October 2008 Dann V J

Preface

The interaction of laser light with materials and the properties of the plasma produced by focusing high peak power laser radiation onto a solid target is still a developing area in basic science, engineering and material processing technology. Studies in this direction have gained further importance due to recent discoveries related to tabletop particle accelerators. In-depth theoretical and experimental investigations are essential to obtain detailed knowledge related to physical processes involved in the light-matter interactions leading to plasma generation. Moreover, since the thermo-physical properties of solid matter are fairly well known, numerical models have been proposed by several groups and compared the results with experimental data. Experimental studies related to laser induced plasma (LIP) have been carried out by employing investigation techniques of atomic and molecular physics such as optical emission and absorption spectroscopy, mass spectrometry, time-of-flight, laser induced fluorescence and charge collection measurements. Fast photographic techniques, holographic interferometry and different methods of tomographic reconstructions have also been used to study LIP. The proposed thesis in seven chapters reports the studies on spectral characterization and diagnostics of LIP from a few metal oxide targets. Time and space resolved spectroscopic methods and electrical characterization techniques are applied to LIP from solid targets in magnetic field as well. Tomographic projection methods and digital holographic interferometry (DHI) are employed for diagnostic imaging of plasma cross sections.

Chapter 1 contains a brief review of the laser-plasma interactions and numerical modeling. The laser pulse duration is an important parameter describing its interaction with the material as well as with the plasma. Femtosecond laser beams can induce promising properties which might allow analytical improvements of nanosecond-laser induced breakdown spectroscopy (ns-LIBS). A literature survey on

the plasma emissions induced by nanosecond and ultra-short laser pulses is also included in this chapter.

The main objective of **Chapter 2** is to describe the experimental investigations on fundamental physical phenomena during laser pulse interaction with dielectric or metallic surface using time and space resolved optical emission spectroscopy (OES) and optical time of flight emission spectroscopy (OTOF-ES). Diagnostic applications of plasma spectroscopy in determining electron temperature and plasma density are discussed in this chapter. LPP generation from some metal oxide targets are studied with reference to corresponding metal targets of pure quality as reference. Line emissions from atomic and ionic species are employed for the characterization. The experiments were conducted at diffusion vacuum level. For each of the selected targets, plasma density and temperature are evaluated using spectroscopic characteristics and dynamics of neutral and ionic species. Under the same laser fluence and experimental conditions, LPP from oxide target of Titanium (TiO_2 Pellet) shows a higher ionization degree compared to the corresponding Ti target. In contrast to metallic target, a fast degradation of ion drift velocities near the target and relatively higher values of electron densities are observed in the LPP of Aluminium oxide (Al_2O_3 Pellet) target. During free expansion into vacuum, the differential expansion of the plume elements becomes noticeable at larger distances. For both metallic and oxide targets of Tin (SnO_2 Pellets), time integrated temperature is found to increase with distances farther than 4mm.

The principal factors influencing the nature of interaction between laser radiation and a solid target in vacuum are duration, wavelength and power density of the laser pulse, laser absorption processes, physical and chemical properties of the target and geometry of the target. **Chapter 3** discusses the applications of electrical signal between the target and collector (plasma chamber body or metallic wire mesh) on laser plasma diagnostics. Target materials get electrically charged when they are photo-ablated with high energy laser pulse. This leads to fast-rising voltage transients between the target and the collector, which serves as an alternate probe signal

providing information about the nature of ablated species, their expansion velocities, extent of ionization in the plume and electron and ion currents in real time. Plasma generation and plume evolution processes get reflected on the temporal variations of the recorded TOF spectrum. Expansion dynamics in field free vacuum and the effects of external magnetic field on the dynamics of LPP are probed using source target signal derived from metallic copper targets, results of which are also included in this chapter.

Chapter 4 deals with the emission characteristics and dynamics of laser induced Lithium plasma in magnetic field. Behavior of neutrals and ions with magnetic field strength are studied results of which are also included in this chapter. It is observed that the intensity of recombination radiation is strongly reduced by the field. The magnetic field does not significantly affect the arrival time distribution of the ejected species. With sufficient ambient pressure, presence of the field increases the lifetime of neutral species. During the interaction between expanding plasma and ambient gas, buffer gas is ionized and more free electrons are produced. The enhanced values of electron density increase the excitation probability of species.

Imaging techniques are used on a routine basis in fusion research to provide much information about the plasma emissivity, plume shape, emission positions relative to the laser spot, fluctuations in the spatial distribution of different plasma parameters and so on. **Chapter 5** presents the irradiance dependence of plasma emissivity studied using tomographic projection measurements on expanding LIP from the target. The emissivity contours are reconstructed through an image processing technique called pixel method. Pixel method is suitable if the plasma cross-section is smooth in polar coordinates with a zero level near the origin. A photo detector of nanosecond rise time observes the plasma through a cone of small solid angle. The axis of this cone is designated as chord. The emitting region is divided into pixels of constant emissivity and a definite number of pixels are always seen by the detector. Local emissivity values are calculated from the system of simultaneous linear equations formed when all the detector positions are taken into account. Irradiance

dependence of plasma emissivity and chord brightness are generated and analyzed by a tomographic inversion of the system of integral equations.

Chapter 6 describes the technique of digital holographic interferometry (DHI) as applied to the in situ diagnostics of LPP which serves as the phase object for the digital hologram. DHI enables full digital recording and a completely different way of processing. For each case of the LIP from a Titanium target, a digital hologram is recorded using a continuous laser beam and reconstructed numerically. The hologram acts as an amplitude grating and the analysis is made using well known diffraction theory. Reconstruction of the numerical hologram is realized by a convolution approach available from the Fresnel-Kirchoff diffraction integral. The numerically generated reference beam will get diffracted from the holograms and the wave fields are reconstructed in a plane behind the hologram, thereby forming the objects. From the resulting complex amplitudes, interference phase can be calculated. Interference phase is proportional to the integral of refractive index distribution within the plasma which is directly related to the free electron density.

Chapter 7 deals with the general conclusions drawn from the present studies and outlines some of the directions in future works.

List of publications

I. Journal Publications

1. **V J Dann**, Manoj V Mathew, V P N Nampoori, C P G Vallabhan, V M Nandakumaran, P Radhakrishnan; Spectoscopic Characterization of Laser Induced Plasma from Titanium Dioxide; *Plasma Sci. and Technol. Vol.9, No.4 456 (2007)*

2. **V J Dann**, V M Nandakumaran, V P N Nampoori; Plasma Dynamics of Neutral Species of Titanium in Laser Ablated Titanium Dioxide (*communicated)*.

3. **V J Dann**, Arun Anand, V P N Nampoori; Radial Electron Density Distribution in Laser Induced Plasma Using Digital Interferometry (*communicated*).

4. **V J Dann**, Arun Anand, V P N Nampoori; Diagnostics of Laser Induced Plasma Using Optical Tomography (communicated).

5. Litty Irimpan, **V J Dann**, Bindu Krishnan, A Deepthy, V P N Nampoori and P Radhakrishnan; Backscattering of Laser Light from Colloidal Silica; *Laser Physics, Vol 18, Issue 7, 882 (2008).*

6. Ritty J Nedumpara, K Geetha, **V J Dann**, C P G Vallabhan, V P N Nampoori and P Radhakrishnan; Light Amplification in Dye Doped Polymer Films; *J. Opt. A: Pure Appl. Opt. 9 174 (2007).*

7. Bindu Krishnan, A Deepthy, Litty Irimpan, **Dann V J**, V P N Nampoori; Backscattering from Nano-sized ZnO Suspensions; *Physica E 35 23 (2006).*

II. Conference Publications

8. **V J Dann**, R K Singh, Ajai Kumar, V P N Nampoori; Optical Emission in Laser Induced Breakdown of Li in Transverse Magnetic Field; Proceedings of *NLS 2007, MS University, Vadodara (December 2007)*.

9. **V J Dann**, Arun Anand, C V S Rao, D Sajeev, V P N Nampoori; Optical Tomography of Laser Produced Plasma using Pixel Method; Proceedings of *Progress*

on Tunable lasers for Ultrafast Processes and Applications (PTLUPA 6), Indian Institute of Technology, Madras (December 21-22, 2006).

10. **V J Dann**, C P G Vallabhan, V M Nandakumaran, V P N Nampoori; Electrical Characterization of Laser Produced Plasma from a Metallic Target; Proceedings of *Plasma 2006, Malaviya NIT, Jaipur (December 19-22, 2006)*.

11. **V J Dann**, C P G Vallabhan, V M Nandakumaran, P Radhakrishnan, V P N Nampoori; Effect of External Magnetic Field on the Dynamics of Laser Generated Plasma from a Solid Target; Proceedings of *PHOTONICS 2006, University of Hyderabad (December 13-19, 2006)*.

12. **V J Dann**, Manoj V Mathew, V M Nandakumaran, C P G Vallabhan, V P N Nampoori; Temporal Profile of Ti in Laser Produced Plasma from Titania; Proceedings of *Fifth DAE-BRNS National Laser Symposium (NLS-5), Vellore (December 2005)*.

13. **V J Dann**, Manoj V Mathew, Jaimon Yohannan, C P G Vallabhan, V M Nandakumaran and V P N Nampoori; Spectral Characterization of Laser Produced Plasma from Titanium Dioxide; Proceedings of *20th Natonal Symposium on Plasma Science and Technology (PLASMA 2005), Cochin (December 2005)*.

14. Sajeev D, **Dann V J** and Nampoori V P N; Spectral Studies on the Laser Induced Breakdown of Corals; Proceedings of *PHOTONICS 2006, University of Hyderabad (December 13-19, 2006)*.

15. Sajith Mathews T, **Dann V J**, Nampoori V P N; Laser Induced Breakdown in Aqueous Solutions of Rhodamine 6G; Proceedings of *Fifth DAE-BRNS National Laser Symposium (NLS-5), Vellore (December 2005)*.

16. Litty Irimpan, **V J Dann**, Bindu Krishnan, A Deepthy, V P N Nampoori and P Radhakrishnan; Studies on Back-scattering of Laser light in Colloidal Silica; Proceedings of *Seventh International Conference on Optoelectronics, Fiber Optics and Photonics (PHOTONICS 2004), Cochin (December 9-11, 2004)*.

17. Lyjo K Joseph, Litty Mathew Irimpan, **Dann V J**, Radhakrishnan P and Nampoori V P N; Fluorescence Study of Lanthanum Titanate; Proceedings of *Fifth DAE-BRNS National Laser Symposium (NLS-5), Vellore (December 2005)*.

18. Bindu Krishnan, Litty Irimpan, Deepthy A, **Dann V J**, Nampoori V P N; Non-linear Optical Properties of Nano ZnO Colloids Using Z-Scan Technique; Proceedings of *Fourth DAE-BRNS National Laser Symposium, BARC, Mumbai (January 10-14, 2005)*.

19. Bindu Krishnan, A Deepthy, Litty Irimpan, **Dann V J**, V P N Nampoori; Coherent Backscattering from Nano-sized ZnO; Proceedings of *Seventh International Conference on Optoelectronics, Fiber Optics and Photonics (*PHOTONICS 2004*), Cochin (December 9-11, 2004)*.

20. **Dann V J**, Amrithesh M, Seema R, Thomas Lee S; A Macrobend Fiber-optic Force Sensor; Proceedings of *Second International Conference and Twenty Seventh Annual Convention of the Optical Society of India, Science and Technology Museum, Thiruvananthapuram (August 27-29, 2001)*.

CONTENTS

CHAPTER 1

Introduction

1.1. Laser plasma interactions

The main aim of the work reported in the present thesis is the experimental and theoretical studies of the fundamental physical phenomena related to laser pulse interaction with dielectric or metallic surfaces. High power laser-matter interaction results in the laser ablation and laser induced plasma (LIP) formations. The ablation and plasma properties are directly related to the physical mechanisms of laser pulse energy absorption and its redistribution in the solid and laser plasma. Studies on plasma have applications in diverse areas of science and technology. For example, in an effort to harness fusion energy on earth, physicists study devices that create and confine very hot plasmas in magnetic fields. In space, plasma processes are largely responsible for shielding earth from cosmic radiation, and much of the sun's influence on earth occurs by energy transfer through the ionized layers of the upper atmosphere. Plasma dynamics is the key field of study in understanding stellar structures.

Studies in the field of high intensity laser interaction with matter unfold numerous exotic phenomena so that the subject always stands among the current topics of research. Progress in short pulse laser technology has been in fast pace since the invention of chirped pulse amplification in 1985. At present, pulses shorter than an atto second are available. Today, Peta watt (PW) lasers are already in operation and Exa watt (EW) lasers have been successfully installed in Europe [1]. Ordinary matter will easily get ionized when subjected to high intensity irradiation. The electrons released by ionization processes are then immediately caught in the laser field and oscillate with a characteristic energy dictated by the subsequent laws of interaction. The four parameters governing the laser radiation during the interaction are wavelength, energy, pulse duration and focal spot size.

During the initial evolution of LIP, one can roughly assume a one-dimensional cartesian expansion as long as the expansion distance is much smaller than the focal spot diameter. When the plasma expands in ambient air, the plasma expansion at later times

can be reasonably taken to be hemispherical. Several computational models [2-7] have been proposed to explain the physical phenomena involved in optical breakdown of solid materials. Modelling of optical breakdown are carried out, based on the effects of avalanche ionization, electron – ion recombination, electron diffusion and so on. Niemz [8] found a square root dependence of the energy density on the pulse duration in the pico-second and nano-second range. Nano-second time scale pulses can interact with the expanding plasma so that the electron density, temperature of the excited species and so on, are sustained longer than those due to ultra-short laser pulses.

1.2. Plasma hydrodynamics and numerical modelling

Plasma theory is a combination of electromagnetic theory and theory of hydrodynamics related to plasma. There are various hydrodynamic descriptions of plasma starting with the one fluid model of Alven. General macroscopic equations for fully ionized plasma are the two fluid equations derived by Schluter and Biermann [9]. The different physical models for LIP incorporate the salient plasma features, laser structure, and numerical algorithms that accurately solve the governing equations. The whole processes of target ablation, implosion and ignition are essentially determined by hydrodynamics.

In the case of fluids, there is a velocity field whose temporal derivative corresponds to the acceleration, a mass density field $\rho(x, y, z, t)$ which corresponds to the mass m and a force density which is given by the gradient of the pressure field $p(x, y, z, t)$. Consider the fluid as being composed of electrons of mass m, density n_e, temperature T_e and ions of mass m_i, density n_i and charge Z. Assuming space charge neutrality, $n_i = n_e / Z$, the mass density field is given by,

$$\rho(x, y, z, t) = m_i n_i(x, y, z, t) + m n_e(x, y, z, t) \tag{1.1}$$

and the pressure field is,

$$p(x, y, z, t) = n_e K T_e + n_i K T_i \approx (1 + Z) n_i K T_e \tag{1.2}$$

The first basic equation is Euler equation which corresponds to the conservation of momentum:

$$\rho \frac{\partial \mathrm{v}}{\partial t} + \rho \mathrm{v} \cdot \nabla \mathrm{v} = -\nabla \mathrm{p} \tag{1.3}$$

The second basic equation is the conservation of mass, which is the equation of continuity:

$$\frac{\partial \rho}{\partial t} + \nabla \cdot (\rho \mathrm{v}) = 0 \tag{1.4}$$

In addition to these two, the equation of energy conservation is needed to arrive at the complete set of differential equations for uniquely solving the gas dynamic expansion of LIP. This equation is of the type,

$$\frac{\partial}{\partial t}\frac{\rho}{2}\mathrm{v}^2 = -\frac{\partial}{\partial t} n_i KT(1+Z) - \nabla \cdot (\kappa_T \nabla T) + W \tag{1.5}$$

where, LHS describes the temporal change of the kinetic energy of the fluid to be compensated by the change of internal energy (first term on RHS), by thermal conduction, characterized by the thermal conductivity κ_T and by power density W of radiation. In LIP, the net electrodynamic potentials can change in time. These components will then have to be included as additional potentials [10].

Fluid equations for the conservation of mass, momentum and energy are solved by means of suitable codes. The plasma is treated as a single fluid described mainly by a set of four main variables: density, velocity, electron, and ion temperature, which are functions of spatial coordinates and time. The fluid velocity is obtained by solving the momentum equation, using the appropriate pressure boundary condition at the interface with the ambient air. The plasma temperature can be obtained by solving the electron and ion energy conservation equations in which the source terms include the absorption of the laser energy, the heat conduction, the electron–ion coupling and the radiation loss term. The radiative energy losses, local energy changes due to radiative transfer within the plasma and radiative losses through the boundaries are also to be taken into account [11-14].

For moderate background pressures, the hypothesis of a spherical expansion appears to be reasonable for the description of near-axis plume behavior [15]. However, in high vacuum, the plume is essentially forward directed, and therefore a one-dimensional fluid dynamic model can be used to describe the system [16-22]. This model considers only the stages of expansion during and after the laser pulse without detailing the evaporation process. At the end of the laser pulse, a plume is assumed to be formed in the direction perpendicular to the target, in the same position of the irradiated spot center. The laser energy is spent on melting, vaporization and heating of the target material and

on heating and ionization of the vaporized particles. Before the expansion, the plasma can be considered to be in thermal equilibrium. After pulse termination, the cloud begins to expand perpendicular to the target into the ambient gas at specific pressure. The plasma has been treated as a single fluid characterized by one velocity and one temperature. This fluid dynamic approach disregards the effects of space-charge separation, as the time-averaged electric field of the laser radiation is zero. In fact, numerous studies have shown that the angular distribution of the laser-generated flux is often much more strongly forward peaked than the flux obtainable from small-area effusive sources operating under collision-less conditions. This forward peaking phenomenon for deposition in vacuum is now generally accepted as arising from collisions of the plume species among themselves.

Quite different approaches to simulate the LIP expansion have been proposed by Wood et al. [23, 24]. The Wood's model is based on a combination of multiple scattering and hydrodynamic approaches. The plume is allowed to be broken into different orders of scattering, whose particles can undergo many collisions with the background. Particles can only be transferred from one order to the next higher order by collisions. The densities in the individual orders propagate according to the usual conservation equations to give the overall plume expansion. Nemirovsky et al. [25], starting from the Boltzmann equation, have derived the hydrodynamic equations of motion for partially ionized plasma when the charged component and the neutral component have different flow velocities and temperatures. They have developed a general approach for the hydrodynamics of a gas in a binary mixture, when the interaction between particles of the same species is much stronger than that between particles of different species.

Le et al. [26] demonstrates a persistent lack of equilibrium between the electron and heavy particles in the expanding plasma plume. To take this effect into account, the fluid dynamic method is coupled with a kinetic approach. The processes included in the model are the ionization of the ground state and the three-body recombination as well as the photo-recombination into the ground state.

To overcome the limits of the gas-dynamic approach, many authors have investigated the plume expansion and the effects of collisions amongst particles desorbed from solid surfaces by means of direct Monte Carlo simulation. According to such a simulation by Urbassek et al [27], light and heavy particles are spatially segregated due to

the different velocity of desorbed heavy and light particles. In the back part of the cloud both species appear to be well mixed while the front part of the cloud consists mainly of light species. Itina et al [28] showed that at low pressure (0.01 mTorr), heavy particles are more energetic than light particles and their distribution of mean energy is more focused towards the center. As the background pressure increases, the mean energies of both species diminish and the distributions become less focused toward the center. This effect is more evident for light particles than for heavy particles. The decrease of the kinetic energy of the plume particles is due to the collisions with the background gas, which thermalize the particles. The decline of energy is more pronounced for light species, because they lose energy more efficiently in a collision. Therefore a smaller background pressure is required for thermalization of light components. At high pressures (100 mTorr) most of the particles are thermalized and energy distributions become broadened along the normal of the surface. The difficulties of the gas-dynamic description of the diffusive processes are avoided in such models.

To simulate the real system under study, it is necessary to include chemical models also into the fluid dynamic code. For example, in a TiO plasma in local thermodynamic equilibrium (LTE), the plasma thermodynamics is completely defined by two independent parameters, such as pressure and temperature, or enthalpy and pressure. A strong non-linear coupling occurs between the chemical kinetics and the fluid dynamics [17].

A fluid dynamic model to investigate the effects of finite rate coefficients on the plume expansion for a titanium plasma includes (a) ionization by electron impact (b) three-body recombination and (c) radiative recombination [16, 29, 19]. The simulations reveal the strong influence of plasma chemical processes on the time of flight (TOF) plots. The plasma, initially produced by the laser–matter interaction is supposed to be completely ionized. When kinetic processes of plasma chemical reactions are included, the TOF plots of Ti become significant, due to recombination processes. At the first instant, the plume arriving at 0.5 mm is essentially composed of ions, as the kinetic effect is still negligible. As time increases, recombination takes place, and consequently, the Ti molar fraction grows up, while the ion molar fraction decreases. TOF plot analysis highlights an apparent separation between atom and ion concentrations, when kinetics is introduced in the numerical modelling [29].

1.3. Outcomes of numerical modelling

The results of modelling suggest that plasma properties depend more strongly on the fluence near the ablation threshold. However, for the higher fluences of interest, the temperature and electron density reach a saturation value due to the increase of the plasma radiative cooling with the plasma temperature. Ablation of metals occurs at relatively low intensity compared with that for a transparent dielectric whose absorption is negligibly small resulting in large threshold for optical breakdown. For typical dielectrics like ceramics, energies involved in ablation are close to those required for heating the targets beyond their melting temperatures and initiate significant evaporation. Material ejection is accompanied by the formation of a vapor or plasma just above the target surface and an easily recognizable snapping sound as the velocity of some of the species exceeds the speed of sound in the immediate environment. In order to make the process efficient, so that energy is not lost due to carrier or thermal diffusion during the laser light absorption, short laser pulses should be used at a wavelength strongly absorbed by the material. For power densities above the vaporization threshold, the dominant mechanism is vaporization [30, 31].

There exist two zones in the model described by Aden et al [15], at pressures below 1 mbar: one which is directly attached to the target surface throughout the whole process, and the second is recognized as an outward moving shock front. Heavier background gases, such as *Ar* result in a slower expansion component of the vapour plume and hence lower plume velocity and shorter plume length. The plasma temperature and ionization degree seem not to be affected by the background gas, up to 100 ns. The background gases with lower ionization potential exhibit a higher ionization degree in the plasma. Further, the threshold for plasma formation in the background gas is determined by the ionization potential of the gas. Bogaerts et al [32] predicts that most of the laser–plasma interaction occurs with the background vapour, so that plasma shielding (change in the efficiency of laser energy coupling to the target by increased absorption and/or reflection from the laser-induced plasma) is only a little bit more pronounced in the gases with lower ionization potential, such as Ar, than in He.

A three dimensional Monte Carlo simulation of LIP in vacuum indicates that, when more than a few monolayers are ablated, the laser energy absorption by the evaporated particles has dominant effects on the plume shape during the expansion

process. A fraction of the recombination of ionic and excited species leads to a delayed kinetic energy transfer in the plume. This has a significant effect on the angular and kinetic energy distributions of the evaporated particles [33].

1.4. Plasma emissions induced by nanosecond and femtosecond laser pulses

In typical nanosecond laser ablation processes, two types of photon absorption mechanisms dominate. The first one is inverse bremsstrahlung absorption, which involves photon absorption by free electrons. Free electrons can gain energy from the laser beam through collisions with neutrals and ions. The probability of photon absorption due to electron-neutral collisions is much smaller than that due to electron-ion collisions. The second mechanism is photo-ionization of ground- and/or excited-state species, and multi-photon ionization for sufficiently high laser intensity. A bound electron is excited to the free energy level and thus ionized by absorbing one or more photons. The effect of the inverse bremsstrahlung process becomes more important for longer wavelengths, whereas the opposite is usually true for photo-ionization and multi-photon ionization processes [34].

Femtosecond laser beams can induce properties, which might allow improvements in analytical treatment of current nanosecond-laser-induced breakdown spectroscopy. Femtosecond laser interactions with matter have the potential for innovative materials applications. Clean craters were observed by interferometric microscope measurements [35] indicating the advantages and potential for applying femtosecond lasers to micromachining and advanced materials treatment. Due to a much smaller thermal diffusion depth, high-precision ablation and minimal damage can be obtained with femtosecond lasers. Femtosecond regime is better than the picosecond and the nanosecond ones for precise material processing because of full vaporization of the matter and no trace of molten material [36]. This regime occurs at the laser pulse duration less than 200 fs. For femtosecond laser-material interactions, only a very small fraction of the laser pulse energy is transmitted as heat and transferred to the material surrounding the laser-irradiated area. Consequently, femtosecond laser pulses can induce non-thermal structural changes, driven directly by electronic excitation and associated nonlinear processes, before the material lattice has equilibrated with the excited carriers. This fast

mode of material modification can result in vanishing thermal stress and minimal collateral damage for processing practically any solid-state material.

An intermediate regime takes place at the laser pulse duration between 0.5 ps and 100 ps. The most appropriate description of the heating and expansion processes in this regime is given by the conventional two-temperature approach [37-40].

At the longer laser pulse duration (~ ns), the heat conduction and hydrodynamic motion dominate the ablation process. The electrons and lattice ions are in equilibrium early in the beginning of the laser pulse. Hence, the limiting case of thermal ablation is suitable for the description of the long pulse ablation mode. The total melt and evaporation depth increase slightly for longer laser pulses, because the target is exposed to the laser for a longer time, and it is found that the plasma shielding is a bit less pronounced for longer pulses, because of the lower irradiance, so that the net laser fluence reaching the target increases slightly with pulse duration [41].

For energies higher than 3 mJ, there is little difference between 50 ps and 10 ns pulses in the plasma emission both in terms of the intensity of the emission lines and in terms of lifetime of the emission. Differences become significant only at very low fluences approaching the plasma formation threshold, which is significantly lower for 50 ps pulses than for 10 ns pulses. Calculations using a plasma ablation model show that initial plasma conditions are significantly different for 50 ps and 10 ns pulses during irradiation by the laser pulses. However, the dominant process leading to plasma emission at later times is from expansion and cooling of the plasma plume in the form of a blast wave in the ambient air which is primarily dependent on the energy deposited in the plasma and not on the pulse length [42].

1.5. Ablation mechanisms

The density of free electrons can grow exponentially by electron impact ionization, which involves collision of bound electrons with free electrons. If the free electron is accelerated such that its kinetic energy exceeds the ionization potential of the bound electron, ionization of the bound electron could occur, resulting into two free electrons. This process can repeat itself and lead to an avalanche event. Plasma with a critical density is formed when enough bound electrons are generated through ionization of atoms. The plasma forms within the laser pulse, and starts to absorb incident laser

light. Consequently, the laser light coupling mechanism into the target is significantly altered. For ultra-short laser pulses, the electrons are first driven to very high peak temperatures, while initially the lattice temperatures remain low. When the critical density level is reached, the plasma oscillation frequency is equal to the laser frequency and plasma with significant absorption character is formed. The electron-phonon scattering time scale is of the order of 100fs in most metals and semiconductors, while the phonon–phonon scattering time is on the order of 10ps. Consequently, for pico and femtosecond laser based heating of solids, initially the electrons are not in equilibrium with the lattice and subsequently electron-lattice heating raises lattice temperature. Recombination during the laser pulse is negligible because it requires longer time relative to the pulse duration. The energy density initially deposited within the lattice is responsible for the material surface damage through plasma expansion and material evaporation. The actual material damage and ablation usually occurs a few ps after the expiration of the laser pulse [35]. Prevalence of multiphoton excitation and absence of interaction of the laser pulse with ablated material appear to be the main characteristics of the femtosecond regime [43].

During its temporal evolution, the recombination character dominates the plasma expansion, and hence LTE hypothesis cannot be completely assumed. Energy transfer duration from the electrons to ions by coulomb collisions is longer than the laser pulse duration. Therefore, the conventional hydrodynamic motion does not occur during the femtosecond interaction time. There are two forces which are responsible for momentum transfer from the laser field and the energetic electrons to the ions in the absorption zone: one is due to the electric field of charge separation and another is the ponderomotive force. The charge separation occurs if the energy absorbed by the electrons exceeds the fermi energy (which is approximately a sum of the binding energy and work function) and escapes from the target. The electric field of charge separation pulls the ions out of the target. At the same time, the ponderomotive force of the laser field in the skin layer pushes electrons deeper into the target. Correspondingly it creates a mechanism for ion acceleration into the target.

The main contribution to femtosecond laser interaction with metals are from the processes of material expansion due to fast heating and very fast energy absorption leading to mechanical stress [44-46]. The superheating and material ablation of metals

caused by ultrashort-pulse lasers are simulated by a model based on the concept of phase explosion [47], which is a rapid boiling process due to the homogeneous nucleation in a superheated volume of liquid near its critical state. For PLD applications, the film composition is precisely same as that of the target because of the explosion like removal of the material at the high power densities [48, 49]. For dielectrics, the dominant channel for free electron generation is either impact or multiphoton ionization depending on the size of the band gap [50]. The ablation threshold for dielectric in the ultra short laser-matter interaction regime must be higher than that for the metals, assuming that all the atoms in the interaction zone are at least singly ionized.

Interaction mechanisms induced by ultrashort pulses, can be treated by different approaches depending on the material, such as the two temperature model [51], coulomb explosion [52-54] and non-thermal heating [55]. Laser–target interaction models using a hydrodynamic code include the absorption of laser radiation, the electronic heat conduction, the electron-phonon or electron–ion energy exchange, as well as a realistic equation of state.

1.6. Features of femtosecond laser-matter interaction

By comparing the femtosecond and nanosecond measurements, it appears that reduced amount of ions are measured in the femtosecond-laser-induced plasma. This is consistent with the fact that femtosecond laser pulses are too short in time to be able to interact with the plasma they have created. In the femtosecond interaction regime of expanding plasma, there are different population species with specific velocities. The electron number density and temperature of fs-laser induced plasma decreases faster than ns-laser induced plasmas due to different energy deposition mechanisms [56]. Because of its short pulse duration, the fs laser beam does not interact with the laser-induced plasma [57, 58]. Femtosecond pulses are of particular interest for ablation as the pulse duration is less than the typical thermalization characteristic time of a few picoseconds [59]. At constant laser irradiance, the target heating, melting and vaporization increase with laser pulse duration, and this applies also to the densities of vapor and background gas atoms and ions, and electrons in the plume, as well as to the plume expansion velocity and temperature, because the laser fluence rises with pulse duration. On the other hand, at fixed laser fluence, the target heating and evaporation rate increase for shorter laser

pulses, because of the rise in laser irradiance. The results show that the ablation thresholds are low in the femtosecond regime and plasma plume is strongly forward directed. The kinetic energy of the species evolved during laser ablation is close to 1 keV in the femtosecond regime and a few hundreds of eV in the case of nanosecond pulses [58, 60].

Femtosecond laser-induced plumes are found to be much smaller and weaker in intensity than those induced by nanosecond laser pulses [35]. The plume temperature and electron density during or shortly after the laser pulse become higher for shorter pulses at fixed laser fluence, because of higher laser irradiance. However, at a certain moment in time, sufficiently long after the laser pulse, it is observed that the total laser fluence, and not the pulse duration, determines the plume behavior, because the plume and plasma characteristics look very similar for different pulse durations, at constant laser fluence [41]. The temporal dynamics of the continuum and the spectral lines depend much more on the laser fluence than on the pulse duration. The decay time of the continuum emission due to the bremsstrahlung, is about three times higher with a nanosecond pulse than with a femtosecond one. With respect to ns-LIBS, the fs-laser induced spectra are characterized by smaller spectral continuum contribution, shorter duration and better resolution of the spectral lines [61, 62]. LIP illuminated by ultra-short, ultra-intense optical pulses is a rich non-linear medium for the study of parametric production of electromagnetic radiation and collective phenomena such as x-ray generation, terahertz radiation, amplification and guiding of optical pulses.

In subsequent chapters, details of the work carried out on LIP from some solid targets using ns laser pulses and simulation of plasma characteristics are described.

1.7. References

[1] K. Imasaki and D. Li, Journal of Physics: Conference Series 112 042071 (2008)

[2] F. Seitz, Phys. Rev. 76 1376 (1949)

[3] A. G. Molchanov, Sov. Phys. Solid State 12 749 (1970)

[4] N. Yablonovitch and N. Bloembergen, Phys. Rev. Lett. 29 907 (1972)

[5] N. Bloembergen, IEEE J. Quantum Electron. QE-10 375 (1974)

[6] A. S. Epifanov, IEEE J. Quantum Electron. QE-17 2018 (1981)

[7] C. A. Sacchi, J. Opt. Soc. Am. B 8 337 (1991)

[8] M. H. Niemz, Appl. Phys. Lett. 66 (10) 1181 (1995)

[9] A. Schluter and L. Biermann, Z. Naturforsch., 5A (1950), 237

[10] Heinrich Hora, Physics of laser driven plasmas, (Wiley Interscience, New York), (1981)

[11] S. Laville, F. Vidal, T. W. Johnston, M. Chaker, B. Le Drogoff, O. Barthelemy and J. Margot, Phys. Plasmas Vol.11 No.5 2182 (2004)

[12] I.B. Gornushkin, A.Ya. Kazakov, N. Omenetto, B.W. Smith, J.D. Winefordnerb, Spectrochimica Acta Part B 60 215 (2005)

[13] Zhaoyan Zhang , Zhen-Xue Han and George S. Dulikravich, J. Appl. Phys. Vol. 90 No.12 15 (2001)

[14] C. Garrido, B. Leon and M. Perez-Amor, J. Appl. Phys. Vol. 69 No.3 1133 (1991)

[15] M. Aden, E.W. Kreutz, A. Voss, J. Phys. D: Appl. Phys. 26 (10) 1545 (1993)

[16] Anna Rita Casavola, Gianpiero Colonna, Alessandro De Giacomo, Olga De Pascale, and Mario Capitelli, Appl. Opt. 42 (30) 5963 (2003)

[17] G. Colonna, A. Casavola, M. Capitelli, Spectrochim. Acta Part B 56 (6) 567 (2001)

[18] A. Casavola, G. Colonna, A. De Giacomo, M. Capitelli, J. Thermophys. Heat Transfer 17 (2) 225 (2003)

[19] A. Casavola, G. Colonna, M. Capitelli , Appl. Surf. Sci. 208–209 85 (2003)

[20] R.K. Singh, J. Narayan, Mater. Sci. Eng. B 3 (3) 217 (1989)

[21] R.K. Singh, O.W. Holland, J. Narayan, J. Appl. Phys. 68 (1) 233 (1990)

[22] A.V. Bulgakov, N.M. Bulgakova, J. Phys. D: Appl. Phys. 28 1710 (1995)

[23] R. F. Wood, J. N. Leboeuf, D. B. Geohegan, A. A. Puretzky and K. R. Chen, Phys. Rev. B 58 (3) 1533 (1998)

[24] K. R. Chen, T. C. King, J. H. Hes, J. N. Leboeuf, D. B. Geohegan, R. F. Wood, A. A. Puretzky, and J. M. Donato, Phys. Rev. B 60 (11) 8373 (1999)

[25] R.A. Nemirovsky, D.R. Fredkin, A. Ron, Phys. Rev. E 66 (6) 066405 (2002)

[26] H. C. Le, D. E. Zeitoun, J. D. Parisse, M. Sentis, and W. Marine, Phys. Rev. E 62 (3) 4152 (2000)

[27] H.M. Urbassek, D. Sibold, Phys. Rev. Lett. 70 (12) 1886 (1993)

[28] T.E. Itina, W. Marine, M. Autric, J. Appl. Phys. 82 (7) 3536 (1997)

[29] A. Casavola, G. Colonna, A. De Giacomo et al, J. Thermophys. Heat Transfer 17 (2) 225 (2003)

[30] E.W. Kreutz, Applied Surface Science 127–129 606 (1998)

[31] G. Abdellatifa, H. Imam, Spectrochimica Acta Part B 57 1155 (2002)

[32] Annemie Bogaerts, Zhaoyang Chen and Davide Bleiner, J. Anal. At. Spectrom., 21, 384 (2006)

[33] F. Garrelie, J. Aubreton and A. Catherinot, J. Appl. Phys., Vol. 83, No.10 5075 (1998)

[34] S. Amoruso, M. Armenante, V. Berardi, R. Bruzzese and N. Spinelli, Appl. Phys. A: Mater. Sci. Process. 65 265 (1997)

[35] Mengqi Ye and Costas P. Grigoropoulos, J. Appl. Phys., Vol. 89, No.9 (2001)

[36] B.N. Chichkov, C. Momma, S. Nolte, F. Von Alvensleben, A. Tunnermann, Appl. Phys. A 63 109 (1996)

[37] Yu. V. Afanasiev and O. N. Krokhin, Proceedings of the International School of Physics ‘‘Enrico Fermi’’ Course XLVIII, edited by P. Calderola and H. Knoepfel (Academic, New York, 1971)

[38] S.S. Mao, X. Mao, R. Grief, R.E. Russo, Appl. Phys. Lett. 76 31 (2000)

[39] S.S. Mao, X. Mao, R. Grief, R.E. Russo, Appl. Phys. Lett. 77 2464 (2000)

[40] R.E. Russo, X. Mao, S.S. Mao, Anal.Chem. 74 70A (2002)

[41] Annemie Bogaerts, Zhaoyang Chen, Spectrochimica Acta Part B 60 1280 (2005)

[42] G.W. Rieger, M. Taschuk, Y.Y. Tsui, R. Fedosejevs, Spectrochimica Acta Part B 58 497 (2003)

[43] D. von der Linde, K. Sokolowski-Tinten, J. Bialkowski, Appl. Surf. Sci. 109/110 1 (1997)

[44] D. Perez, L.J. Lewis, Phys. Rev. Lett. 89 255504 (2002)

[45] L.V. Zhigilei, B. Garrison, J. Appl. Phys. 88 1281 (2000)

[46] E. Gamaly, A. Rode, B. Luther-Davies, V. Tikhonchuk, Phys. Plasm. 9 949 (2002)

[47] J.K. Chen1 and J E Beraun, J. Opt. A: Pure Appl. Opt. 5 168 (2003)

[48] L. Bakowsky, G. Herziger, W. Peschko, DVS Ber. (63) 171 (1980)

[49] Jong H. Yoo, Oleg V. Borisov, Xianglei Mao and Richard E. Russo, Analytical Chemistry Vol. 73 No.10 2288 (2001)

[50] M. Lenzner,J. Krüger,S. Sartania,Z. Cheng, Ch. Spielmann, G. Mourou, W. Kautek, and F. Krausz, Phys Rev Lett 80 No 18 4076 (1998)

[51] L.D. Pietanza, G. Colonna, S. Longo, M. Capitelli, Thin Solid Films 453-454 506 (2004)

[52] R. Stoian, D. Ashkenasi, A. Rosenfeld, E.E.B. Campbell, Phys. Rev. B 62 13167 (2000)

[53] R. Stoian, D. Ashkenasi, A. Rosenfeld, M. Witmann, R. Kelly, E.E.B. Campbell, Nucl. Instrum. Methods. Phys. Res. B 166-167 682 (2000)

[54] N.M. Bulgakova, R. Stoian, A. Rosenfeld, I.V. Hertel, E.E.B.Campbell, Phys. Rev. B 69 054102 (2004)

[55] B. Rethfeld, K. Sokolwski-Tinten, D. von der Linde, S.I. Anisimov, Appl. Phys. A 79 767 (2004)

[56] X. Zeng, X.L. Mao, R. Grief, R.E. Russo, Appl. Phys. A 80 237 (2005)

[57] K.L. Eland, D.N. Stratis, D.M. Gold, S.R. Goode, S.M. Angel, Appl. Spectrosc. 55 286 (2001),

[58] V. Margetic, A. Pakulev, A. Stockhaus, M. Bolshov, K. Niemax, R. Hergenroder, Spectrochim. Acta B 55 1771 (2000)

[59] M. Lenzner, F. Krausz, J. Kruger, W. Kautek, Appl. Surf. Sci. 154–155 11 (2000)

[60] Chris B Schaffer, Andre Brodeur and Eric Mazur, Meas. Sci. Technol. 12 1784 (2001)

[61] A. De Giacomo, M. Dell'Aglio , A. Santagata, R. Teghil, Spectrochimica Acta Part B 60 935 (2005)

[62] J.B. Sirven, B. Bousquet, L. Canioni, L. Sarger, Spectrochimica Acta Part B 59 1033 (2004)

CHAPTER 2

Laser induced plasma emissions from some planar solid targets

2.1. Introduction

The study of plasma produced by the interaction of a laser with solid matter is an important aspect of many technological applications, such as material processing, pulsed laser deposition (PLD) and chemical trace analysis. In the past decade, considerable effort has been devoted to the solution of basic questions concerning the dynamics of laser induced plasma (LIP) to improve the in situ models of interaction between laser radiation and material and to control technological processes [1,2].

Due to the interaction of high power laser with matter, the vaporization of surface layers leads to the formation of an expanding plasma. During nanosecond laser ablation, high density plasma is heated to high temperatures and is ionized by inverse bremsstrahlung and the photo-ionization processes. The plasma then expands rapidly in the direction perpendicular to the target surface. During the expansion, the main mechanism of transition of bound electrons is driven by inelastic collisions of electrons with heavy particles, while the concentration of charged particles is controlled by the electron impact ionization and the three-body recombination of electrons with ions.

LIP created by a pulsed laser has been investigated with the aim to study possible dynamical mechanisms in different regimes of time and space. The influence of laser energy on the ejection and propagation of different species in the LIP is also being investigated.

2.2. Experimental setup

An Nd: YAG laser (Spectra Physics, Quanta-Ray DCR-11) with an emission wavelength of 1064nm is used as the source of monochromatic radiation for plasma formation inside an evacuated steel chamber. The chamber is pumped down to $2x10^{-5}$

mbar by rotary and diffusion pumps. The laser is operated at a repetition rate of 10Hz, with pulse duration of 10ns. A high resolution monochromator (1m SPEX) coupled with a thermoelectrically cooled PMT and a time resolved detector (gated integrator and boxcar averager, SR 250) interfaced using appropriate software is used to study the time evolution of plasma. The boxcar gate width and monochromator slit width are optimized to maximize the spectral line intensity while maintaining good temporal resolution. For time resolved measurements, each spectrum is recorded at a gate width of 25ns, which is sufficiently short to follow plasma expansion. An aggregate of 10 signal accumulations is collected for averaging.

An optical system consisting of two lenses of equal focal length (f = 150mm) is used to produce a one to one image slice of the plume in a direction perpendicular to its symmetry axis. The targets are placed inside the chamber, on an axle fixed to a motorized rotating system to provide a fresh surface for ablation. An f/4.5 quartz lens (f = 500mm) is used to irradiate the targets with a laser spot of diameter 0.5mm. The detection systems are always triggered using pulses from the pump laser. A digitizing fast oscilloscope (LeCroy 6050A 500MHz) is used to calibrate and control the gate width and time delay after the laser irradiation. A CCD detector (Roper Scientific, NTE/CCD - 1340/100 - EM) coupled to the exit port of a spectrograph (Acton Research, SpectraPro 500i) is used to record the spectral details collected for the time integrated measurements. Studies are made on LIP from pellets of TiO_2, Al_2O_3 and SnO_2, at various energy levels of the pump laser. The powder forms (commercial grade; 99.9 % purity) of the respective oxides are pelletized using a binder, under high pressure and sintered at high temperatures. The pellets used for the experiment are sintered at the best sintering temperature so that the density of the pellet is not different from that of the original material. For comparison purposes, the spectra from the metallic discs of Ti, Al and Sn were recorded with exactly the same geometry and the same laser focusing. For simplicity, the ambient is diffusion vacuum and gas dynamic effects can be safely neglected. Differences appearing in the plasma expansion would be therefore related mainly to the physical phenomena during the laser-matter interaction. Fig 2.1 gives the schematic diagram of experimental arrangements.

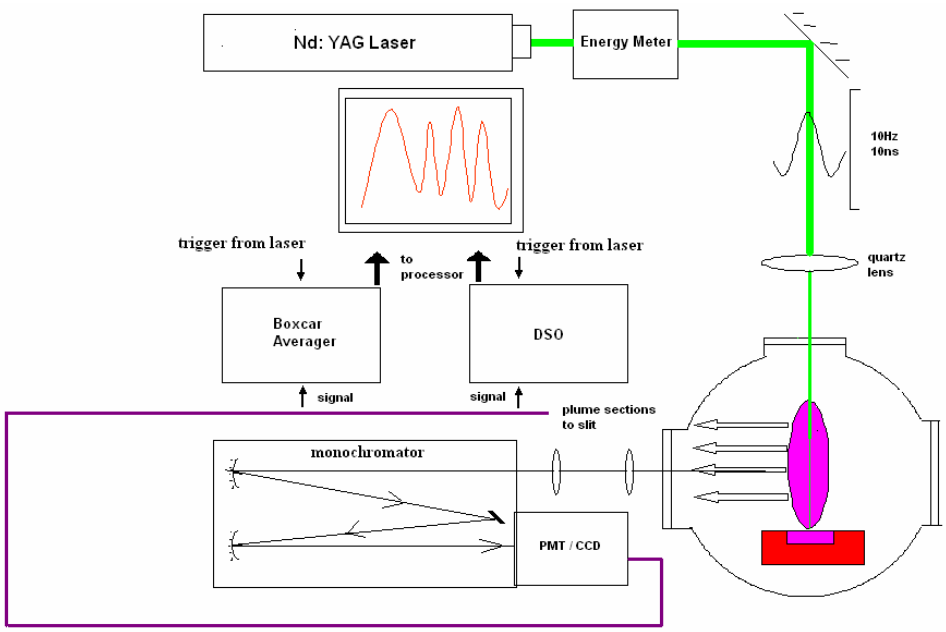

Fig.2.1: Schematic diagram of the experimental setup for optical emission spectroscopy of LIP

2.3.Titanium dioxide and titanium

2.3.1. Plasma emissions and emission profiles

Titanium dioxide is a technologically important material which acts as a photo-sensitizer for photovoltaic cells and as an oxygen sensor. Pulsed laser deposition (PLD) is successfully employed for thin film deposition of materials like TiO_2 and for elemental analysis [3]. TiO_2 films obtained with PLD have numerous optical and thermal applications. Optimization and control of the process demands a better understanding of plasma dynamics. Analysis of optical emissions from plasma is an important diagnostic tool to understand the dynamics of LIP. Moreover, plasma deposited TiO_2 films attract attention due to its high ionic character and comparatively large value of refractive index [4]. For both PLD applications and elemental analysis, it is important to understand the composition and the temporal as well as the spatial evolution of the species in the plasma.

Various experimental techniques can be employed for this purpose. Among them, the most widely used are optical emission spectroscopy (OES), laser induced fluorescence (LIF) and mass spectrometry. Detection of charged particles and laser excitation technique give the best results in the investigation of LIPs far from the target but OES is the simplest way to make the time of flight (TOF) measurements in the high brightness zone of LIP. TOF measurements allow the dynamic aspects of LIP to be studied and give important information on the temporal evolution of species in the plasma plume.

Measurements performed with the experimental setup in Fig. 2.1 yield values that are space-averaged over the whole volume of the considered plasma slice. The laser beam axis is identified as the z-axis and the spectrometer optical axis as the y-axis. In this configuration, the spectrometer entrance slit collects the light emitted by a slice of plasma of thickness Δz along the (x,y) plane. One-dimensional resolution of the ablation plume is achieved by imaging various plasma slices onto the entrance slit of the spectrometer. The experiments carried out at each sampling distance are concerned with the expansion dynamics of the atomic species.

Space resolved OES gives a triple peak distribution exhibited by the TOF profile of Ti I in TiO_2 plasma, above a threshold energy of the pump laser. The evolution of the peaks is studied for various laser irradiances. Their dependence on the distance from the target surface provides some information about their origin. The different peaks are arising from Ti produced by different processes. Particle velocity measurements show a strong collisional expansion.

Optical emissions from excited neutral Ti at 586.6nm [$3d^2.4s^2$ - $3d^2.4s4p$] has been analyzed for time of flight studies. The spectrum exhibits a multiple peak distribution with pump energy increasing beyond 110mJ. At 110mJ of pump energy, a double peak structure (pk1 and pk2 in fig 2.2) is observed. The pk1 is more intense than pk2 till the observation point at 6mm from the target surface. Beyond this, pk2 becomes more intense than pk1 as observed in the figure. A high brightness zone is observed within a distance of 3mm and the intensity is slowly diminished outside the bright zone. This is due to cooling of plasma by recombination processes. In the double peak formation, the delayed peak exists only outside the bright zone. However, at greater energy, the splitting

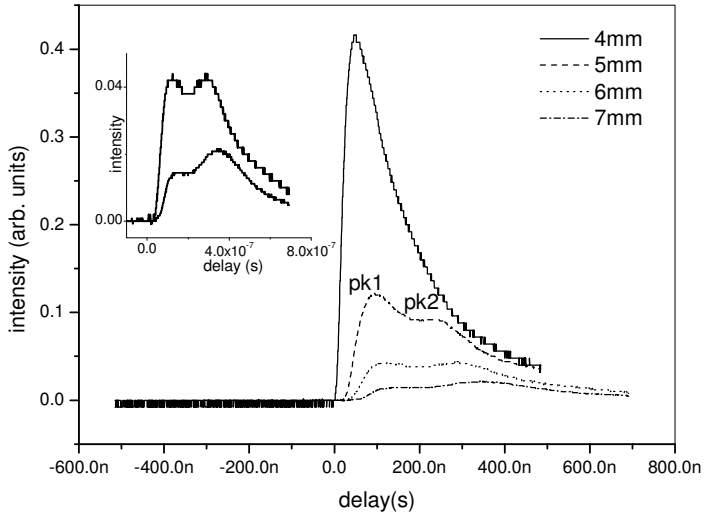

Fig. 2.2: Dual peak distribution of TiI in TiO_2 plasma. Inset shows the plot for 6mm and 7mm. Pump energy is 110mJ.

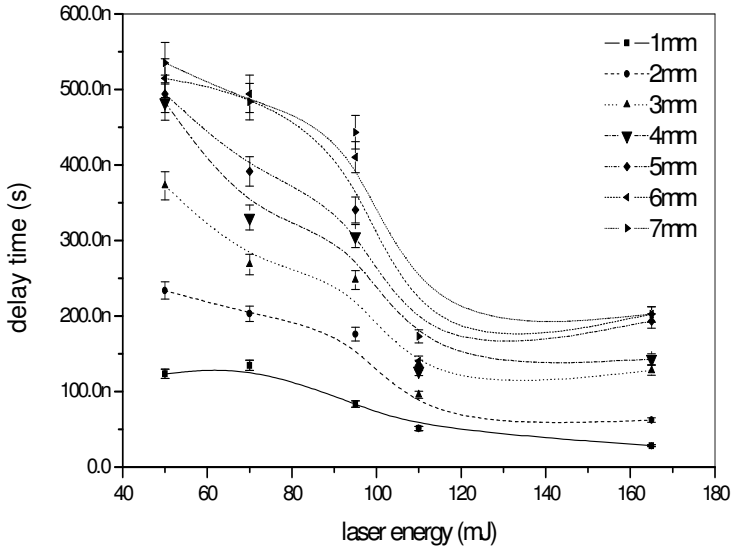

Fig. 2.3: Variation of delay (pk 1) with laser energy at different spatial points from origin of plasma formation. Source - LIP from TiO_2.

is prominent even within the bright zone and a third component (pk3) is observable outside the bright zone. A typical distribution of dual peaks is given in Fig 2.2.

Beyond pump energy around 110mJ, sudden decrease in the delay of pk1 with respect to pump pulse is observed as shown in Fig 2.3. Fig 2.4 depicts the fact that high velocity peak (pk1) initially shows an increase in delay with distance and just beyond the high intensity zone (<3mm), it becomes constant for intermediate distance and then increases with further distances. Delay of pk2 exhibits nonlinear variation with distance, while pk3 shows stronger dependence on delay, with target separation.

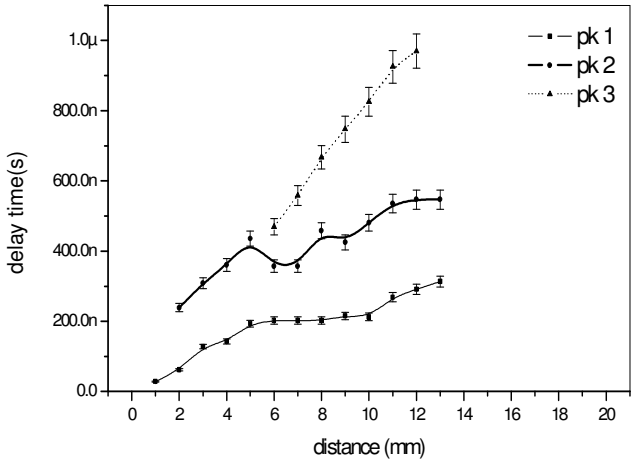

Fig. 2.4: Delay variation of different peaks with distance at laser energy of 165mJ. Source - LIP from TiO_2.

The initial peak structure in the TOF profile of Ti species are assigned to those generated away from the target that is responsible for the higher kinetic energy peak and the most delayed peak to those generated through direct laser ablation or in the vicinity of the target. At intermediate distances, electron impact collision is highly probable and higher excited states are produced. As time evolves, plasma temperature drops so that the excited states undergo collisional recombination with electrons and yields an enhanced spectral emission from Ti [5,6,7]. Such a behaviour is also supported by the fact that emissions of Ti I and Ti II are detected outside the high brightness zone.

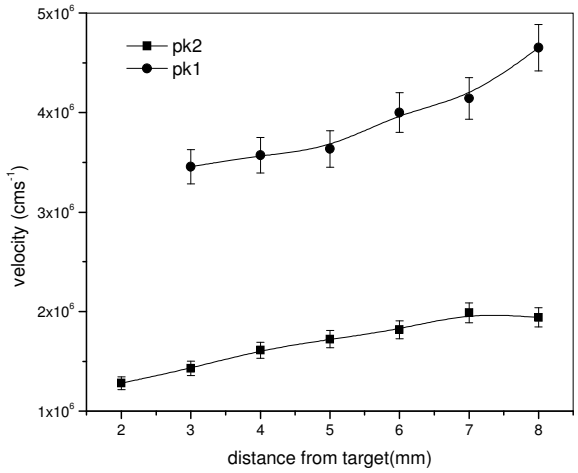

Fig. 2.5: Comparison of pk1 and pk2 velocities in metallic titanium LIP at 250mJ laser energy.

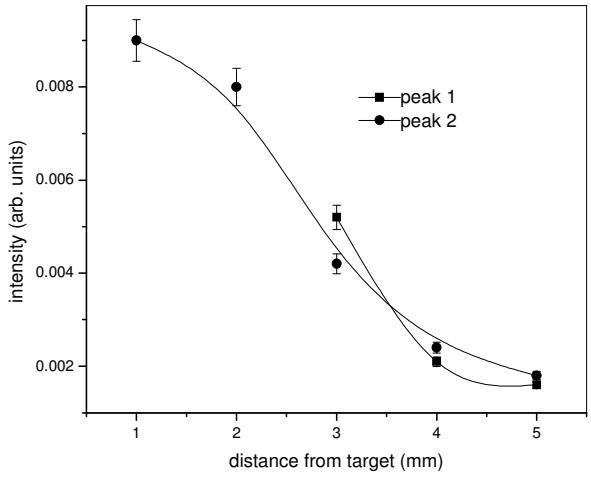

Fig. 2.6: Intensity variation of dual peaks at 100mJ Source – LIP from metallic titanium.

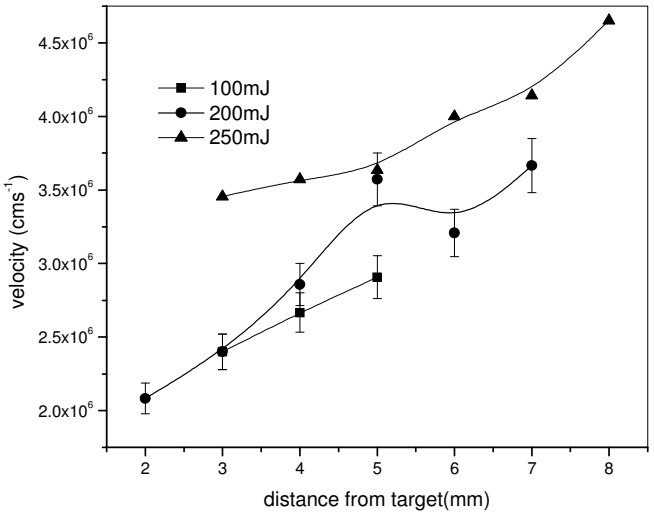

Fig. 2.7:Velocity plot at different laser energies evaluated from pk1. Source – LIP from metallic titanium

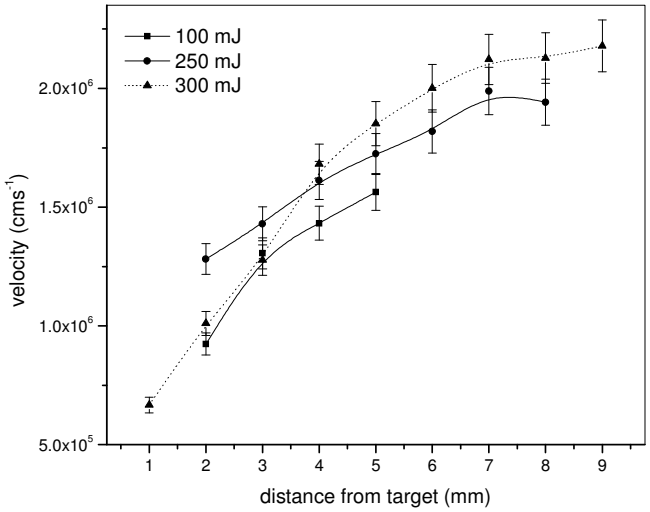

Fig. 2.8: Velocity saturation of pk2 in metallic titanium LIP

The time evolution of LIP species can be used to determine the expansion rate as the distance increases from the target. From the shift of TOF peaks for each distance, the mean velocity of LIP along the propagation axis is obtained. Propagation velocities of different peaks in the optical emission at 6mm from the target are 3 x 10^6 cms^{-1} (pk 1), 1.7 x 10^6 cms^{-1} (pk 2) and 1.3 x 10^6 cms^{-1} (pk3). Velocity of pk1 increases initially and reaches a maximum. This trend is due to initial acceleration of the ablated particles. For

the most delayed peak (pk3), the velocity first decreases and then remains constant. This is attributed to the fact that part of the energy is expended in intra-plume collisions [8].

The TOF spectrum of the same plasma emission (excited neutral Ti at 586.646nm) has been analyzed with pure metallic titanium as the target for plasma production. The presence of twin peaks is clearly evident.

Neutrals present in the LIP of pure metallic targets of Ti also shows Peak 2 from 2mm but peak 1 has been detected only from 3mm onwards. Peak 1 is a high velocity peak (Fig: 2.5) emitted by neutral species produced by recombination of charged ions. At the same time, peak 2 is a delayed one and is produced at the target during the laser pulse. The plasma cools off while expanding in vacuum and the electron temperature at 3 mm has been calculated as approximately 1.2eV by spectroscopic methods. It is also noticed that the peak intensities are falling with increase in distance and decrease in irradiance. Within the spatial region beyond 3mm, peak 2 is more intense than peak 1 as shown in Fig: 2.6. Velocity of peak 1 goes on increasing with distance for different irradiances while for peak 2, velocity attains a steady value at large spatial separations and higher irradiances as is evident from Figs: 2.7 and 2.8.

2.3.2.Time and space evolution of electron density

The interaction of laser beam with solid matter and the consequent plasma generation has been studied for many years. Despite the efforts to exploit the laser - matter interaction for material processing and diagnostic purposes by many workers, some of the aspects still need to be elucidated and clarified. The classical approach in the study of LIP is based on the assumption of local thermodynamic equilibrium (LTE) and optically thin plasma. Using these assumptions, parameters like mass of plasma species, density, temperature and chemical composition of the plasma can be easily determined. In LTE condition, Maxwell - Boltzmann and Saha relations are locally valid. In LIP, where the fast dynamics play a fundamental role, the plasma parameters can change due to the supersonic expansion in shorter time with respect to that necessary for the balancing of elementary processes. The knowledge of deviations from LTE is important to understand the corrections and constraints on the theory to be taken into account for practical applications [9,10]. This point will be discussed further in sections dealing with data analysis.

Optical emission spectroscopy (OES), is based on the intrinsic light emission of LIP and does not need any intrusive systems. The spectral composition at different distances from the target throws light into some of the fundamental properties of LIP, which will help in understanding the main processes that must be taken into account for the analysis of plasma [11]. This represent the behavior of the plasma, along the line normal to the target surface and going through the ablation point on the target.

During the evolution of laser induced plasma, excitation and ionization of the evaporated material occur so that the depositing material is energetically suitable for the film formation. It is then important to determine the thermodynamic parameters of LIP such as electron number density (n_e) and electron temperature (T_e). For this purpose, the emission spectra of LIP have been observed at different distances from the target and varying delay times (t) with respect to the laser pulse. Our interest is mainly concentrated on the initial high density plasma evolution ($t \leq 500$ns). We have chosen spectral lines of Ti I and Ti II for plasma diagnostics. The detection of Stark broadening and displacement of spectral lines allow estimating n_e without considering LTE. The full width at half maximum (FWHM) of a Stark broadened line (in nm), without any ionic contribution is given by the simple relation,

$$\Delta\lambda_{1/2} = 2w\left(\frac{n_e}{10^{16}}\right)\text{nm} \tag{2.1}$$

where, w is the electron impact parameter [12,13].

Stark broadening of the line emission from Ti II transition ($3d^2.4s$-$3d^2.4p$) at 350.5 nm is used to evaluate n_e as a function of space and time. At early times of decay, a highly broadened and shifted line profile is observed, while the width decreases with increasing time and this can be observed from figure 2.9. The value of n_e exhibits rapidly decreasing behaviour (from 1.6 x 10^{16}cm^{-3} at 1mm to 1.2 x 10^{16}cm^{-3}) for distances up to 9mm from the target surface as shown in figure 2.10. Its variation with distance perpendicular to the target (z) approximately follows an inverse dependence on z, which indicates that the initial expansion of the plume is one dimensional and is in agreement with the plume expansion model given by Singh et al [14]. The given n_e distribution fits well to an inverse z dependence of the type $n_e = c + b / (z + a)$ where, $a \cong 5$, $b \cong 4$ and $c \cong 1$. A series of emissions from Ti I are also analyzed for spectral broadening due to Stark effect. Both the emissions from Ti I and Ti II show the same spatial variation. The Stark broadening parameter (w) for Ti I (586.5 nm) is not reported. From the value of n_e obtained through the studies on Ti II line, we can

evaluate w in respect of Ti I line. The parameter w thus obtained has the same order of magnitude reported in similar cases [12].

For the time resolved measurement, a time window of 30 ns is selected to get an optimum resolution. The temporal variations of electron density near the target, at distances of 0.5mm and 1mm from the target are discussed. The observed decay of electron density close to the target and at a spatial separation of 1mm is plotted in Fig.2.11. The temporal variation of n_e in the case of 1mm distance has a fast rise up to a maximum value 5.45 x 10^{16}, which decays to lower values at larger gate delays. The rising part is so fast that it cannot be recorded because of the constraints in the present experimental setup. Here, we observe the high density plasma front, indicated by the intense continuum emission, followed by lower density plasma at later time. For delays greater than 50ns, there is very little change in n_e values. Similar is the case for 0.5mm also. The observation is probably due to recombination processes. The relatively low value at 1mm with respect to that of 0.5mm can be attributed to the plasma propagation [15, 16]. The spatio - temporal evolution of density at an increased energy (200mJ), is as given in Fig.2.12. At the increased laser energy, the density is higher at 1mm and is highly nonlinear function of time delay. A weak dependence of density on time is seen around 3mm. At 4mm distance, there is some kind of modulating dependence of n_e with time delay.

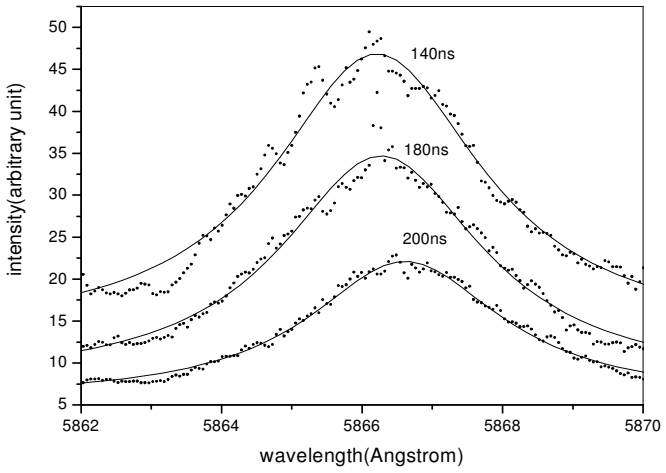

Fig. 2.9: Temporal profile of Ti I (586.5nm) in TiO_2 plasma.

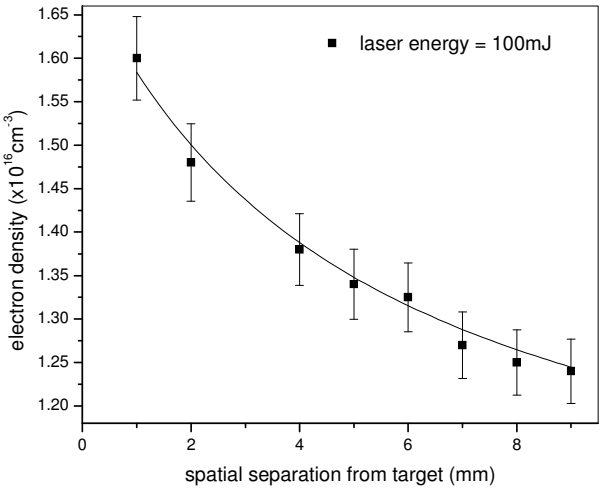

Fig. 2.10: Spatial variation of n_e with 100mJ of laser energy; dotted line shows the theoretical fit based on an inverse z dependence for n_e .Source – LIP from TiO_2.

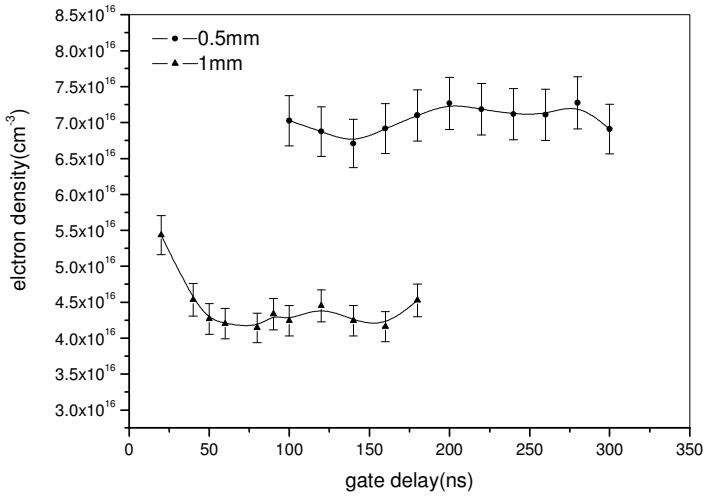

Fig. 2.11:Temporal evolution of n_e from TiO_2 plasma. (Energy of laser beam is 100mJ)

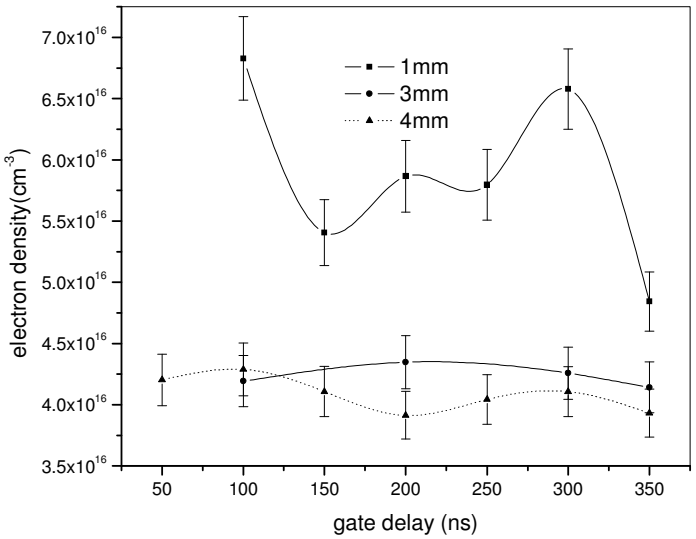

Fig. 2.12: Spatio-temporal electron density evolution in TiO_2 plasma at 200mJ.

The time evolution of line intensities is extracted within a time range extending up to 300ns after the plasma initiation. The typical temporal spectra evolution is shown in figure 2.13. Majority of the emissions are from Ti I and Ti II. The spectral line kinetics of (a) 343.9nm (Ti I), (b) 347.8nm (Ti I), (c) 349.1nm (Ti II), (d) 350.5nm (Ti II), (e) 351.1nm (Ti II), (f) 352nm (Ti II), (g) 353.5nm (Ti II), (h) 357.3nm (Ti II), (i) 358.7nm (Ti II) and (j) 359.6nm (Ti II) are presented. By the analysis of this figure, it is possible to observe the initial spectral continuum, essentially due to collisions of free electrons with heavy particles and radiative recombination of electrons with positive ions. Each fragment of the spectra belongs to a different portion of the LIP temporal distribution.

The emission lines become progressively narrower as a consequence of the change in electron number distribution. The FWHM of a few representative lines, measured at different delay times are shown in Fig.2.13A. It shows that the excitation temperatures must decrease during the time evolution. The maximum intensity is reached after a characteristic time of 90ns, which depends on the observation distance and this represents the most populated section of LIP. As a consequence of the high degree of ionization, for most part of the spectra, the ionic lines are proportionally more intense than those of the atoms, while on the tail of the temporal distribution of LIP intensities, which correspond to the colder part of the plasma, it is possible to observe the progressively disappearing atomic lines.

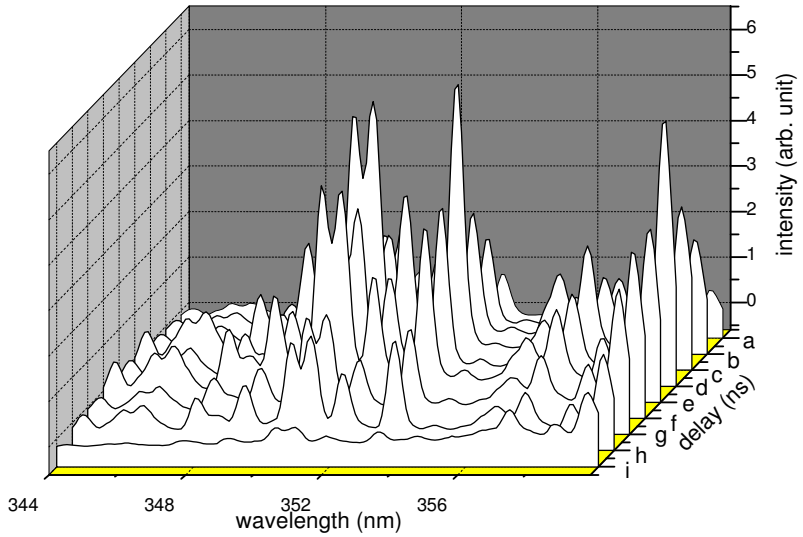

Fig. 2.13:Temporal evolution of a typical Ti spectrum at distance 1mm from the target. (a)20ns (b)50ns (c)60ns (d)90ns (e)100ns (f)120ns (g)140ns (h)160ns(i)180ns.

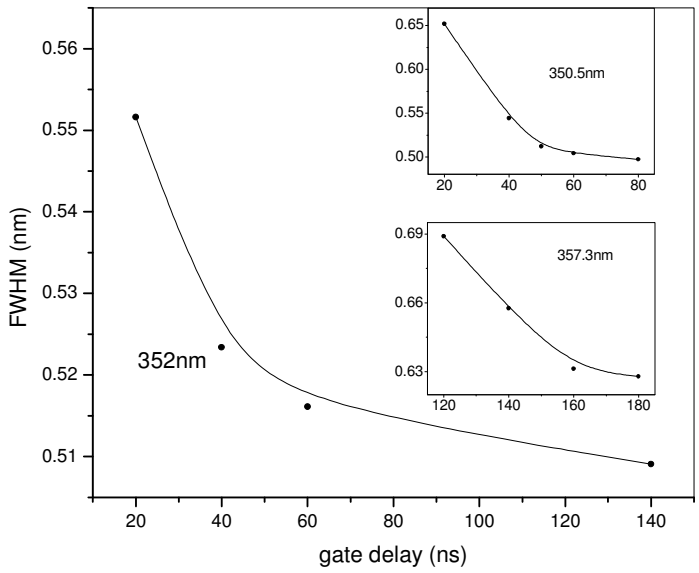

Fig.2.13A: Progressive narrowing of emission line width (352nm), as the plume evolves in time, at 1mm from the target. Inset shows the narrowing feature at 350.5nm and 357.3nm.

The experimental measurement on pure metallic target of titanium (Fig:2.14) shows that density values are lying between definite limits with minimum fluctuations, during 150ns to 350ns except at 1mm separation from the target, where the density is relatively high.

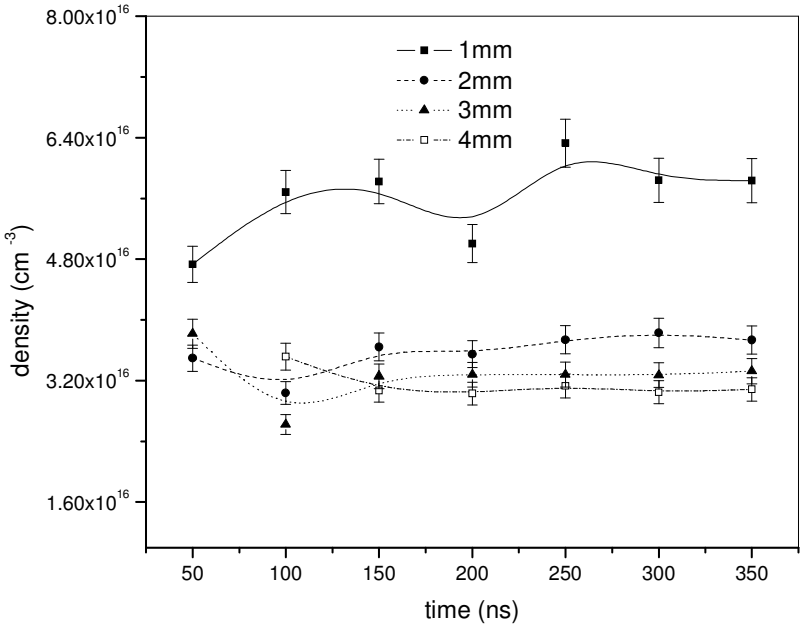

Fig.2.14: Time evolution of electron density of pure metallic target of titanium at 100mJ.

2.3.3. Time and space evolution of plasma temperature: Boltzmann plot method

The electron temperature distribution within time range of upto 350ns is also calculated. While evaluating the electron temperature by this method, it is important to verify that the plasma is not optically thick for the lines used. This was done by checking the ratio of emission intensities at the wavelengths, according to a procedure described by Radziemski et al [17]. The intensities were observed to be in a ratio that is consistent with the ratio of their statistical

weights, which indicates that the plasma was optically thin. The resultant temperature is a population-average temperature as discussed by Boumans [18]. Farther the observation distance from the target (towards the laser beam), colder is the plasma, as depicted in Fig.2.15, due to the expansive dissipation of the plume energy. At a distance of 1mm, the temperature of the tail of the temporal distribution falls down to 1eV from the initial value of 1.2 eV. At 0.5mm from the target, the initial temperature is greater than this. As we go ahead from the target surface, at farther distances, the temperature begins to rise at later times. This can be attributed to the recombination processes which compensate the expansive cooling. With laser energy of 200mJ, the evolved temperature is shown in Fig.2.16. The sudden electron temperature increase at 300ns is due to the laser energy absorption that occurs during the laser – plasma interaction. This can be explained by atom – atom collisions at greater distances from the target [19]. Such an increase can flourish only with tolerable decay rates. But, even at 3mm distance, the recombination rate is not dominant and the increased electron temperature decays faster.

Time integrated measurements are done to evaluate the spatial variation of electron temperature from the target. The measured distribution functions can be represented in good approximation in a Boltzmann form. Assuming a Boltzmann distribution, the plasma temperature can be determined using Boltzmann plot technique using the measurements of spectral intensities (I_{mn}) by the following equation, representing an energy transition from an upper energy state m to a lower state n.

$$\ln\left\{\frac{I_{mn}\lambda_{mn}}{A_{mn}g_m}\right\} = \ln\left\{\frac{N}{2}\right\} - \left\{\frac{E_m}{kT_e}\right\} \tag{2.2}$$

The parameter λ_{mn} is the transition wavelength, A_{mn} is the transition probability, E_m and g_m are the energy and statistical weight of the upper level respectively. The temperature is obtained from the slope of the plot of $\ln\left\{\frac{I_{mn}\lambda_{mn}}{A_{mn}g_m}\right\}$ Vs E_m. We have chosen three transitions of Ti II with well separated upper energy levels in order to determine kT_e. The selected transitions along with their characteristic parameters are listed in table 2.1.

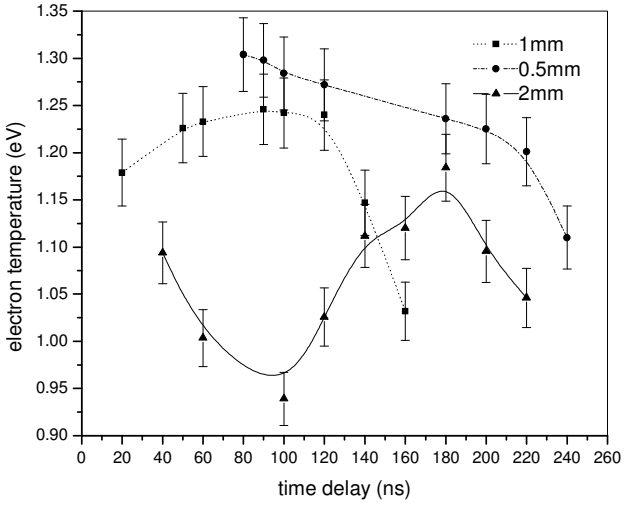

Fig. 2.15: T_e evolution at 100mJ as a function of time. Source: LIP from TiO_2 target.

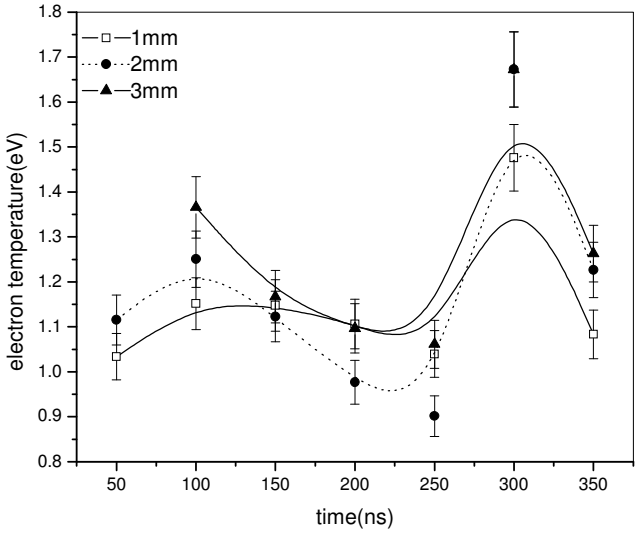

Fig. 2.16: Distribution of electron temperature at a laser energy of 200mJ. Source: LIP from TiO_2 target.

wavelength (nm)	$A(s^{-1})$	g_m	species	E_m (eV)
346.1	$6.27x10^6$	10	Ti II	3.71
348.4	$9.7x10^7$	8	Ti II	7.85
350.5	$6.5x10^5$	10	Ti II	5.42

Table 2.1

The spatial variation of the electron temperature shown in Fig.2.17 is typical with a rapid decay near the target and a slowly varying function of space at larger distances. The lowering of the decay rate of temperature at larger distances is mainly due to the energy gained from three body recombination that compensates the expansive cooling [20]. The calculations are based on the assumption that the emitting species are in collision equilibrium with the electrons and self-absorption for the chosen spectral lines which is due to the absorption by the atoms in the lower level of the transition are neglected.

We confirm the validity of Mc Whirter criterion [21] in the present experiment, which states that the minimum density of LTE should be,

$$n_e \geq 1.4\times10^{14} T_e^{1/2} \left(\Delta E^3\right) \text{ cm}^{-3} \tag{2.3}$$

where T_e and ΔE are in eV. For the transition with the largest energy gap of 3.574 eV, applying the peak plume temperature of 1.67eV to this criterion predicts a lower limit of 8.25 x 10^{15} cm^{-3} for n_e. Our observed n_e values are always greater than this lower bound, implying that LIP from TiO_2 target, under the present experimental conditions validates LTE.

Within the range of laser fluence and temperature studied, excited species of Ti II are prominent in the LIP from TiO_2 target. Spectral lines of oxygen or molecular species are not observed under the present experimental conditions. Majority of the emissions are due to Ti II during the interval upto 180 ns. At a spatial separation of 1mm from the target, the most populated section of LIP emerges after 90ns.

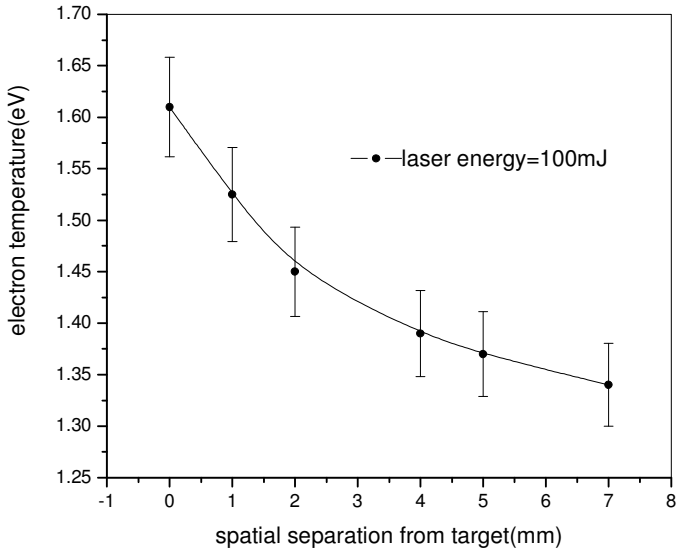

Fig.2.17: T_e distribution in TiO_2 plasma at 100mJ.

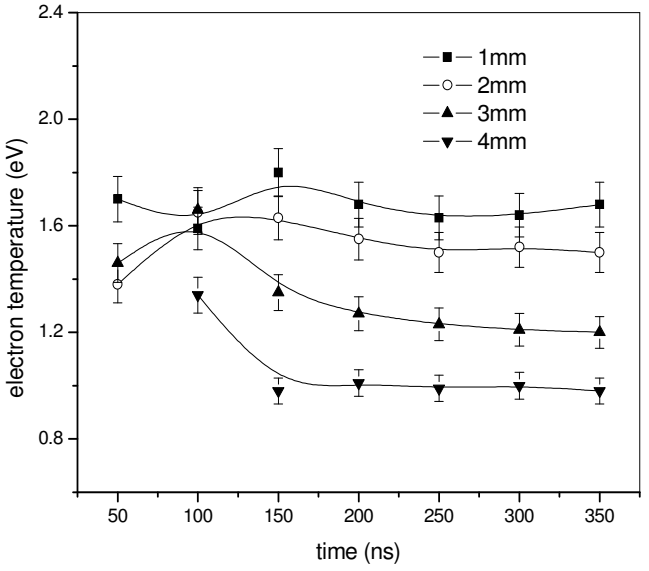

Fig. 2.18: Temporal variation of electron temperature at 100mJ. LIP target is titanium metal

For the plasma produced using pure metallic target of titanium, the electron temperature in the region from 1mm – 4mm lies between 0.8eV and 1.8eV during the

first 350ns. After 150ns, the electron temperature at each spatial point shows steady values under the present experimental conditions (Fig: 2.18).

2.4. Aluminium oxide and aluminium

Plasma ignition threshold of aluminum is approximately 0.3 $GWcm^{-2}$ [22]. But at irradiance above 10 $GWcm^{-2}$, a threshold seems to occur indicating a significant change in plasma dynamics from normal ablation to explosive boiling. The sudden change in the mechanism is responsible for vapor and particle formation above the sample surface and subsequent laser plasma interaction. When the laser energy deposited onto the sample is larger than the value required for reaching the critical temperature, the excess of laser energy is directly coupled with the sample and the amount of ablated material is significantly increased.

2.4.1.Time of flight for plasma species

An ionic line of aluminium has been selected for the temporal measurement of line shapes. This line corresponds to the emission from the first excited state (*Al II*) for the transition 3s.4p $^3P^0_2$ – 3s.4d $^3D_3$. For this emission at 624.3nm, the transition probability value is very high, compared to the nearer transitions. The time of flight spectrum is shown in Fig.2.19.

With aluminium oxide target, the expansion velocity is large at distances very close to the target surface and shows irradiance dependence. But at locations away from the target surface, steady cooling occurs in the plasma (at 6mm, the plasma temperature is calculated as 1.3eV). Due to this cooling, the temperature falls below the ionization energy and three body recombination dominates collisional recombination, in the plume regions at larger distances [23]. But at distances below 5mm, collisions are highly prominent and the high initial kinetic energy values of the species are degraded. Beyond 5mm, the expansion velocity of aluminium ions increases slightly with distance up to 14mm but in a steady manner (Fig.2.20). With metal target, the electron density falls (Fig.2.24) with distance from target and the ionic species show that the plasma is freely expanding (Fig.2.21).

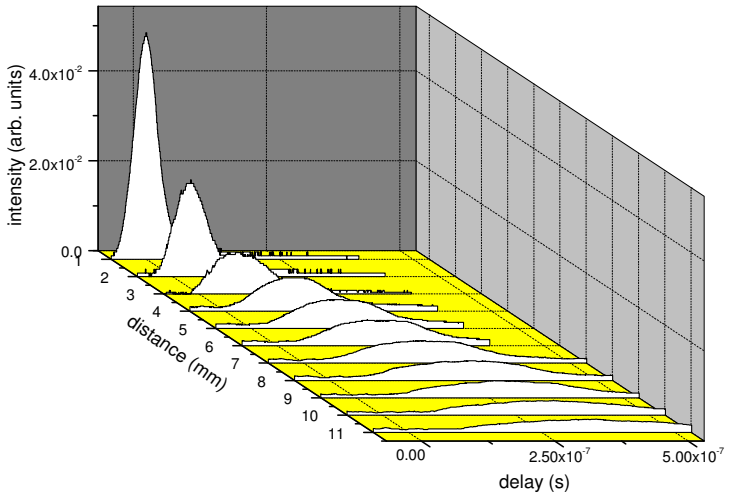

Fig. 2.19: Flight of AlII from 1mm to 11mm in aluminium oxide plasma at 200mJ laser energy

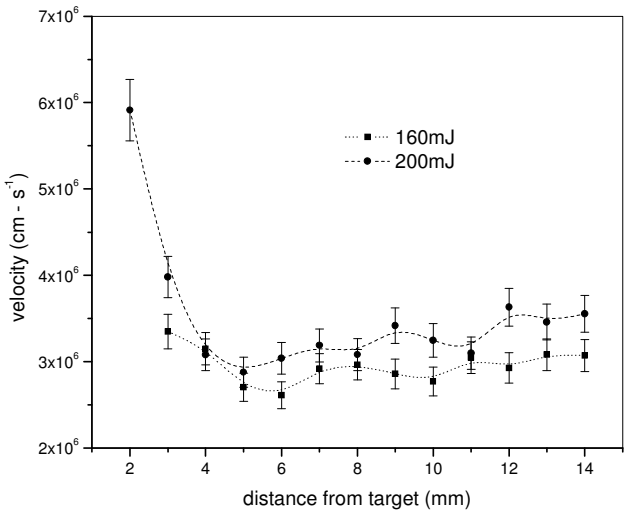

Fig. 2.20: Expansion velocity of aluminium ions in aluminium oxide LIP at different laser energies

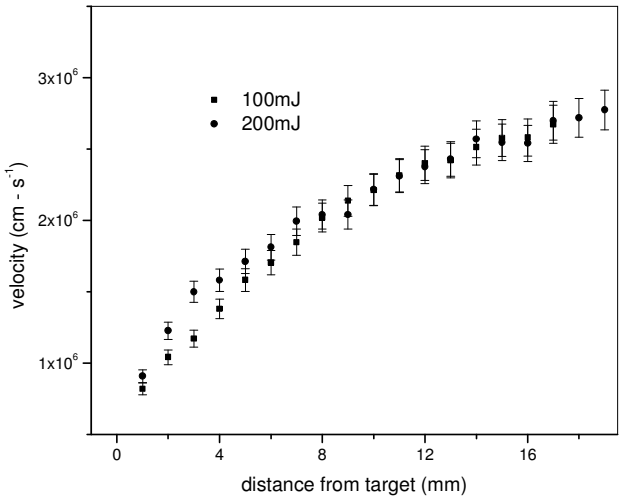

Fig. 2.21: Free expansion of ionic species in LIP of metallic aluminium

The reduced rate of collisions prevents the sudden cooling of plasma as evident from the rapid decrease in emission intensity in the beginning which then becomes very slow (Fig.2.22).

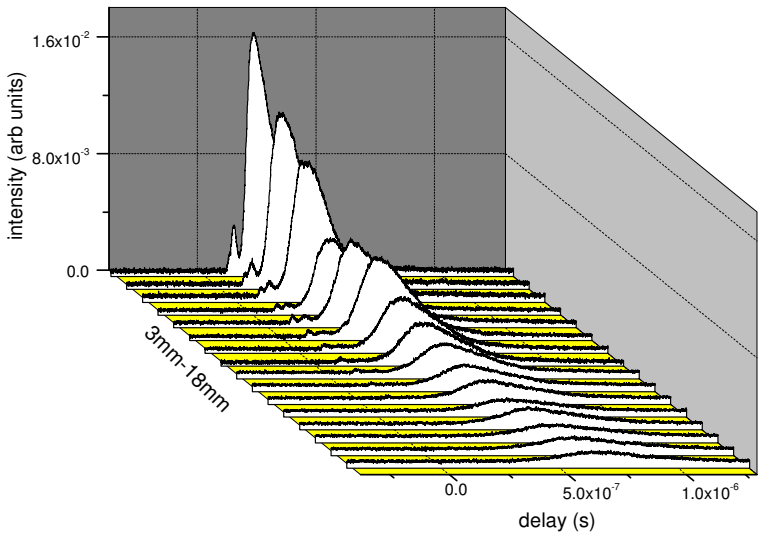

Fig. 2.22: Slow decay of emission intensity at farther plasma slices in aluminium LIP

2.4.2. Development of electron density in space and time

Line broadening and shifting are the result of interaction between emitting species and surrounding electrically charged species (Stark effect), while other possible contributions could be the instrumental broadening, resonance broadening, Doppler and van der Waal's effect [24]. Stark broadening of the line is mainly due to the influence of the free electrons surrounding the emitting particle, that of the surrounding ions being of less importance. The Stark broadening of the neutral aluminium species in the plasma is considered for evaluating the electron density evolution in space and time. All other contributions to the total line width have been neglected in doing this. The line corresponds to the *Al I* emission at 396.2nm, from the transition $3s^2.3p\ ^2P^0_{3/2} - 3s^2.4s\ ^2S_{1/2}$. The spectroscopic data used for the evaluation were retrieved from NIST electronic database [25]. Two sets of measurements are done – density from near field emissions (1mm-6mm) and density from far field (>6mm) emissions. Higher electron density is observed above the oxide surface than the corresponding metallic surface under the most identical situations (Fig. 2.23-2.24).

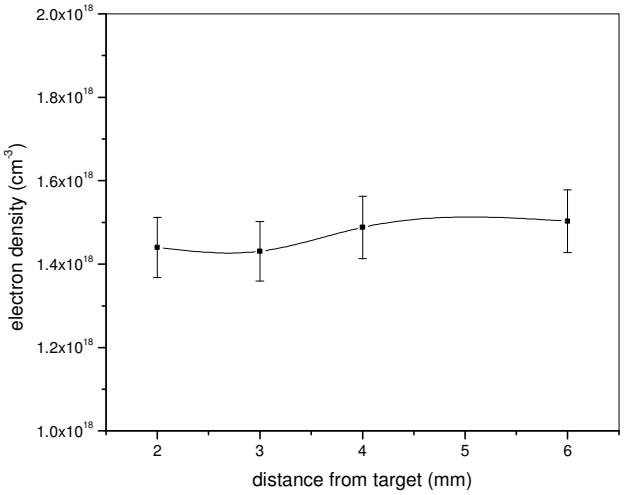

Fig.2.23: Time integrated electron density in the near field of LIP over aluminium oxide target

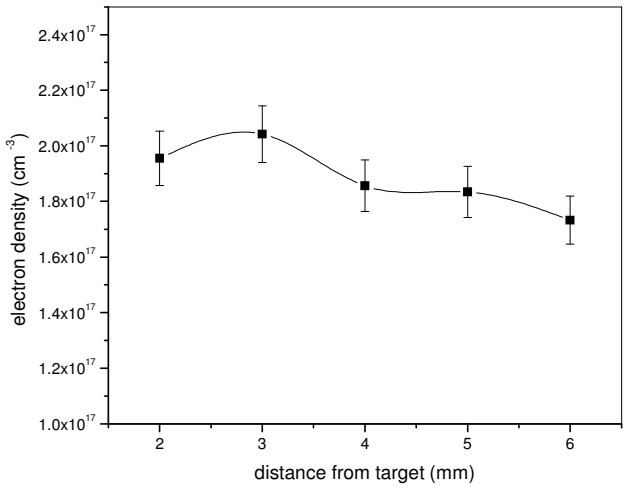

Fig. 2.24: Time integrated electron density. Source – near field emissions from LIP over metallic aluminium target

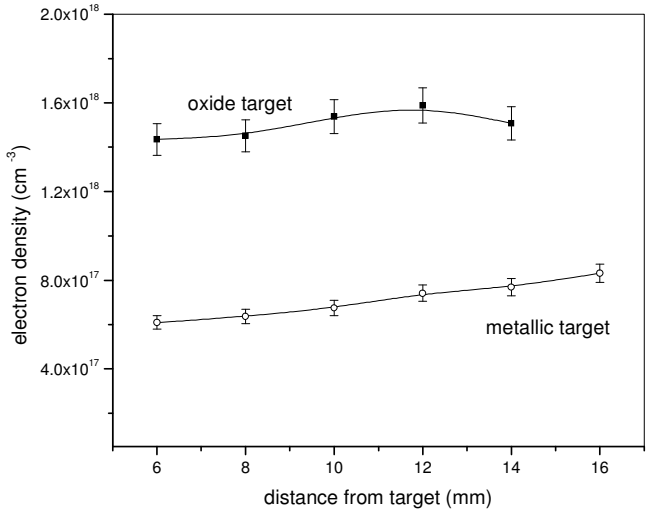

Fig. 2.25: Time integrated electron density in far field region of aluminium LIP

At intermediate distances, the evolved local electron density is preserved without much variation, within the measured time range (Fig.2.26-2.27).

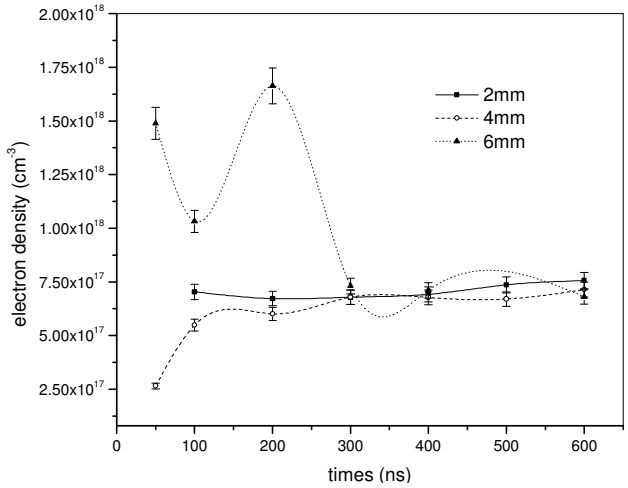

Fig. 2.26:Local electron densities in Aluminium LIP at different times

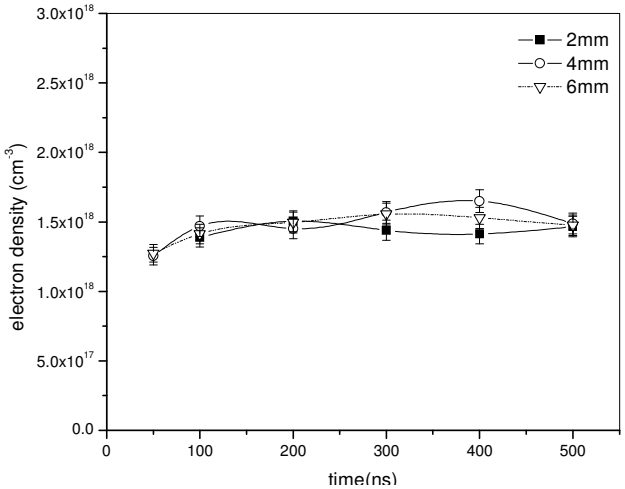

Fig. 2.27: Time dependent variation of local electron densities in the LIP from oxide target of aluminium

In aluminium oxide plasma, the density is lying between $1.4x10^{18}cm^{-3}$ and $1.5x10^{18}\,cm^{-3}$, before 6mm, during its time evolution between 200ns and 500ns. But for the metallic target, the plasma density reaches a high value ($\approx 10^{18}\,cm^{-3}$) between 200ns and 500ns and again falls with distance at 500ns (Fig.2.28-2.29).

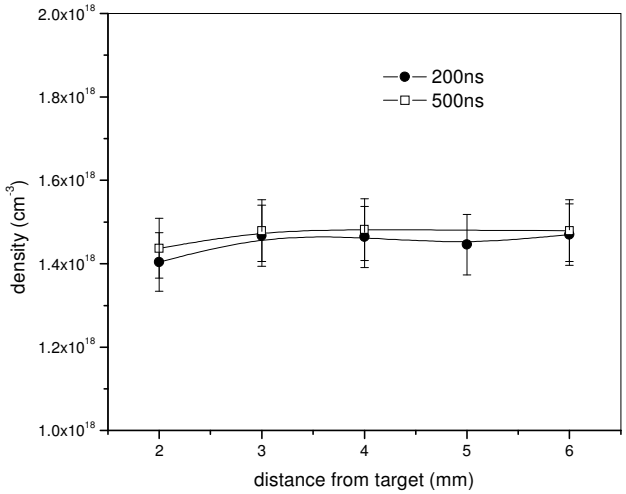

Fig. 2.28: Time resolved variation of spatial electron density. (source – LIP from aluminium oxide target)

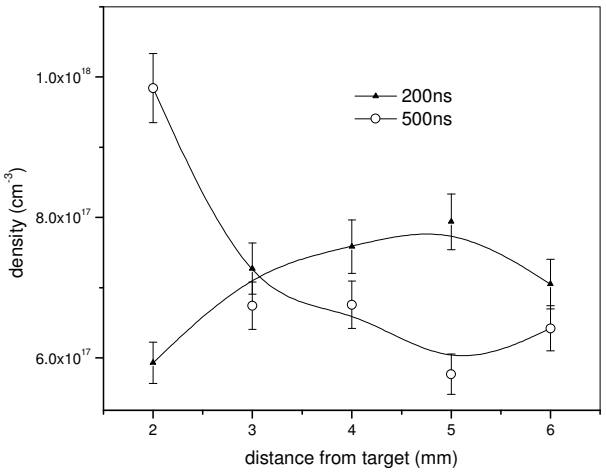

Fig. 2.29: Time resolved variation of spatial electron density. (source – LIP from aluminium metal)

From the density measurements made on the emissions collected in the far field (beyond 6mm distance from target surface) of the plasma, a density fall can be observed at later times (Fig 2.30-2.31). Another important feature observed is that the electron density profiles stretch over a longer distance as time increases, as a result of plasma expansion (Fig 2.30).

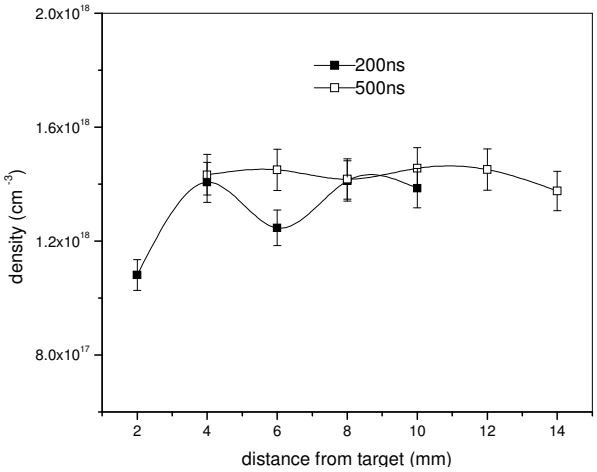

Fig. 2.30: Time resolved variation of spatial electron density extending up to far field of plasma. (source – LIP from aluminium oxide target)

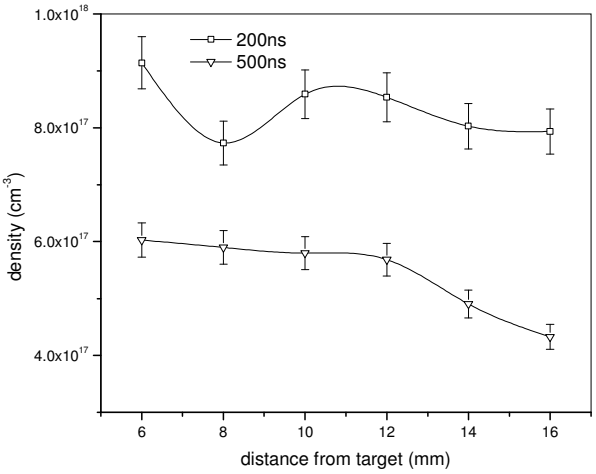

Fig. 2.31: Time resolved variation of spatial electron density. (source – far field region of LIP from aluminium metal)

As the plasma evolves between 200ns and 700ns, the range of plasma density variation is shortened in space, beyond 6mm (Fig.2.32). A flattening of the curve is also noticed at later times.

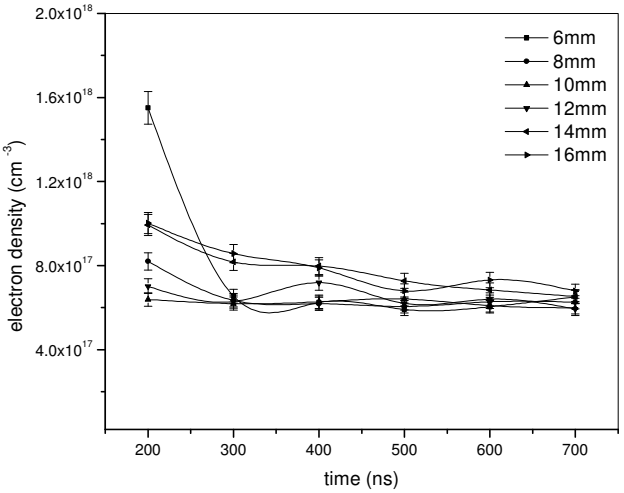

Fig. 2.32: Progressive flattening of electron density profile as time advances. Source – far field region of LIP from aluminium metal)

Considering that the plasma geometry is hemispheric [26], each axial position corresponds to plasma slices of different transverse extensions (hence volumes). As a consequence, the profile flatness suggests that the electron density is spatially homogeneous in the time range. These results do not contradict results obtained by other authors since as far as we know there is no report in the literature of time- and space-resolved electron density values for delays shorter than 1µm in the spatial range extending upto 16mm.

2.4.3. Evaluation of plasma temperature from line intensities of subsequent ionization stages: space and time evolution

The Boltzmann plot method is difficult to implement in this case as the lower energy levels of most of the experimentally convenient transitions are not well separated. This renders the line intensity ratios insensitive to temperature changes. Considerable improvement in the sensitivity is obtained if lines from successive ionization stages of the same element are compared with each other, because the effective difference is now enhanced by the ionization energy, which is larger than the thermal energy. In LTE, the ratio of such line intensities (I) follows the equation [27]:

$$\frac{I'}{I} = \frac{f'g'\lambda^3}{fg\lambda'^3}\left(4\pi^{3/2}a_0^3 n_e\right)^{-1}\left(\frac{kT_e}{E_H}\right)^{3/2}\exp\left(-\frac{E' + E_\infty - E}{kT_e}\right) \qquad (2.4)$$

Primed quantities in equation:2.4 refer to the line from the higher ionization stage, E_∞ is the ionization energy of the lower ionization stage, E_H is the ionization energy of hydrogen atom, a_0 is the Bohr radius, n_e is the free electron density, T_e is the electron temperature, g is the statistical weight and f is the oscillator strength.

The line intensities of Al I at 394.4nm ($3s^2.3p\ ^2P^0_{1/2} - 3s^2.4s\ ^2S_{1/2}$) and Al II at 390.1nm ($3s.3p\ ^1P^0_1 - 3p^2\ ^1D_2$) are compared in the spectroscopic evaluation procedure for temperature measurement. The presence of neutral lines characterizes the existence of non-ionized ablated matter in the plasma. The time integrated temperature falls with distance from the target (Fig: 2.33). Despite the expansive cooling, the decay rate falls, as the spatial point is more and more separated from the target. This may be due to the energy gained from three body recombinations [21].

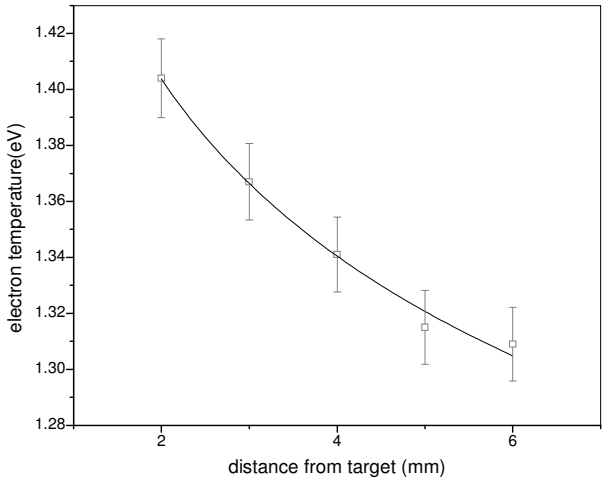

Fig. 2.33:Time integrated temperature values. Source – near field region of LIP from aluminium oxide.

This fact is also supported by the time resolved measurements (Fig: 2.34-2.35).

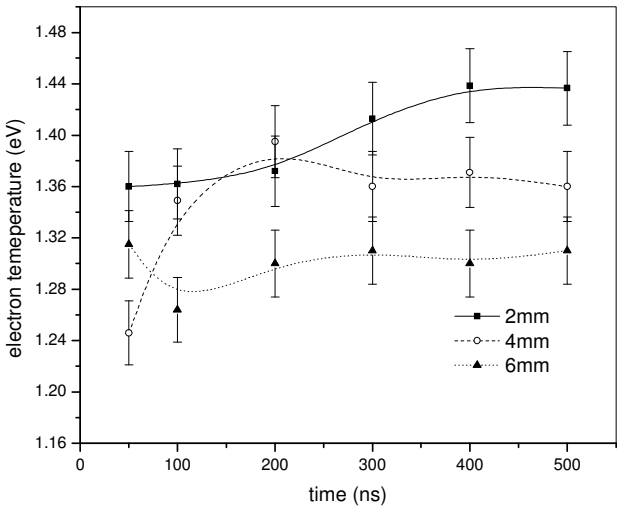

Fig. 2.34: Time resolved temperature plot of aluminium oxide LIP showing fall of temperature with distance from target.

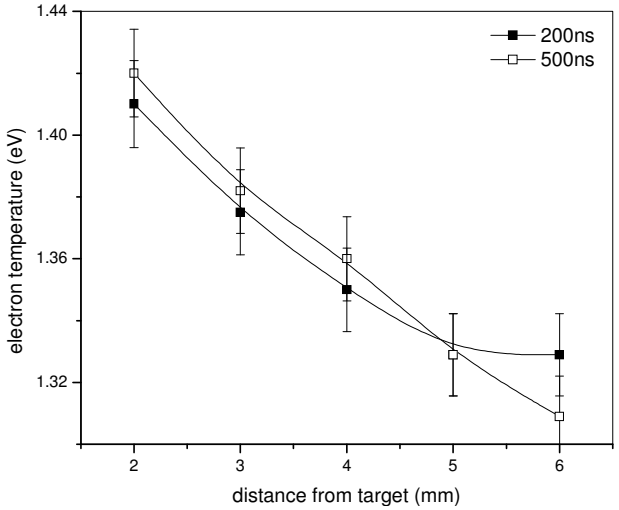

Fig. 2.35: Spatial variation of temperature in aluminium oxide LIP at different times

But for the plasma induced from the corresponding metallic target, a temperature drop is noticed at the target side. One of the reasons for the temperature drop noticed at the target side, at nearer spatial points is due to the thermal conduction from the plasma towards the solid target. The lowered temperature tries to build up even at nearer distances from the target as seen in the time resolved temperature values (Fig.2.36-2.37).

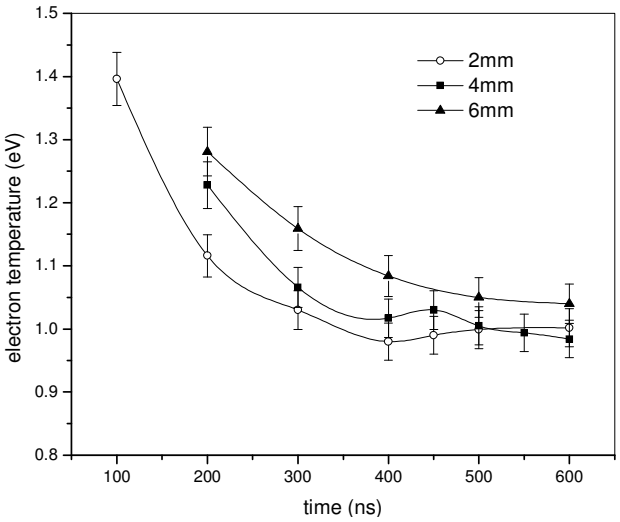

Fig. 2.36: Time resolved temperature plot of metallic aluminium LIP showing temperature drop at the target side.

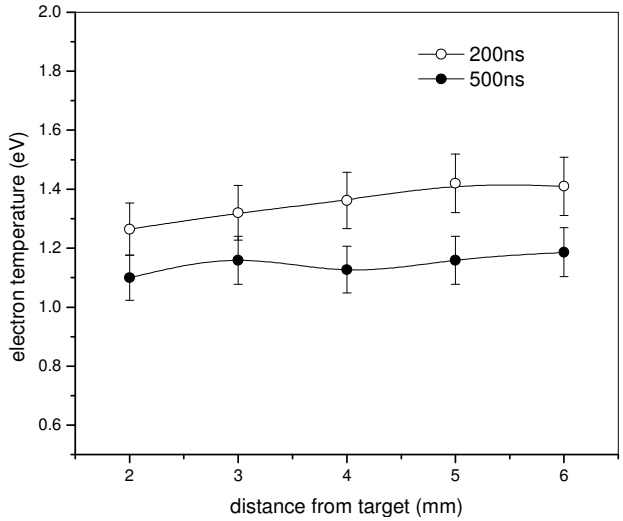

Fig. 2.37: Levelling of temperature in metallic aluminium LIP at intermediate spacial points (3-6mm).

At large spatial separations from the target, the time integrated temperature increases slightly. This is evident from the measurements on both types of aluminium targets (Figs. 2.38-2.39). This fact is also supported by the corresponding time resolved measurements (Figs. 2.40-2.43).

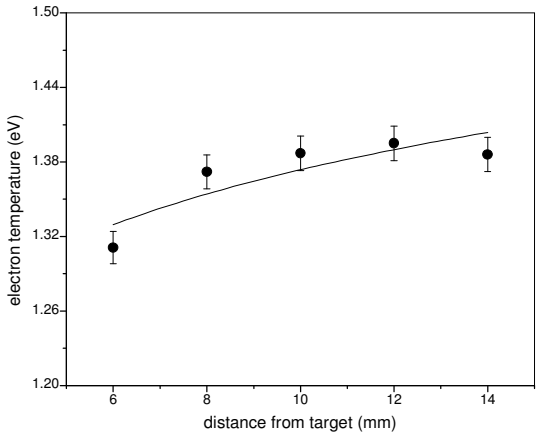

Fig. 2.38: Time integrated temperature values. Source – far field region of LIP from aluminium oxide.

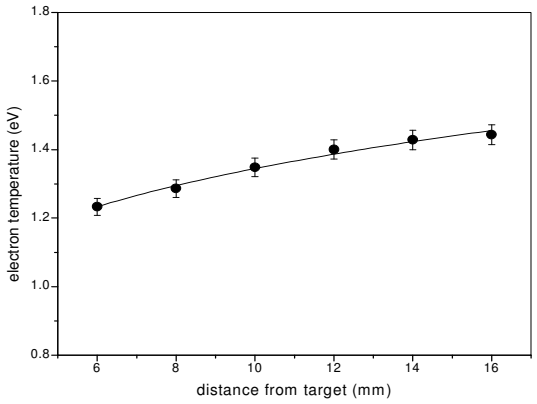

Fig. 2.39: Time integrated temperature values. Source – far field region of LIP from aluminium metal.

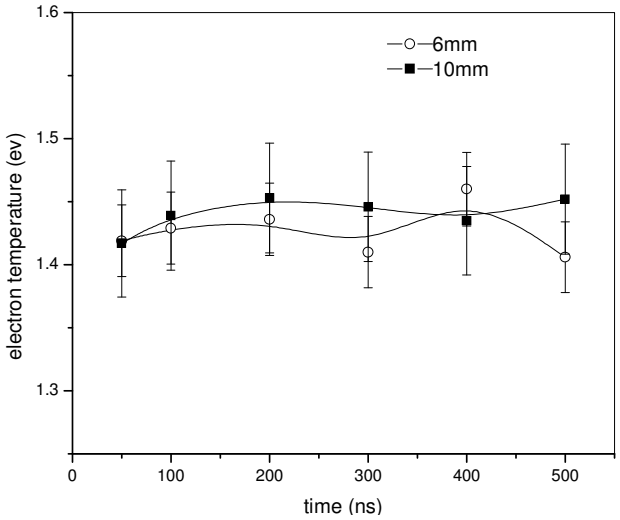

Fig. 2.40: Time resolved temperature. Source – far field region of aluminium oxide LIP

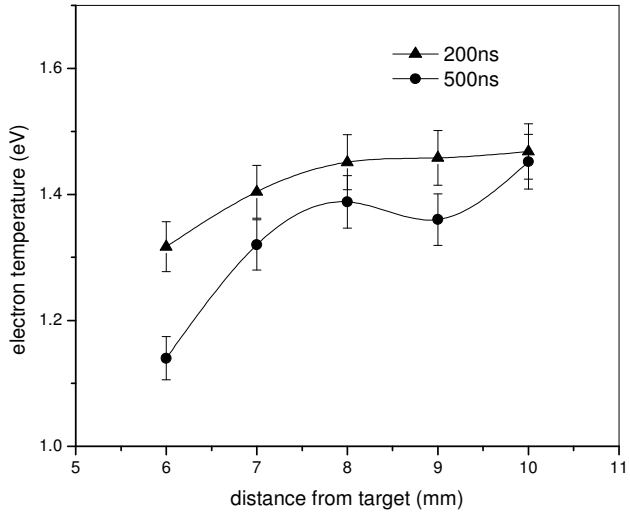

Fig. 2.41: Increase of temperature at large spatial separations. Source – far field region of aluminium oxide LIP.

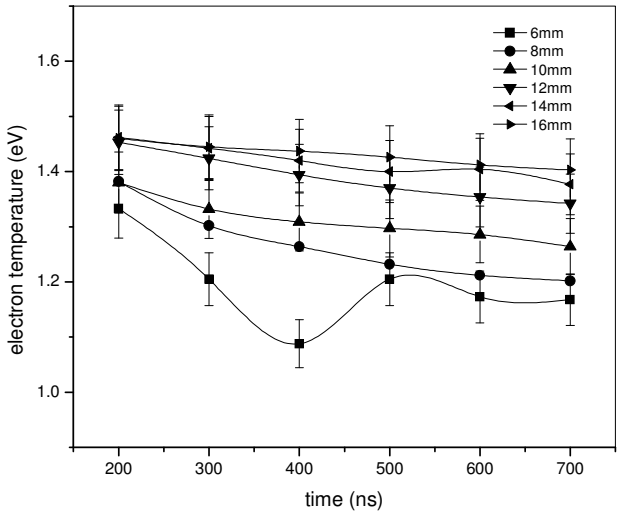

Fig. 2.42: Time resolved temperature. Source – far field region of metallic aluminium LIP.

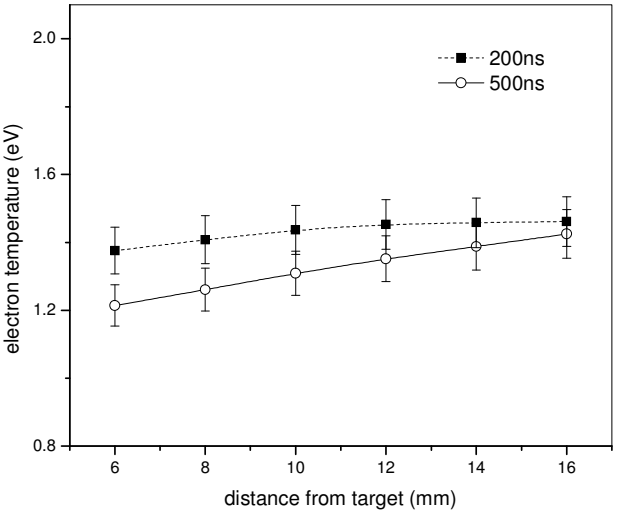

Fig. 2.43: Slight temperature increase at large spatial separations. Source – far field region of metallic aluminium LIP.

The temperature near the target shows steady decrease but at distances greater than 6mm, the temperature is found to increase. As the plume expands freely into vacuum, plume species move with different expansion velocities. The differential expansion becomes noticeable at farther spatial points and the separated species collide less frequently with one another. This reduces the rate of temperature equilibration and cooling. This fact is also responsible for the noted temperature increase.

The temperature drop at the plasma edge (on the right) is essentially due to radiative cooling, which is higher in this area as a consequence of the larger emitting surface. Heat conduction from the plasma to the ambient air also contributes to the plasma cooling at the front edge of the plasma. [28-32]. At early times, when the plasma is hot and dense, both plasma cooling effects are more significant than at later times, when thermal and radiative conduction have smoothed out the temperature gradients and lowered the plasma temperature values. The plasma temperature evolution at late times is largely determined by the cooling mechanisms (mainly radiation losses toward the ambient air) so that nearly the same ‘‘asymptotic state’’ is reached some time after the laser shot, whatever may be the initial conditions [31]. The leveling off of the temperature, amidst the expansive cooling at larger distances is mainly due to the energy gained from three-body recombination.

2.5. Tin oxide and tin

2.5.1. Emission profiles with pure and oxide targets

Two lines of *Sn* I, 452.5 nm with transition probability 2.6 x 10^7 s^{-1} ($5p \cdot 6s \ ^1P_1^0 - 5p^2 \ ^1S_0$ transition) and 615.5 nm with transition probability 11 x 10^6 s^{-1} corresponding to the transition, $6s \ ^1P_1^0 - 7p \ ^1D_2$, were selected for TOF measurements of neutral tin species. For investigating the flight of charged species in the plasma, two *Sn* II lines were selected. 559.6 nm line is arising out of the transition, $5s^2 \cdot 6d \ ^2D_{3/2} - 5s^2 \cdot 6p \ ^2P^0{}_{3/2}$, with transition probability 1.5 x 10^7 s^{-1} and 645.3nm $\left(5s^2 \cdot 6p \ ^2P^0{}_{3/2} - 5s^2 \cdot 6s \ ^2S_{1/2}\right)$ line has the transition probability 8 x $10^7 s^{-1}$. A typical plot for the flight of neutral species is presented in fig: 2.44.

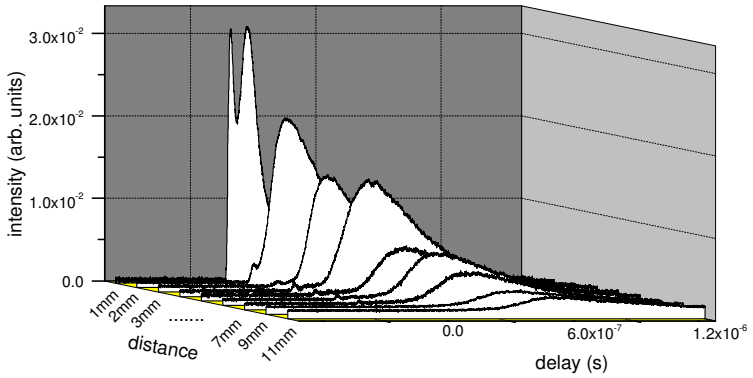

Fig. 2.44: Time of flight of neutral tin species (615.5nm) in tin oxide LIP

The expansion velocity of various plasma species is closely related to their charge states as well as their masses. The species with higher charge states move with high velocities compared to their counterparts with lower charge states [33, 34, 23].

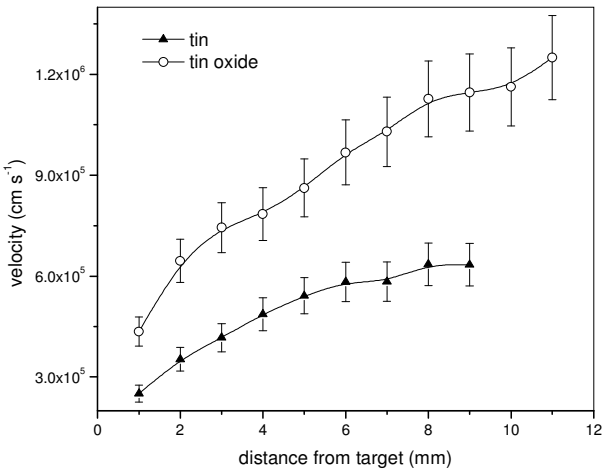

Fig. 2.45: Expansion (normal to target surface) of neutral species in tin and tin oxide targets.

During TOF separation, the observed velocity of flight of charged species is proportional to the square root of their charge to mass ratio. The observation that velocity of the neutral species are always lower than the singly ionized species is

made about LIP from pure metallic tin as well as tin oxide targets. But under the same conditions of vacuum and irradiance, neutrals and singly charged ions in the LIP from oxide targets gain comparatively higher flight velocities (Fig.2.45-2.46).

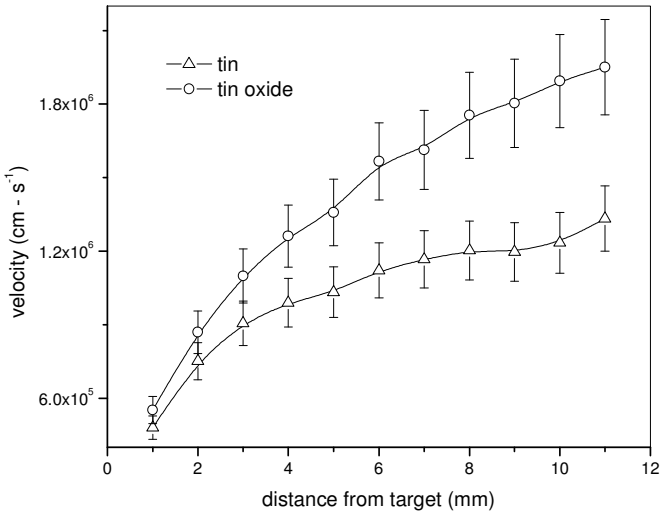

Fig. 2.46: Flight velocity of ionic species during forward expansion. Source – LIP from tin oxide.

2.5.2. Electron density evolution in space and time scales

Spectral measurements were made at sequential distances from the target surface upto 20mm. Spectral and line shape analyses were made at different distances from the target surface, on the Sn II line $\left(6p\ ^2P^0_{3/2} - 6d\ ^2D_{5/2}\right)$ at 556.2nm. The time integrated measurements are indicative of the average local conditions while the time resolved measurements are defining the conditions at a particular stage of the plasma's evolution. In tin plasma, density falls immediately up to 6mm, builds up slightly and thereafter the decrease is slow but (beyond 6mm) the oxide target develops a fluctuating density**,** about a mean value (Fig:2.47-2.48). This feature could be related to the change of the cooling mechanism from plasma propagation to recombination [35, 36].

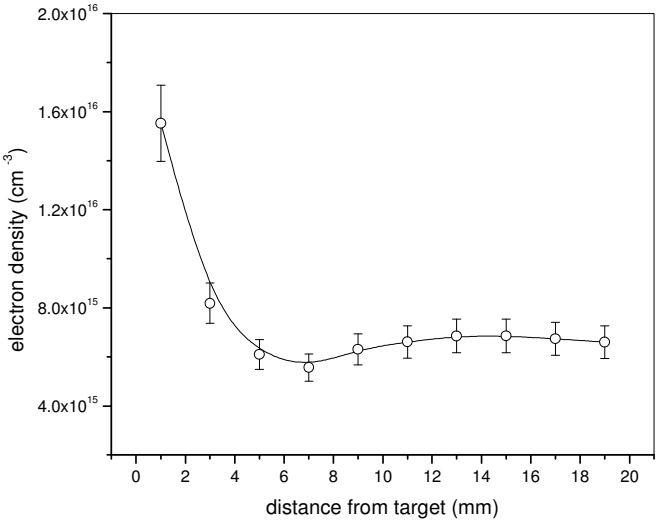

Fig. 2.47: Time integrated electron density in tin LIP.

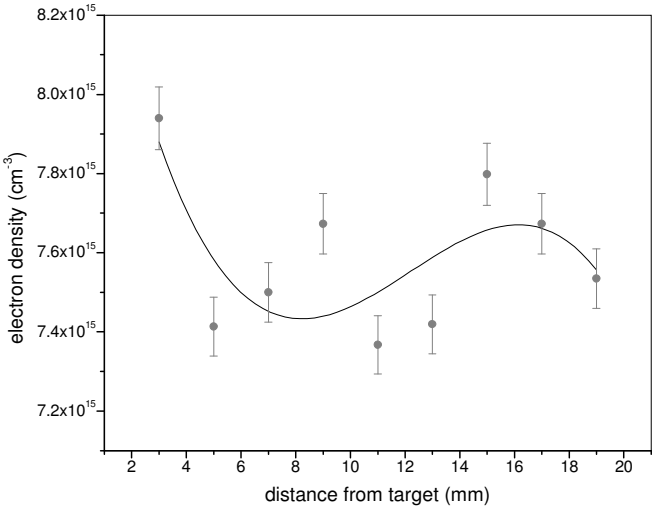

Fig. 2.48: Ttime integrated electron density in tin oxide LIP.

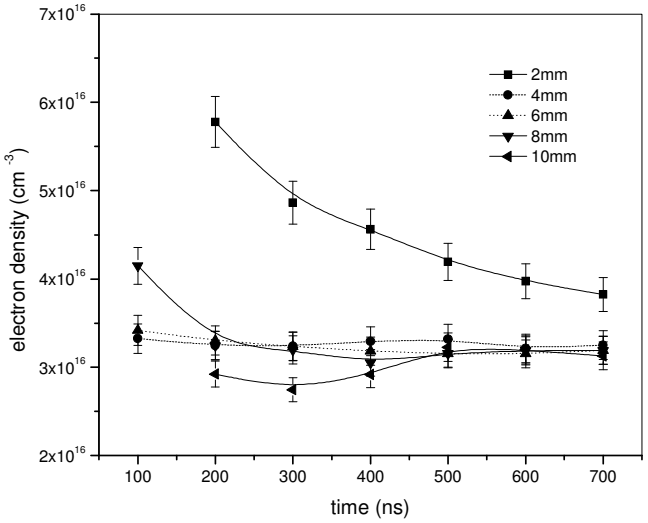

Fig. 2.49: Evolution of electron density during the initial expansion stage of tin LIP.

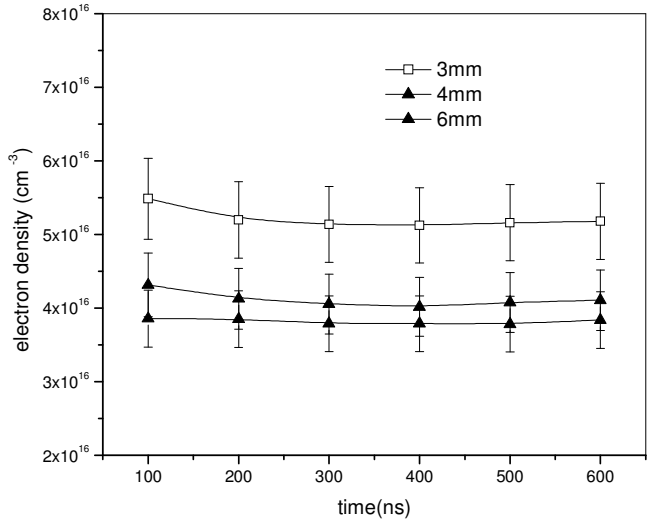

Fig. 2.50: Time evolution of electron density during the expansion of tin oxide LIP.

It is seen that the density attain its peak value close to the target surface within the first 100ns and then decrease due to the plume expansion. Initially the plasma expands isothermally during the laser pulse. After termination of the pulse, no more energy is pumped into the plasma. The thermal energy is converted into directed kinetic energy and the plasma cools through adiabatic expansion. After the plasma formation, the electron density over the LIP of both pure metallic and oxide targets of tin evolves nearly uniformly in time (between 200ns and 700ns) except at points closer to target surface, which shows relatively high values of density (Fig.2.49-2.50).

2.5.3. Calculation of plasma temperature along resolved space and time

It can be observed that somewhat larger data dispersion occurs in the evaluated T_e values, as compared to the electron density. This is due to the method (Boltzmann plot method) employed to extract the temperature, which requires the observation of seven spectral lines of various intensities, rather than only one for the determination of the electron density. Table 2.2 gives the spectral details used for calculating electron temperature.

wavelength (nm)	$A(s^{-1})$	g_m	species	E_m (eV)
556.2	13×10^7	6	Sn II	11.2
645.4	6.6×10^7	4	Sn II	8.97
684.4	6.1×10^7	2	Sn II	8.86

Table 2.2

A spectral response curve of the spectrograph+PMT, recorded in the region 400nm - 700nm has been used to calibrate the experimental line intensity values for the spectroscopic temperature measurement.

For tin targets, the temperature plot at 2mm is flat compared to 6mm where an increase of temperature is detected at later times (Figs.2.51-2.52).

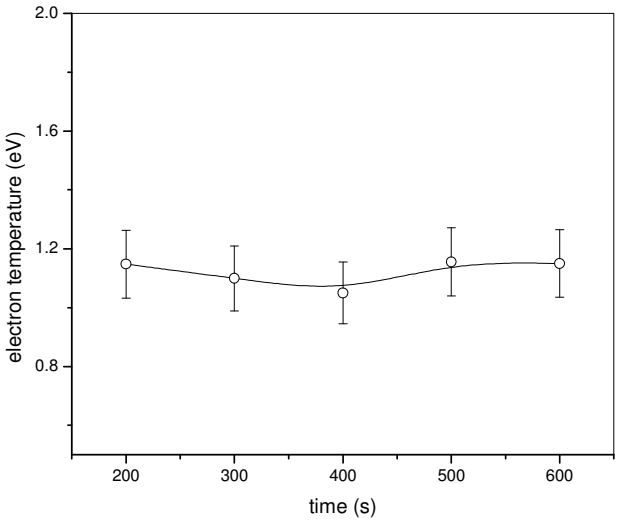

Fig. 2.51: Nearly flat time profile of electron temperature in tin LIP at 2mm.

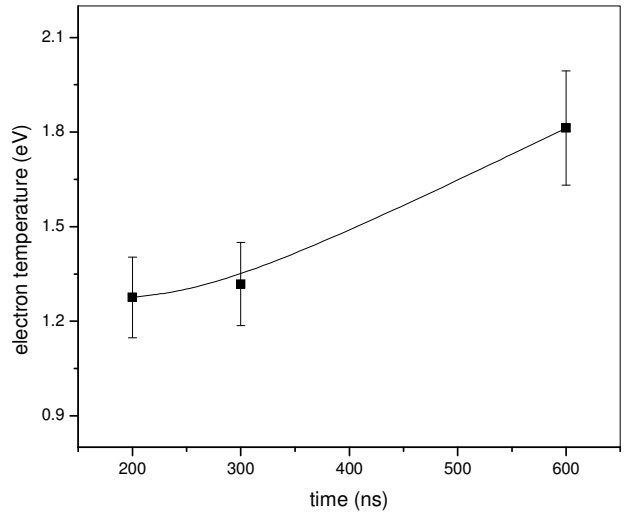

Fig. 2.52: Increase of electron temperature in tin LIP at 6mm as time evolves.

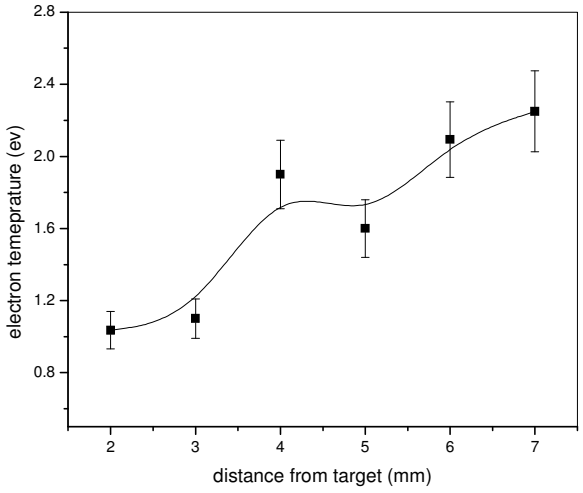

Fig. 2.53: Rise in electron temperature detected at farther spatial points of tin LIP during 500ns.

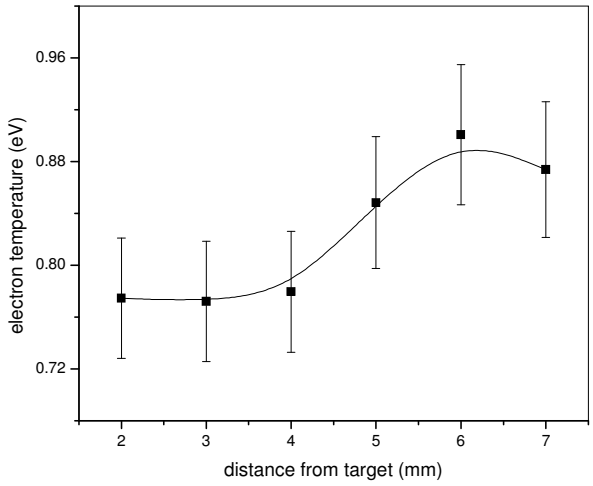

Fig. 2.54: Electron temperature increase at farther spatial points of tin oxide LIP at 500ns.

Except at spatial points closer to the target, a gradual rise in temperature is detected in LIP with both kinds of samples as targets (Figs.2.53-2.54)**.** This may be due to the absorption of laser energy by means of electrons via, the inverse bremsstrahlung absorption process and more details of this observation are presented at the end of section 2.3.3.

2.6. Summary

To conclude, LIP emissions from some metal oxide targets are studied with corresponding metal targets of pure quality as reference. Line emissions from atomic and ionic species are employed for the characterization. The studies provide improved insight, throwing more light into LIP dynamics.

2.7. References

[1] Anna Rita Casavola, Gianpiero Colonna, Alessandro De Giacomo, Olga De Pascale, and Mario Capitelli, Applied Optics Vol 42 No.30 (2003)

[2] Z. Szymanski, J Phys D: Appl Phys. 30 3153 (1997)

[3] Giacomo De, Shakhatov V A, Pascale O De., Spectrochim Acta Part B 56 753 (2001)

[4] Ludvik Martinu, J Vac Sci Technol A 18 (6) 2619 (2000)

[5] S. S. Harilal, Applied Surface Science 172 103 (2001)

[6] J. Hermann, J Appl Phys. 83 (2) 691 (1998)

[7] J. Hermann, J Appl Phys. 73 (3) 1091 (1993)

[8] M Capitelli, Spectrochimica Acta Part B 59 271 (2004)

[9] Colonna G, Casavolla A, Capitelli M., Spectrochim Acta B 56 567 (2001)

[10] J. Hermann, A. L. Thomann, C. Boulmer-Leborgne, B. Dubreuil, M. L. De Giorgi, A. Perrone, A. Luches, and I. N. Mihailescu, J. Appl. Phys. 77 (7) 2928 (1995)

[11] Dann V. J., Manoj V Mathew, V P N Nampoori et al, Proceedings of Fifth National Laser Symposium, (Vellore Institute of Technology, Vellore, India, December 7-10, 2005)

[12] Hermann J., Boulmer-Leborgne C, Hong D., J Appl Phys., 83(2) 691 (1998)

[13] Restrepo E., Devia A., J Vac. Sc. Tech., A 22 (2) 377 (2004)

[14] Singh R. K., Holland O W, Narayan J., J Appl Phys 68 (1) 233 (1990)

[15] Giacomo A De., Spectrochim Acta PART B, 58 71 (2003)

[16] A. De Giacomo, V. A. Shakhatov, G. S. Senesi, S. Orlando, Spectrochim Acta PART B 56 1459 (2001)

[17] Leon J. Radziemski, Thomas R. Loree, David A. Cremers, and Nelson M. Hoffman, Anal. Chem. 55 1246 (1983)

[18] Boumans P W J M, Theory of Spectrochemical Exitation (London: Hilger and Watts, 1966) ch 6, p 149

[19] A. Perea, J. A. Chaos, J. Gonzalo and C. N. Afonso, Appl. Phys. Lett. 78 7 (2001)

[20] Harilal S S, O'Shay Beau, Tillack Mark S., J. Appl Phys 98 13306 (2005)

[21] Bekefi G., Principles of laser plasmas, (New York : Wiley, 1976)

[22] S. Amoruso, A. Amodeo, V. Berardi, R. Bruzzese, N. Spinelli, R. Velotta, Appl. Surf. Sci. 96 175 (1996)

[23] Harilal S S, Bindhu C V, Tillack M S, Najmabadi F and Gaeris A C, J. Appl. Phys. 93 2380 (2003)

[24] V. Margetic, A. Pakulev, A. Stockhaus, B. Bolshov, K. Niemax, R. Hergenroder, Spectrochim. Acta Part B 55 1771 (2000)

[25] http://www.nist.gov

[26] O. Barthelemy, J. Margot, M. Chaker, IEEE Trans. Plasma Sci. 33 476 (2005)

[27] Hans R. Griem, Plasma Spectroscopy, (Mc Graw-Hill Inc, United States of America, 1964)

[28] F. Vidal, T.W. Johnston, S. Laville, O. Barthelemy, M. Chaker, B. Le Drogoff, J. Margot, M. Sabsabi, Phys. Rev. Lett. 86 (12) 2573 (2001)

[29] F. Vidal, S. Laville, T.W. Johnston, O. Barthelemy, M. Chaker, B. Le Drogoff, J. Margot, M. Sabsabi, Spectrochim. Acta, Part B 56 (6) 973 (2001)

[30] S. Laville, F. Vidal, T.W. Johnston, O. Barthelemy, M. Chaker, B. Le Drogoff, J. Margot, M. Sabsabi, Phys. Rev. E 66 (6) 066415 (2002)

[31] S. Laville, F. Vidal, T.W. Johnston, M. Chaker, B. Le Drogoff, O. Barthe´lemy, J. Margot, M. Sabsabi, Phys. Plasmas 11 (5) 2182 (2004)

[32] J.P. Christiansen, D.E.T.F. Ashby, K.V. Roberts, Comput. Phys. Comm. 7 271 (1974)

[33] Torrisi L and margarine D, Plasma Sources Sci. Technol., 15 635 (2006)

[34] Harilal S. S., Issac R C, Bindhu C V, Nampoori V P N and Vallabhan C P G, J Appl. Phys. 81 3637 (1997)

[35] M. Sabsabi, P. Cielo, Appl. Spectrosc. 49 499 (1995)

[36] L. St-Onge, M. Sabsabi, P. Cielo, J. Anal. At. Spectrom. 12 997 (1997)

CHAPTER 3

Plasma diagnostics using probe signals derived from plasma source target

3.1. Introduction

The principal factors influencing the nature of interaction between laser radiation and solid target in vacuum are duration, wave length, power density of the laser pulse and laser light absorption processes as well as physical and chemical properties of the target. The dynamics of the plume produced in laser ablation processes is also of considerable interest in understanding the physics of plasma. Theoretical and experimental investigations are actively in progress in order to obtain accurate knowledge of all the physical processes involved in the ablation processes and the dynamics of laser induced plasma (LIP). Most of the above studies reported are carried out by using conventional Langmuir probes and typical investigation techniques of atomic and molecular physics, such as optical emission and absorption spectroscopy. This chapter deals with information on the LIP generation from metal targets by nanosecond laser metal ablation.

The processes involved in the initial stages of generating plasma from a solid target are complex. It is necessary to consider the heating of the target while in the solid state, the subsequent melting, vaporization and ionization. With high irradiances, ionization can occur very rapidly and since the energy required to ionize an atom is small compared to the energy needed to heat it to temperatures of some millions of degrees. Many theoretical calculations ignore the initial stages of plasma production from a solid target and a cold and fully ionized plasma is assumed to exist with ion and electron densities equal to the solid atom density [1].

The dynamics of plasmas formed from solid targets are governed by the geometry of the target, the laser beam and the time dependence of the laser pulse power and we find it convenient to consider planar targets for our experiment.

3.2. Initial stages of plasma formation from solid targets in vacuum

When laser pulse is incident on an opaque solid target, two extreme situations may be identified. Low irradiances produce only a rise in temperature below the surface, by conduction. If the irradiance is very large, multi-photon ionization takes place at the surface within a few cycles of the electric field and produces phase explosion. Between these extremes, there are a wide variety of intermediate situations governed by changes of phase, pressure due to vaporization, thermionic emission and shockwave generation. Along with this, various thermal, optical and mechanical properties of the target material and their temperature and pressure dependence will also control the interaction.

3.2.1. Light absorption and surface heating

Light (nanosecond duration) falling on the metal target is absorbed by electrons, which are thus raised to higher energy states. These electrons then transfer the energy by collisions with other electrons and phonons so that the solid tends to reach equilibrium at a higher temperature. In order that a single instantaneous temperature may be defined at every point, the light must not cause a substantial change in the internal energy of the region where absorption occurs during the relaxation times involved. The depth at which the temperature reaches a tenth of the surface value is only a few microns even at 50ns [2]. The rate of cooling is rapid, the surface temperature falling to a quarter of the maximum value in in 200ns. Such rapid changes in temperature are accompanied by sudden expansion processes which can generate shock waves in the target [3].

3.2.2. Effects of melting and vapourization

The next stage of heating in the target begins when the temperature is raised to the melting point. However, the transient liquid phase is not of great significance as far as the step towards the production of plasma is concerned. The latent heat of

fusion is small compared with the latent heat of vaporization or the ionization energy. Also, as the laser pulse is of short duration, the molten material will not be displaced significantly during the pulse. But with constant irradiance, the rate of heating increases considerably, together with surface melting. The most important consideration may be change in the optical characteristics of the surface [4].

When the boiling point is reached, effects that are more complex arise. At moderately high irradiances, the rate of evaporation will be greater and the resulting vapour density may become sufficiently large for the bulk of the incident flux to be absorbed in the region occupied by the vapour phase [5]. It should be remembered that the boiling point of a material is pressure-dependent. The radiation pressure due to a focused laser beam can exert a peak pressure of hundreds of atmospheres. When evaporation takes place, the departing particles exert even greater pressure on the surface due to the recoil [6, 7], which affect the physical and chemical properties of the target.

3.2.3. Thermal ionization

The temperature in the hottest region of the vapour generated by the laser pulse will rise as long as the local rate of absorption of energy from the beam is sufficiently large to overcome cooling by expansion and conduction. Eventually, the vapour may reach a sufficiently high temperature for a significant number of atoms to be ionized by collisions. If the vapour is still sufficiently dense, for thermodynamic equilibrium to hold, we may use Saha's equation to relate the densities n_e, n_i, n_a of electrons, ions and neutral atoms at a temperature T:

$$\frac{n_e n_i}{n_a} = \frac{2u_i}{u_a}\left(\frac{2\pi m_e k_B T}{h^2}\right) \exp\frac{-\chi}{k_B T} \qquad (3.1)$$

Here, u_i and u_a are the partition functions for the singly ionized and neutral atoms respectively and χ is the ionization energy of the neutral atom. In the early stages of ionization, only singly ionized atoms are present, so $n_e = n_i$.

At very low electron densities and high neutral atom densities in a lightly ionized vapor, electrons are more likely to absorb photons during free-free transitions, in collision with neutral atoms. The presence of even a small proportion of free electrons causes a marked increase in the absorption coefficient of the

gaseous phase and hence an increase in the rate of heating, leading to a greater degree of ionization. At this stage, free-free transitions of electrons in collision with positive ions become the dominant heating process and thereafter strong absorption occurs. Numerically, the rate of temperature rise is roughly equal to the irradiance [8]. As the temperature rises, the rate of heating increases initially. However as full ionization is approached, the power absorbed per particle begins to fall with increasing temperature and becomes density dependent. At higher densities, three-body recombination becomes the dominant recombination process [9]. In three body recombination, an electron is initially captured by an upper excited level. The electron then cascades down to the ground state either by radiative transitions or by transferring energy to free electrons through collisions.

As the laser fluence increases, the generated plume becomes hotter, resulting in the enhancement of the degree of ionization and thus absorb the incident radiation more efficiently.

3.2.4. Ionization through multi-photon processes

The very high particle densities occurring in solid and in vapour layers generated by intense light will cause strong stark broadening thereby favoring quasi-resonant processes as well as depressing the ionization energy [10]. At very high irradiances, tunneling theory shows that ionization can be extremely rapid and occurs within one or two cycles of electric field. The stimulated Raman effect produced by laser light in a dense medium can produce anti-stokes photons of high frequency [11]. If higher order photons are produced, direct single photon ionization may occur.

3.3. Scope of the work

Target materials get electronically charged, when photo-ablated with an energetically suitable laser pulse. An electrical signal that can be delivered from the target can be used as an alternative probe signal for the diagnostics of LIP.

The ejected species going in to the expanding plume of LIP is responsible for target charging. Laser irradiation in vacuum thus leads to fast rising voltage transients on the target. This may provide information on the nature of ablated species, their expansion velocities and the extent of ionization in the plume. Real

time detection of both electron and ion currents is also possible [12]. Plasma generation and plume evolution processes get reflected on the temporal variations of the time of flight (TOF) spectrum.

The present study deals with the diagnostic aspects of LIP using the signals generated at a copper target. The effects of bias voltage, laser fluence and vacuum level on the plasma dynamics are collected through the signal variations derived from plasma source target.

3.4 Expansion dynamics of laser induced plasma (LIP) in field free space

3.4.1. Experimental works in detail

The plasma is created inside an evacuated chamber (2x10-5 mbar) made of steel. An Nd:YAG laser (Spectra Physics, DCR 11, 10 ns) operating at 10Hz in its fundamental wavelength (1064nm) is used as the laser source for plasma production. A copper disc of 2mm thickness and 20 mm diameter is the target for the focused laser beam. The irradiance is kept at 2.6GW cm^{-2}.

The characterization part involves an active probing technique in the sense that we are not inserting any additional probe into the plasma. It is possible to investigate the history of plasma evolved from the target by looking into the electrical

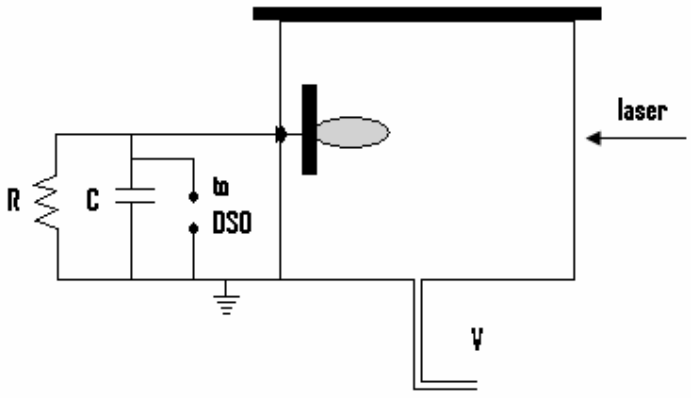

Fig.3.1: Experimental setup to study target signal. V - vacuum pump; R – resistance; C – capacitance; DSO – digital storage oscilloscope.

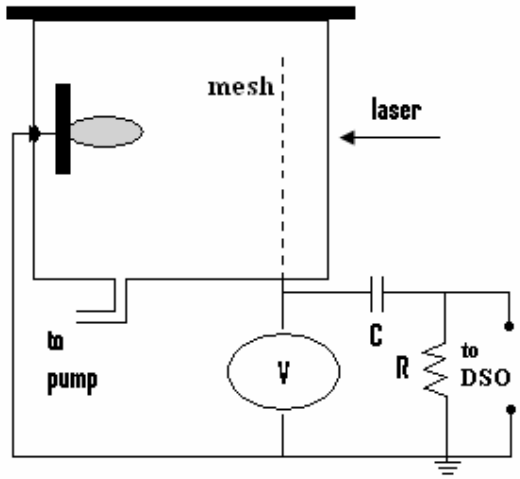

Fig.3.2: Experimental set-up for TOF studies. V- applied bias; C – capacitance; R – resistance; DSO – digital storage oscilloscope.

signal generated at the target itself. The electrical lead taken from the target, for this purpose, is well insulated from the metal chamber. The effects of external parameters on the laser driven plasma can be identified by the temporal variation of voltage transients generated at the target [13]. A schematic diagram of the experimental setup is shown in Fig.3.1. The resistance ($k\Omega$) and capacitance (pF) values are adjusted for the best signal strength.

A TOF spectrum has been recorded with the help of a properly biased mesh, having freedom of translation along the plume expansion direction, erected adjacent to the target. The corresponding experimental setup is given in Fig.3.2. The signal recorded under this arrangement is used for probing the effects of bias voltages, laser fluences and vacuum levels on the plasma dynamics.

3.4.2. Discussion of results

The forward-directed nature of the laser evaporation from planar targets is due to the anisotropic expansion velocities of different species in the plume, imposed by the boundary conditions [14]. The plasma expands freely in vacuum with elliptic contours along the expansion direction which is the target normal.

This is due to the initial density gradient and pressure within the plume, which are much larger in the direction perpendicular to the target surface than in the lateral directions [15]. As the laser pulse triggers the plasma, the peak signal voltage is reached within 80ns.

The transient target charging can be postulated to arise through those electrons which have sufficiently high energies to overcome the plasma work function U and the potential V_T (induced by laser irradiation), escaping from the expanding plasma to the grounded chamber. For a Maxwellian electron energy distribution, it can be shown that the electron current is given by [16, 17]:

$$i_T = i_0 \exp - \left[e(U + V_T) \Big/ kT_e \right] \tag{3.2}$$

where, T_e is the electron temperature and i_0 is a constant. The signal then falls rapidly but sustain for several microseconds. During this time, the behaviour is strongly dependent on the target conditions and the complex processes taking place on the surface layers as well as in the generated plume.

The different peaks superposed on this unipolar pulse correspond to the generation and propagation of species which are at different charged states. Heavier ones take longer times to reach the chamber wall and are delayed more. Fig.3.3 shows the external bias free signal delivered from the target, when irradiated with 200mJ laser energy. This gives an irradiance level, which is well above the plasma generation threshold for copper.

The TOF spectrum of the most prominent species in the plasma has been captured by applying positive and negative polarities to the mesh, arranged adjacent to the target. In both the cases, the ablation produces a bipolar voltage waveform. Calibration of the time-of-flight scale is made by varying the distance between the target and the mesh. The time delay associated with the signal peak can be used to see how their velocities are modified during the transit. A typical TOF profile is given in Fig.3.4.

The ions are accelerated towards the biased mesh and the signal shows a modified time of flight even when the voltage levels are varied. Fig.3.5 shows the

delay in the signal peak when the negatively biased mesh is translated away from the target.

On reversing the polarity (with positive polarity), the electrons are collected by the mesh and an associated negative potential is detected. But it is to be noticed that the voltage waveform is bipolar in nature. During the first 500ns, during which the plasma is highly dynamic, the signal is positive. Thereafter, the signal swings to the negative with a clear twin projection. This can be seen from Fig.3.6. The peak height of the voltage signal is high even when the mesh is negatively biased. In addition to the positive ions collected at the mesh, the secondary electrons generated by neutrals (at the mesh) also may be contributing to this positive voltage.

The velocity distribution of the peak maxima is as shown in Fig.3.7. The appearance of twin peaks is supporting the presence of secondary electrons at the collector.

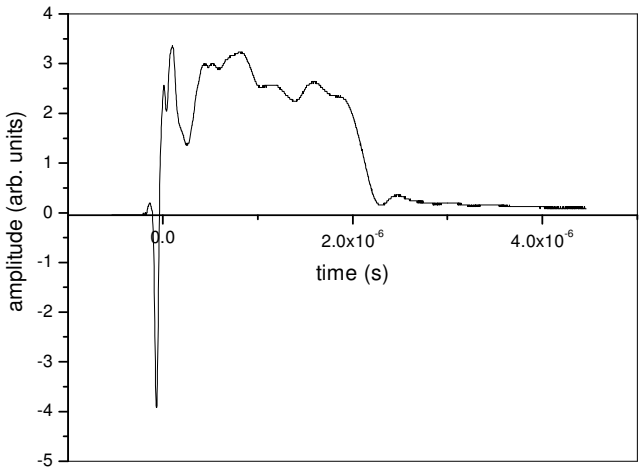

Fig.3.3: Target signal without bias

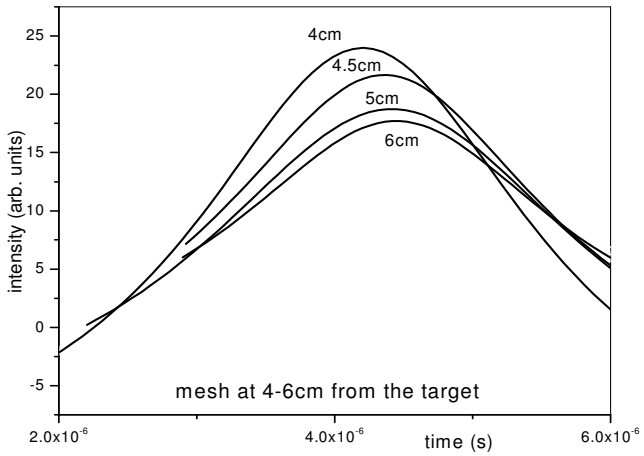

Fig.3.4: A TOF profile of the signal under study, with metallic mesh at various distances from the target.

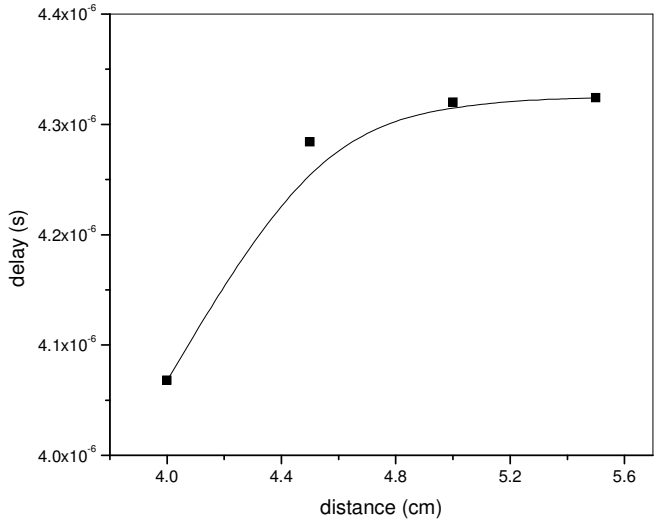

Fig.3.5: Delay in signal peak measured at the negatively biased mesh

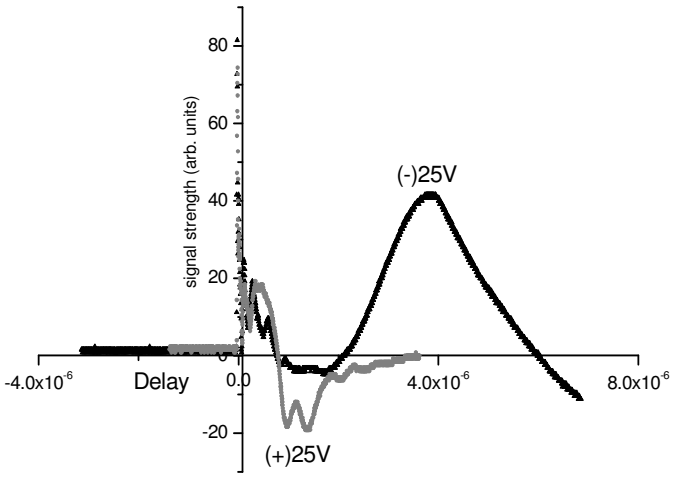

Fig.3.6: Signals with positive and negative bias

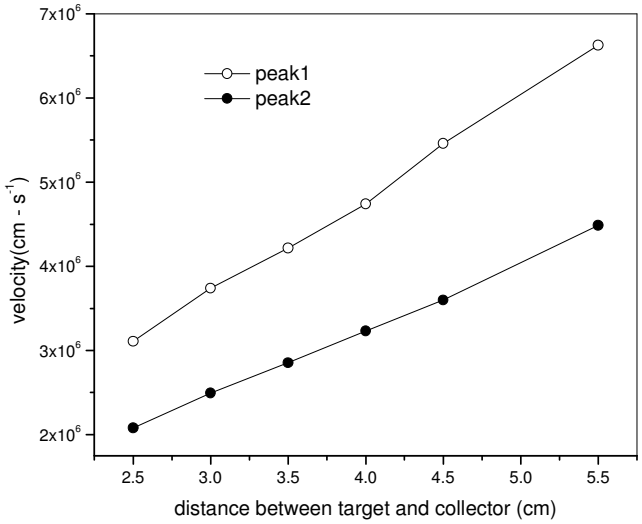

Fig.3.7: Variation of peak velocities with positive bias

The effects of vacuum and power levels on the proposed signal can be seen in Figs.3.8 and 3.9.

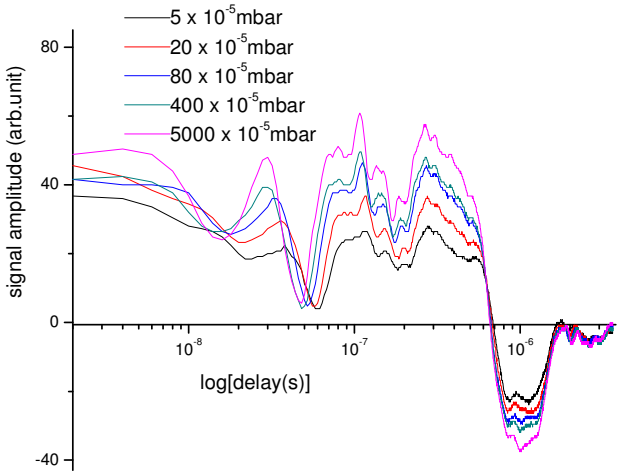

Fig.3.8: signal response to chamber vacuum

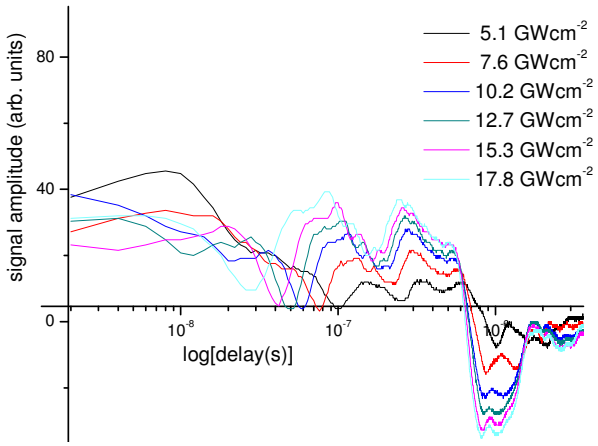

Fig.3.9: Signal response to laser irradiance variation

The responses are collected after applying a fixed moderate positive voltage on the mesh. The chamber pressure is varied from $5x10^{-2}$ mbar to $5x10^{-5}$ mbar of ambient nitrogen. The signal amplitude decreases with increase in vacuum level and as the ambient pressure is decreased, the multiple structure of the profile is clear. This is

probably due to the different species present in the plume gaining more energy in vacuum with an enhancement of secondary electron production. The increase in prominent charge states through collisions with ambient molecules also may be responsible for this effect.

For a given pressure and mesh bias, the signal amplitude and its multiple structure varies also with laser irradiance. Thus, signal response with increase in laser energy shows some analogy with that due to the increase of pressure. The maximum of the distribution is gradually shifted to the left as the energy in increased. This shows the gain in energy of the particles in the distribution.

3.4.3. Summary

Different charged states of the same atom can be tracked from the signal [18]. The signal shows a double peak distribution with positive polarity and a modified time of flight when the voltage levels are varied. As the ambient pressure is decreased, the multiple structure of the peak becomes clear. It seems that the method, when implemented together with suitably designed Langmuir probes can throw more light on the hidden aspects of this technique.

3.5. Effect of external magnetic field on the probe signals

Effects of parameters like external magnetic field on LIP can also be studied by the response of the corresponding electrical signal from the plasma source target.

3.5.1. Introduction

The use of a magnetic field with laser-created plasma is especially interesting, as the magnetic field can be used to control the properties of the transient and dynamic plasma state. The collimation and stability properties of plasma flow across a magnetic field are of particular relevance to the propagation of charged particle beams, stellar bipolar flows, solar wind evolution etc. In inertial fusion, confinement of expanding plasma using a magnetic field offers a potential means to slow high energy particles before they implant in surrounding structures [19, 20]. Spectroscopic studies of dynamics of the plume species in the presence of a magnetic field showed that their spatial and temporal characteristics change considerably with their charge state.

The presence of a magnetic field during the expansion of laser produced plasma may initiate several interesting physical phenomena including conversion of plasma thermal energy into kinetic energy, plume confinement, ion acceleration, emission enhancement, plasma instabilities etc. [21]. It has been postulated that a cloud of laser produced plasma will be stopped by a magnetic field B within a distance $R \sim B^{-2/3}$. Apart from its basic research importance, the effect of a

magnetic field on the expansion dynamics of LIP plumes also has importance in applied research. The effectiveness of debris reduction using magnetically guided pulsed laser deposition has been demonstrated by previous workers [22, 23].

3.5.2. Experiment and results

The effects of external magnetic field on the laser driven plasma can be identified by the temporal variation of voltage transients generated at the target. A schematic diagram of the experimental setup is shown in figure 3.10. The circuit is closed by the emitted charged species travelling towards the chamber wall at velocities greater than $2x10^6$ cm/s [13, 18]. As the laser pulse triggers the plasma, the signal rises to positive within 5ns. This is due to the creation of plasma on the target surface and is unaffected by the application of external magnetic field. This signal showing some characteristic variations as the plume expands is always positive until it finally drops to zero, after two microseconds.

Magnetic field is applied on LIP in a direction transverse to plasma expansion. Two disc shaped magnetic pole pieces (4cm diameter) are used to apply a magnetic field of maximum flux density 0.2T. The magnets placed inside suitable non-magnetic housings are given required separations to change the field in-between. The target is carefully aligned outside the field so that the generated plume expands into the field. Absolute calibration of the field strength has not been performed. For qualitative analysis, the separation between the pole pieces is varied. The results of field mapping have shown that the field is inhomogeneous when the pole pieces are closer (< 4.5 cm). As the pole pieces are separated, the field becomes more and more homogeneous (7.5cm > separation between the poles > 4.5cm). Thereafter, an inhomogeneous decrease in field strength is observed (separation between the poles > 7.5cm) and at each instance, the plasma responds to the field variations as observed in Fig.3.11.

On applying the magnetic field, the trajectories of different charged particles in the plasma and their kinetic energies are modified and they enter into newly defined territories. The plasma confinement (though small) induced by the field should increase the collision frequency of the charged species by confining them to smaller volumes. The plume front decelerates in the direction normal to the target surface and the ion density in the plasma rises immediately. At this point of time, the possible recombinations and their rates get modified and the target experiences a deficiency of positive charge which pulls the signal negative. At later times, the plume tries to

expand in the direction of the magnetic field and the signal grows more and more positive. It is noted that, the transition to positive signal is delayed in intense fields.

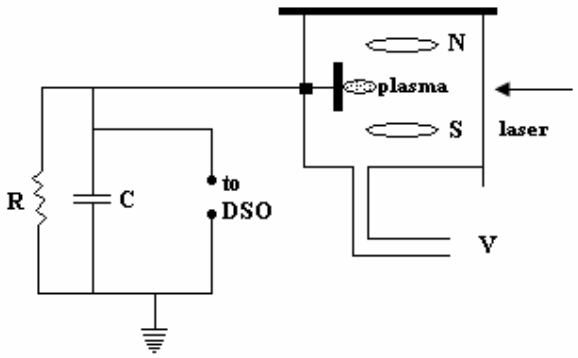

Fig.3.10: schematic diagram of the experimental set-up. [N-North pole, S-South pole, V-vacuum pump, R–resistance, C-capacitance and DSO-digital storage oscilloscope.

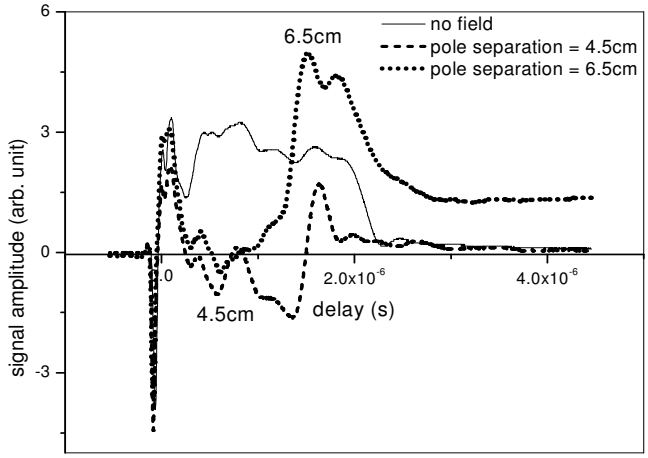

Fig.3.11: Effect of magnetic field on the signal. Two different field strengths are applied. [Absolute calibration of the field strength has not been performed. For qualitative analysis, the separation between the pole pieces are varied.]

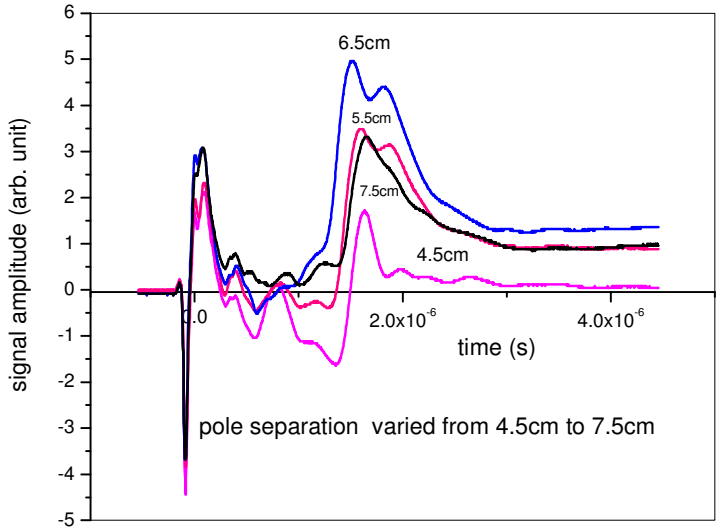

Fig.3.12: Signals showing the effects of magnetic field on the dynamics of plasma. [Absolute calibration of the field strength has not been performed. For qualitative analysis, the separation between the pole pieces are varied.]

Figure 3.12 shows the signal extracted from the target when the magnetic field intensity is systematically varied. The strong signals around 1.5μs and 1.85μs are especially noticeable. Both are delayed in a homogeneous field. In the no field case, the signal falls to zero at 2.3μs after the laser pulse. In the presence of field, the signal exists for longer time. This shows that the plume lifetime is increased in the presence of magnetic field.

3.5.3. Summary

The plasma expansion dynamics in magnetic field has been investigated by monitoring the voltage transients generated at the target. The signal in the presence and absence of magnetic field is analyzed to investigate on the plasma responses to the field. The field confines the plasma and the charged particles enter into new territories, with modified trajectories and kinetics. Signs of a transverse expansion are evident. An increased plume lifetime is observed in the presence of the field.

3.6. References

[1] T. P. Hughes, Plasmas and laser light (Adam Hilger, London, 1975)

[2] Ready J. F., J. Appl. Phys. 36 462 (1965)

[3] Steverding B., J Phys D 3 358 (1970)

[4] Bonch Bruevich, A M Imas Ya A, Romanov G S, Libenson M N, Maltsev L N, Sov. Phys. Tech. Phys. 13 640 (1968)

[5] Anisimov S. I., Bonch-Bruevich A M, El Yashevich M A, Imas Ya A, Pavlenko N A, Romanov G. S., Sov. Phys. Tech. Phys. 11 945 (1967)

[6] Askaryan G. A. and Moroz E M, Sov. Phys JETP 16 1638 (1962)

[7] Hughes T P, Proceedings of conference on lasers and their applications, (sponsored by IEEE and Science divisions, London), pp. 5-12 (1964)

[8] Archbold E., Harper D W, Hughes T P, J Appl Phys 15 1321 (1964)

[9] Martineau J and Tonon G, Phys Lett. 30A, 32 (1969)

[10] Farkas Gy. Horvath Z. Gy., Kertesz I, Phys Lett 39A 231 (1972)

[11] Mennincke H, Phys Lett 37A 381 (1971)

[12] S. H. Brongersma, J. C. S. Kools, T. S. Baller, H. C. W. Beijerinck and J. Dieleman, Appl. Phys. Lett. Vol. 59 No.11 1311 (1991)

[13] P. E. Dyer, Appl. Phys. Lett. Vol 55, No.16 1630 (1989)

[14] Rajiv K. Singh and J. Narayan, Phys. Rev. B 41 8843 (1990)

[15] S. S. Harilal, M. S. Tillack, B. O'Shay, C. V. Bindhu and F. Najmabadi, Phys. Rev E, Vol 69 26413 (2004)

[16] Robert F. Benjamin, Gene H. McCall and A. Wayne Ehler, Phys. Rev. Lett. 42 890 (1979)

[17] G. Cook and P E Dyer, J. Phys. D 16 889 (1983)

[18] R. J. Von Gutfeld and R W Dreyfus, Appl. Phys. Lett. 54 (13) 1212 (1989)

[19] W. Gekelman, M. Van Zeeland, S. Vincena and P. Pribyl, J. Geophys. Res.[Space Phys.] Vol 108 1281(2003)

[20] H. C. Pant, Phys. Scr. Vol T 50 109 (1994)

[21] D. K. Bhadra, Phys. Fluids Vol 11 234 (1968)

[22] R. Jordan, D. Cole and J. G. Lunney, Appl. Surf. Sci. Vol 110 403(1997)

[23] Y. Y. Tsui, H. Minami, D. Vick and R. Fedosejevs, J. Vac. Sci. Technol. Vol A 20 744 (2002)

CHAPTER 4

Optical emissions from laser induced breakdown in external magnetic field

4.1. Introduction

The presence of a magnetic field during the expansion of laser induced plasma (LIP) may initiate several interesting phenomena, including conversion of plasma kinetic energy into thermal energy, emission enhancement, plasma instabilities and oscillations in the temporal history of emitting species. Plasma has a natural tendency to disperse, as the energetic particles that compose the plasma travel away from their initial positions at high velocity and the system of plasma will cease to exist. Plasma particles can be prevented from dispersion, with the aid of a magnetic field which acts on charged particles through Lorentz force. Magnetic fields can confine plasma, because the ions and electrons of which it consists will follow helical paths around the magnetic field lines. The dynamics of charged particles in magnetic field therefore forms an important area of investigation in the field of plasma physics.

A charged particle placed in a magnetic field will execute a circular orbit in the plane perpendicular to the direction of the field. We can also add an arbitrary drift along the direction of the magnetic field due to the Lorentz force $(q \cdot \mathrm{v} \times \mathrm{B})$ acting on the particle which depends only on the velocity component perpendicular to the magnetic field. The combination of these two motions gives a spiral trajectory to charged particle in magnetic field, with the field as the axis of the spiral. Thus, the freedom of motion in the perpendicular direction is thereby substantially suppressed by the field. If we pass to the limit of an extremely strong magnetic field, then the plasma behaves as if it were a one dimensional gas. These features are normally reflected in the properties of the collective modes in the plasma dynamics. The propagation characteristics of the electron plasma oscillation and the ion-acoustic wave are greatly altered by the magnetic field. Another notable feature is the periodicity brought about by the cyclotron motion of the particles. Plasma may thus exhibit new collective modes, propagating mainly in

directions perpendicular to the magnetic field, with a frequency near the fundamental or a higher harmonic frequency of the cyclotron motion [1].

The plasma plume will try to exclude the magnetic field as it expands. The magnetic gradient will then exert a backpressure against the expansion. The expansion will stop when the plasma energy is expended in doing work to oppose the magnetic gradient backpressure. The field may produce cross-field diffusion due to collision or parametric instabilities in the plasma.

In recent years, the use of a magnetic field to confine laser-induced plasmas has attracted more and more interest due to the strong coupling between magnetic field and the LIP.

4.2. Effect of magnetic field on laser induced plasma

The first set of experiments on the effects of magnetic fields on laser produced plasmas were made by Linlor et al [2,3]. He showed that the magnetic field was being displaced by the expanding conducting plasma. In 1969, Mattioli and Veron [4] observed that the intensity of recombination radiation was strongly reduced by the field. Haught et al [5] found that the stopping time of plasma in a magnetic field varies as $B^{-2/3}$. According to Tuckfield and Schwirzke [6], the field had very little effect on the early stages of development of plasma because, the kinetic pressure of the plasma then greatly exceeded the magnetic pressure. Sucov et al [7] studied LIP produced from aluminium targets in a transverse field. He observed narrowing of the plume and a five times increase in the duration of the luminosity of central core. There was a tendency for the plasma to break up in the field. The boundary moved across the magnetic field lines towards the laser almost as rapidly as it did with no field and this was the result of charge separation creating an electric field which cancelled out the v x *B* force.

In the following sections, we discuss the studies made on temporal emission profile of Lithium plasma in magnetic field.

4.3. Dynamics of LIP in magnetic field

When an external magnetic field is applied to LIP, the electrons and ions in the plasma are under the influence of Lorentz force, and the expansion and diffusion of the plasma are decelerated. From magnetohydrodynamic (MHD) equations, the parameter β of the plasma is given by

$$\beta = \frac{8\pi\ nkT_e}{B^2} = \frac{particle\ \ pressure}{magnetic\ \ field\ \ pressure} \qquad (4.1)$$

This indicates the size of the diamagnetic effect [8] and is also called thermal β of the plasma. The deceleration of the plasma expansion under the influence of a magnetic field is given as [9],

$$\frac{v_2}{v_1} = \left(1 - \frac{1}{\beta}\right)^{1/2} \tag{4.2}$$

where, v_1 and v_2 respectively are the asymptotic plasma expansion velocity in the absence and presence of the magnetic field. When β=1, the plasma would be stopped by the magnetic field. In the case of high β, the magnetic confinement would not be obvious while in the case of low β plasma, the magnetic confinement would be effective. Considering an increase in plasma density under magnetic confinement, Rai et al derived a simple expression giving the ratio of plasma emission in the presence (I_2) as well as in the absence (I_1) of a magnetic field [9]:

$$\frac{I_2}{I_1} = \left(1 - \frac{1}{\beta}\right)^{-3/2} \left(\frac{t_1}{t_2}\right) \tag{4.3}$$

where, t_1 and t_2 are the emission times of plasma in the absence and presence of a magnetic field. This can explain the emission enhancement observed in some cases of plasma with β values close to 1. At the same time, even with β values close to 1, it is observed that the plume is not completely stopped by the field. This means that β is not the only factor governing the nature of expansion.

After the initial conversion of thermal energy into the directed energy, the directed beta (β_d), given by,

$$\beta_d = \frac{4\pi\ n_e m v^2}{B^2} \tag{4.4}$$

becomes an important parameter. During the early phase of the plume expansion, β_d is of the order of a few thousands which indicates that the plasma is in the regime of diamagnetic expansion [10]. The diamagnetic cavity (also called magnetic bubble) expands until the total excluded magnetic energy becomes comparable to the total plasma energy. By assuming that the plume expands spherically and considering that it is expanding from a flat surface into solid angle 2π, the confinement radius (R_b) can be written as,

$$R_b = \left(\frac{3\mu_0 E_l}{\pi B^2}\right)^{1/3} \tag{4.5}$$

where E_l is the total plasma energy and B is the applied magnetic field [11, 12].

It is found that β_d varies by nearly three orders of magnitude during the plume expansion across the magnetic field. At earlier times, the charged particles diffuse through the

region occupied by the magnetic field and exclude the field. The diffusion coefficient of the charged particles perpendicular to a field is related to the field strength by [13],

$$D \propto \frac{1}{\beta^2 T^{1/2}} \tag{4.6}$$

So, an increase in temperature will reduce the diffusion across the magnetic field and eventually the plume will slow down considerably. At later times of plume evolution, the plasma cools and the magnetic field is able to diffuse across the boundary relatively fast. In this regime, β_d approaches unity, indicating that the displaced magnetic field energy is approximately equal to the kinetic energy of the expanding plasma. The energy of the magnetic field is converted to heat within a characteristic magnetic diffusion time (t_d) given by,

$$t_d = \frac{4\pi\sigma R_b^{\,2}}{c^2} \tag{4.7}$$

where, σ is the plasma conductivity which can be obtained with Spitzer formula [14].

4.4. Experimental setup

Lithium plasma is produced inside a multipurpose stainless steel chamber evacuated to a base pressure better than 10^{-5} mbar. The target used is pure solid lithium rod of 1.2 cm diameter and 5 cm length. A Q switched Nd: YAG laser with a repetition rate of 30 Hz and 8 ns FWHM is used to generate the plasma. The irradiance at the target is set to be about 2.23 GWcm^{-2}. A PMT with 2 ns rise time, mounted on the exit side of the monochromator has been used to record the signal. The output from the PMT is directly fed to a 500MHz digital oscilloscope (Tektronix, TDS 540). A pulsed transverse magnetic field is generated by discharging a high voltage capacitor bank through a pair of coaxial coils in Helmholtz configuration. During discharge, a high current flows through the coil and hence an induced magnetic field is obtained. The peak point of the magnetic pulse having $\cong$ 2ms life time is synchronized to the nanosecond laser pulse with the help of a programmed microcontroller.

A schematic diagram of the experimental setup is shown in figure 4.1. The diode lasers are helpful in the alignment of Nd:YAG beam on the target surface as well as in the proper imaging of different spatial slices of plasma on the spectrometer slit.. The

detailed description of the different components of the Helmholtz coil and capacitor bank circuit are given in the following sections:

4.4.1. Helmholtz coil

A Helmholtz coil is a pair of conducting circular coils each having *N* turns, carrying a current *I*, separated by a distance comparable to the radius of the circular loops. The arrangement produces a homogeneous magnetic field *B*, in the mid-plane between the two circular coils. The pair of inductor coils are made from copper wire of high current limit, wound on a perspex spool, each coil having 22 number of turns. The diameter of the coil is 0.5m and the distance between the pair of coils is 0.46m. Each of the coils is symmetrically fixed on either sides of the stainless steel vacuum chamber, in such a way that uniformity of the field is maintained at the center of the chamber. The axis of the coil and the plume expansion axis are mutually perpendicular. Both the coils are connected in parallel to the discharging circuit of the capacitor bank.

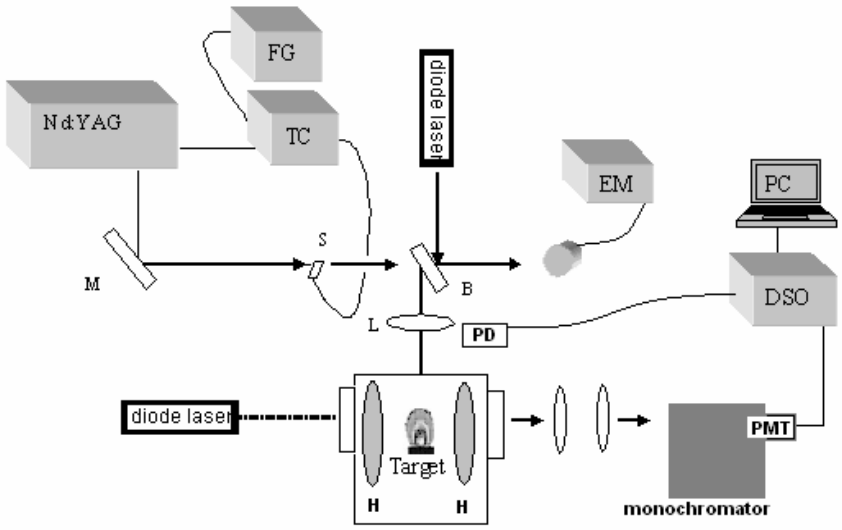

Fig 4.1: Experimental setup used for the generation of plasma and optical spectroscopic studies. (FG- function generator, TC-timing controller, S-shutter, EM-energy meter, PD-photodiode, DSO-digital storage oscilloscope, PMT-photo multiplier tube, M-mirror, B-beam splitter, L-focusing lens, H-helmholtz coil).

The magnetic field intensity at the center of the coil is calculated by the formula,

$$B = \frac{\mu_0 IR^2}{2(R^2 + x^2)^{3/2}} \tag{4.8}$$

where, $\mu_0 = 1.26 \times 10^{-6}$ Hm^{-1}, I is the current in amperes, R is the coil radius in metre, x is the distance between the centre of the chamber and each of the coil.

Since each coil consists of N number of turns, NI gives the total current in the coil.

so that, $$B = \frac{\mu_0 NIR^2}{2(R^2 + x^2)^{3/2}} \tag{4.9}$$

Since there are two such coils, we write,

$$B = \frac{\mu_0 NIR^2}{(R^2 + x^2)^{3/2}} \tag{4.10}$$

At $x = 0.23$ m,

$$B = 0.435 \times I \text{ (Gauss)} \tag{4.11}$$

Fig.4.2 shows the calibration curve for the field at the coil centre.

4.4.2. Rectifier circuit

The rectifier circuit shown in Fig 4.3 consists of a series-parallel combination of 19 numbers of 1 pF capacitors, IN-5408 diodes and 1 MΩ resistances. The circuit converts the ac input from a step-up transformer having a 1:20 turns ratio into a dc voltage, which is then used to charge the high voltage capacitor-bank up to the desired voltage. This voltage is then discharged using an ignitron switch to produce the pulsed magnetic field.

4.4.3. Capacitor bank

The rectifier circuit is connected to a 700μF/5kV high voltage capacitor through a 100 kΩ series resistance. The capacitor is connected to an ignitron switch, through the helmholtz coils. During the charging time of this high voltage capacitor, the ignitron switch is kept in an open state and the capacitor is thus disconnected from ground. At the discharging time, the ignitron switch is closed by giving a TTL trigger pulse and the capacitor discharges through the coil to the ground. The discharge of the capacitor will cause a high current flow through the coil and a pulsed magnetic field is produced around

the coil. The minimum charging time of the capacitor is 70 sec. Figures 4.4 and 4.5 show the capacitor-bank circuit and its firing circuit.

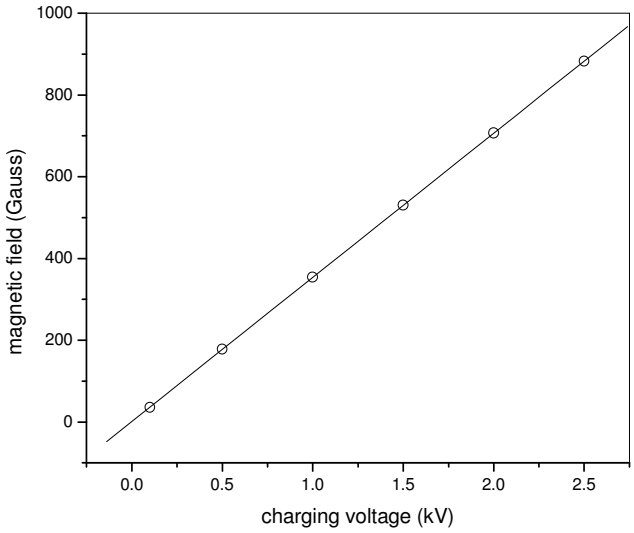

Fig 4.2: The variation of magnetic field strength with capacitor voltage.

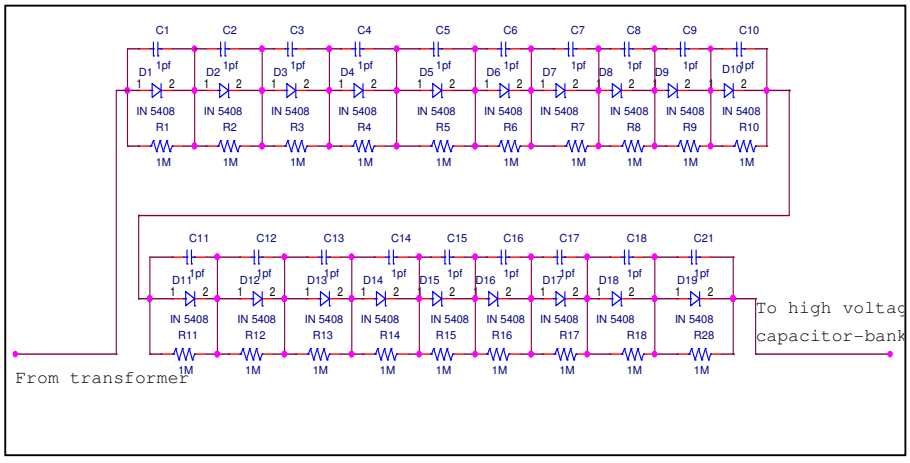

Fig 4.3: The rectifier circuit.

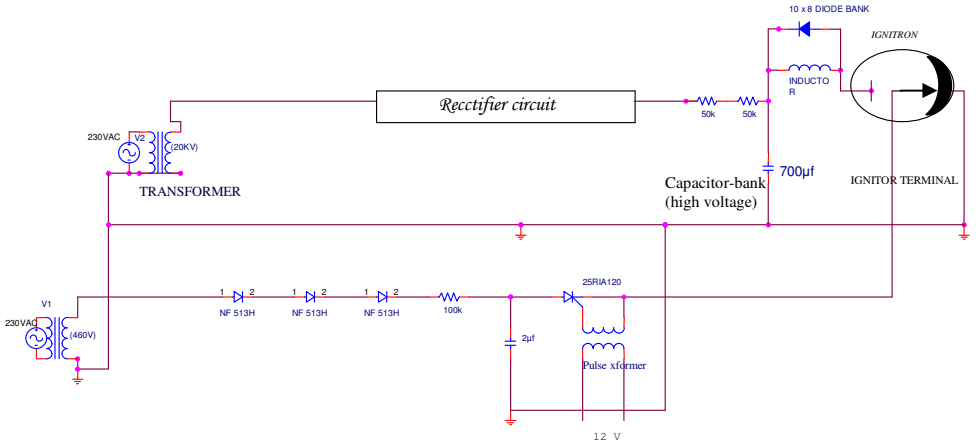

Fig 4.4: The high voltage capacitor-bank circuit used for producing magnetic field.

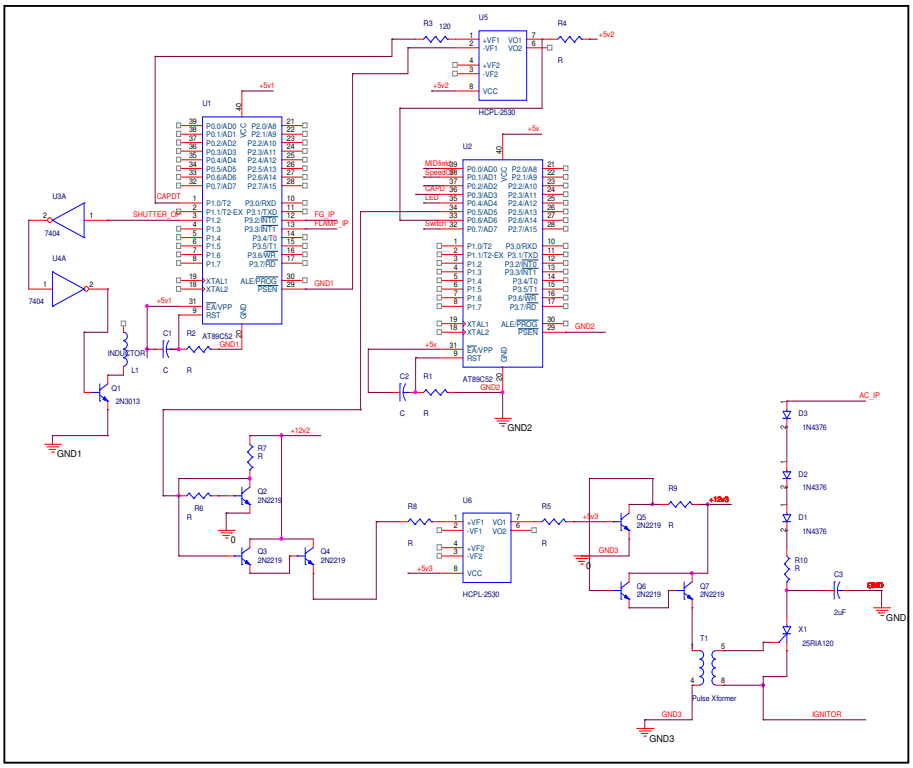

Fig 4.5: firing circuit for the high voltage capacitor-bank

4.4.4. Ignitron

The ignitron can be considered as a switch with an ingenious closing device of unusual reliability and almost indestructible electrodes. Without any applied voltage on the ignitor, the device is an open switch capable of reliably withstanding high voltages without conduction of current.

When a forward voltage is applied between the ignitron and the mercury-pool cathode, the resistance between the two elements decreases suddenly to a few ohms as a hot spot forms on the interface between the mercury surface and the ignitor. Mercury vapour is generated and a mercury glow discharge forms between the ignitor and the spot. This discharge is sustained by the electrical energy from the ignitor voltage source. While this condition exists, the presence of a forward voltage in excess of approximately 15 volts from anode to cathode will cause ionized mercury vapor to fill the tube and allow conduction to occur, making the ignitron a perfect closed switch. During conduction, the mercury pool cathode provides an almost unlimited supply of electrons making it an ideal switch for controlled capacitor discharges.

The change from nonconducting to conducting state of the ignitron is initiated by the ignitor excitation circuit. The ignitron requires a high voltage, which is provided by a Thyristor (25RIA-120).

4.4.5. Level converter circuit

The level converter circuit converts the small voltage (~12V) given by the transistor to about 315 V. This is supplied by a transformer and after rectification, this is transferred to the ignitor terminal to fire the capacitor-bank circuit. The level converter circuit consists of a series combination of three diodes (NF-513H) and a resistor (100 kΩ).

4.4.6. Micro-controller

A microcontroller (8051 architecture, chip no: 89C52) has been used to synchronize trigger pulses both from the flashlamp and the function generator so that maximum magnetic field can be obtained at the time of laser pulse. When the function generator trigger pulse and the flashlamp trigger pulse are given as inputs to the microcontroller it produces output triggers for the mechanical shutter and

also for the capacitor bank circuit. The shutter will open to receive one Q-switched laser pulse and closes just after the laser pulse. If delay adjustment is required for the capacitor bank circuit (for the synchronization of the laser pulse with the magnetic field pulse), then a second micro-controller can be programmed to produce the required delay for the output trigger from the first micro-controller.

4.4.7. Optocoupler

An optocoupler can be used to protect the system from the overvoltage damage, when the source and destination are at very different voltage levels. An optocoupler consists of an LED as a source of light and a phototransistor as the receiver. It transfers light signals from the LED to the phototransistor. This helps to transfer data between the circuit components, avoiding electrical contact between them.

4.4.8. Working

During manual triggering, a 50 MHz function generator provides a TTL trigger pulse to the synchronizing circuit. After synchronization, a 12 V TTL trigger will come to level converter circuit which then gets converted to 315 V and finally reaches the ignitor terminal. This closes the ignitron switch, which leads to the passage of current through the inductor coils in Helmholtz configuration and the desired pulsed magnetic field is generated around the coil.

4.4.9. Laser synchronization

When the flash lamp is triggered it will produce the laser output and simultaneously the capacitor bank circuit will be triggered to generate the magnetic field pulse. The pulse width and maximum amplitude of the magnetic field will be different from that of the laser pulse and they also differ in time. To fire the laser at the maximum field point, a microcontroller is programmed to produce a trigger pulse from the AND logic output of the flash lamp trigger pulse and the function generator trigger pulse so as to produce the required delay for both the shutter and the capacitor bank circuit. The trigger pulses for the laser and shutter operations are gated in such a way that the shutter is opened just before the laser pulse. The mechanical shutter opens only for one Q-switched laser pulse. Fig.4.6 shows the timing diagram for laser-synchronization.

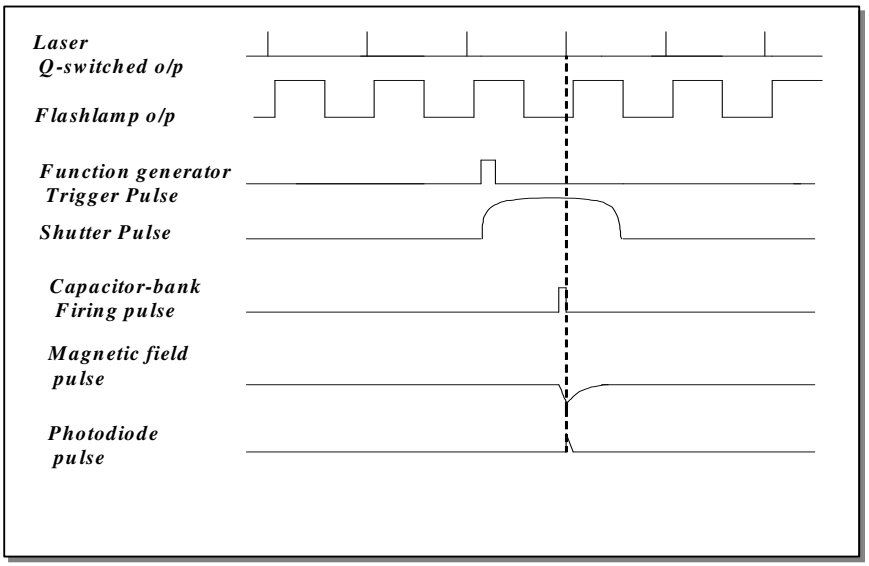

Fig 4.6: Timing diagram showing the laser synchronization.

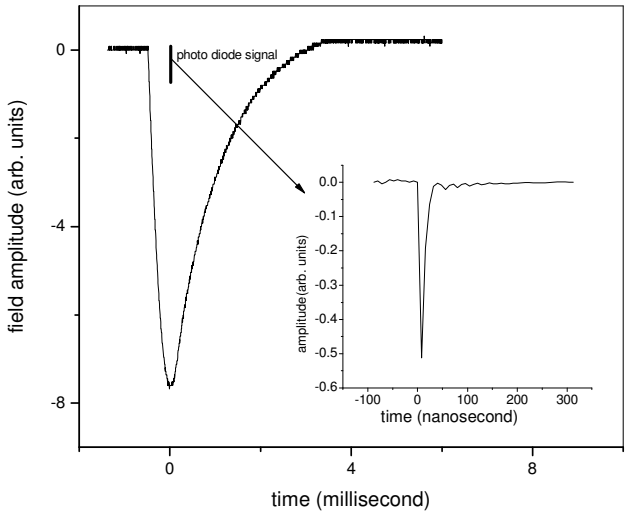

Fig 4.7: The magnetic field (ms) synchronized with the photodiode signal. A profile of the photodiode signal (ns) is given in the inset.

The magnetic pulse (millisecond range) and the photodiode signal (nanosecond range) are synchronized as shown in Fig.4.7 such that the photodiode signal comes at the maximum field point.

4.5. Discussion of results

Emission spectrum from the plasma is recorded using a the experimental setup of figure 4.1. Two neutral (6708Å from a ^2S - $^2P^0$ transition and 6103Å which is a $^2P^0$- 2D transition) lines and two ionic (4788Å from $^1P^0_1$ – $^1D_2$ transition and 5484Å which is a ^3S – $^3P^0$ transition) lines of Lithium are selected for the experiment and the field strengths has been varied between 100G and 800G. The plasma is allowed to expand in vacuum and in argon environment. The front region of the expanding plasma is not much affected by the applied field. Temporal profile investigations are therefore done on the slice of the plasma at 6 mm from the target surface.

4.5.1. Effect of magnetic field on intensity and time delay of plasma emissions in vacuum

In general, the line profiles of both the neutrals and ionic species show a gradual reduction of intensity with applied field (Fig.4.8 and Fig.4.9). The plasma density at 6mm is such that, the applied field is strong enough to penetrate the plasma. As seen in the figures, the intensity decrease with applied field is linear at 6mm.

As the particles in the expanding plasma propagate perpendicular to the applied magnetic field and when the field and plasma pressures are comparable, progressive development of a sharp boundary between the field and the plasma is possible. The expansion velocity of the plume normal to the target decreases and this reduces the forward spatial range of the particles. The slowing down of neutrals and ions in the presence of the field is consistent with an MHD model in which the kinetic energy of the expansion is transformed into random electron motion [15]. Simultaneously, the plasma expands slowly along the magnetic field. This may be the reason behind the observed intensity decrease. The decreased intensity may be going right to some other emissions. The intensity enhancements in some previous reports may be due to this.

Electron-impact collisions are supposed to be the dominant process producing excited species in expanding plume. In other words, we could say that any change in electron density affects the observed intensity of an emission line. Since the presence of magnetic field largely deviates the expansion direction of electrons (because of their low mass), the reduction in intensity is also attributed to the deficiency of electrons in the observable volume [16] at the entrance slit of spectrometer.

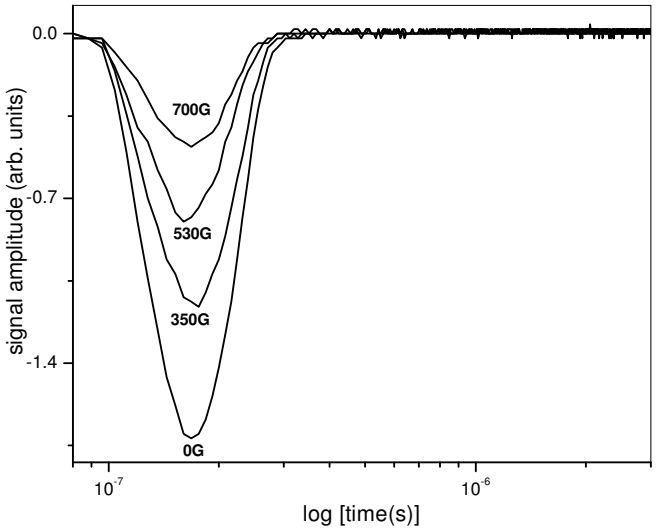

Fig 4. 8: Temporal profile of Li II (5484Å) with magnetic field in diffusion vacuum. laser energy is 140mJ.

Harilal et al. [15] also observed a considerable reduction in intensity for the neutral and singly ionized Al plasma species and an enhanced emission from multiply charged Al ions in a transverse magnetic field. Their conclusion is that the relative rise in intensity of transitions involving higher levels is mainly due to rise in the mean electron energy in the plasma. This also suggests that the intensity of recombination radiation is strongly reduced by the field. Rai *et al.* [17] attributed the reduction in emission intensity in the presence of a magnetic field to loss of plasma energy, which may be due to the opening of a new channel of loss in the content of plasma energy. The generation of

instabilities and high-energy particles in the plasma along with self-absorption of emissions by the plasma may be the reason for the loss of plasma energy.

Both the neutral and singly ionized species are showing the same delay, with and without the presence of magnetic field. This means that magnetic field does not much affect the arrival time distribution of the ejected species.

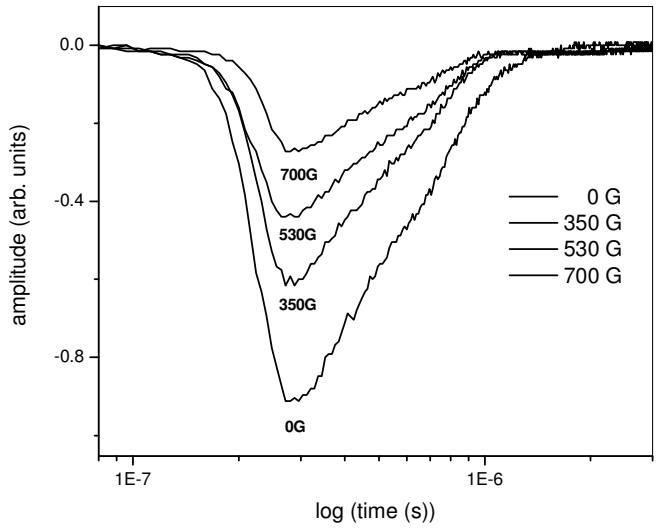

Fig 4. 9: Temporal profile of Li I (6103Å) with magnetic field in diffusion vacuum and at laser energy of 140mJ.

4.5.2. Effect of magnetic field on LIP in argon ambient

The ambient gas greatly influences the temporal profiles of the expanding plume. The slow components appear strongly at 6mm distance. As the neutrals are one of the major constituent species in the plume and ambient gas is the prime source responsible for excitation/ionization of neutral atoms. The increase in emission intensity of expanding plume in background gas is mainly due to two processes: (i) excitations due to collisions with background atoms and (ii) electron impact excitation. Of these two cases, electron impact processes plays the dominant role in the enhancement of the excited species in expanding plasma [18, 19]. The interaction between the expanding plasma and ambient gas causes the ionization of

buffer gas resulting in production of more number of free electrons. The enhanced electron density leads to increase in excitations of species [20].

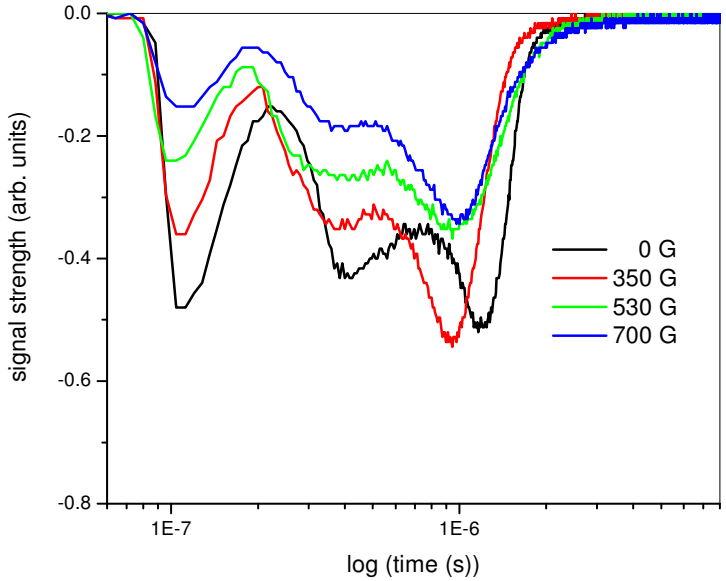

Fig 4.10: Multiple peak structure of LiI (6708Å) in magnetic field at 1mbar pressure. Laser energy is 140mJ.

With ambient argon (1mbar), the neutral profiles show both double peak and triple peak behaviour. Each component of the multiple peak structures shows independent response to the applied field. The plasma is more electron rich, as the argon-excited states are also abundant. It has been shown that plasma formed in argon atmosphere is hotter and denser compared to air as the ambient [21]. Here there is more probability that different fractions of the respective emitting species (neutral or charged) will be of a different origin and therefore different time scales will be involved in the emission, when we look upon the time profile of a specific emission at a definite wavelength. The response of the peak structures are seen in the results presented in figures 4.10 and 4.11.

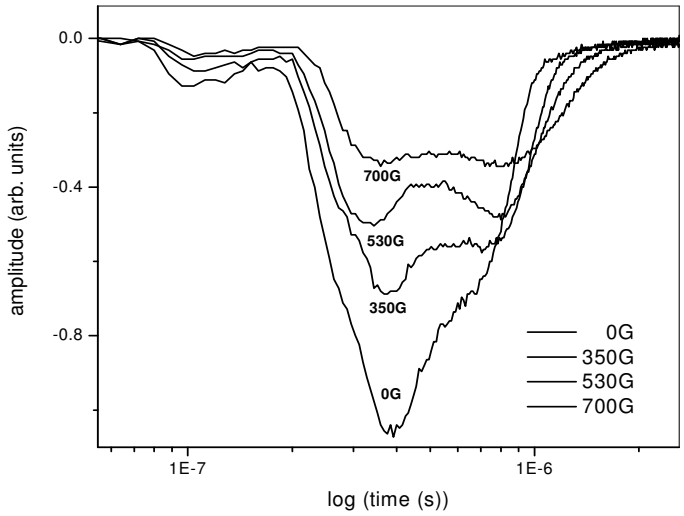

Fig 4.11: Multiple peak structure of LiI (6103Å) in magnetic field at 1mbar pressure. Laser energy is 140mJ.

4.5.3. Splitting of neutral line profiles

Excited neutral species are sustained for a longer time in the plume compared to the singly ionized species (figures 4.8 and 4.9). i.e., neutral profiles are much broader than those of ionic species. This suggests that the effects of magnetic field are more on neutral species. This is because the major constituent of the plume is neutrals and the excitation source is the electron impact collision processes. So, any deviation in the electron density could be reflected on the observed emission intensity of neutral species also.

The temporal profiles of neutral plasma species in the field show a splitting. Formation of an additional peak in the line profile of neutral species (6708Å) is the result of a plume splitting in the field. For the neutral line at 6708 Å in vacuum, this new peak has been recorded 1μs after the original emission. An earlier appearance of the second peak is found in ambient argon at 1mb. This can be seen in the time profile of Li I (6103Å) in the plasma produced by irradiating the target with 140mJ of laser energy (Fig.4.11) over a spot of diameter 1mm.

In addition to those formed from the laser excitation, neutrals are also produced by recombination processes:

$$A^+ + e^- \rightarrow A \qquad (4.12)$$

The electrons in the plume are effectively magnetized by the magnetic field lines than the ions. However, the inhomogeneous space-charge which results from this generates an electric field in a direction perpendicular to the laser spot axis, which will attract the ions towards the central axis of the plume. In effect, a progressive drift of charges takes place and the magnetic field will indirectly confine the ions as well as the electrons [22, 23]. It is expected that fast electrons and ions travel at the leading edge of the plasma. After the laser action ceases, the charge composition of the plasma is governed by three body recombination, which dominates over radiative and electronic effects due to the rapid drop in electron temperature as the plasma expands. The ions located at the front of the plasma acquire the largest energy during hydrodynamic acceleration and their interaction time for recombination is very much reduced [24]. Thus, the recombination are delayed and this may be the reason for a delayed peak (Fig. 4.12). This is found to exist at distances greater than 6mm. Another possible effect for the existence of delayed peak with neutrals is the back flow of the particles towards the target, after the collapse of diamagnetic cavity of the plasma.

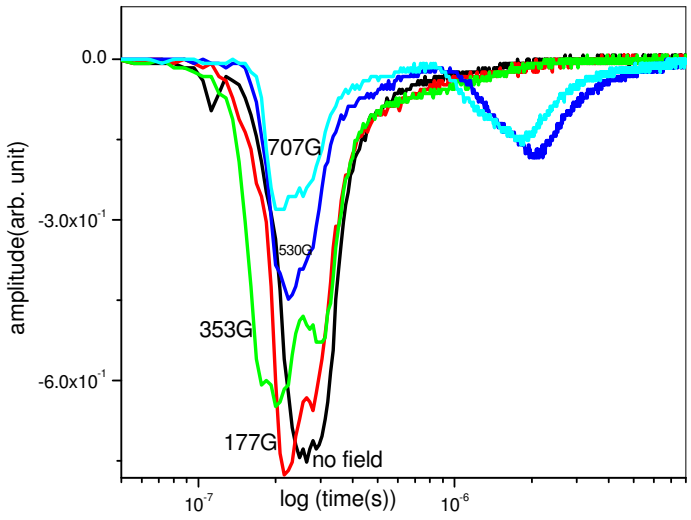

Fig 4.12: Vacuum profile of Li I (6708Å)in magnetic field at laser energy of 140mJ.

4.6. Summary

The main objective of the experiments presented here is to investigate the behaviour of LIP under the influence of a perpendicular magnetic field. The plume is

created using a ns laser pulse hitting a lithium rod in vacuum and argon ambient environments. The pulsed magnetic field applied to plasma has been created using a Helmholtz coil. The plasma is examined using spectroscopic measurements and found that the magnetic field does not much affect the arrival time distribution of the ejected species but the intensity of visible radiation is modulated by the field. Neutrals are greatly affected by the modified collisions and recombination behavior.

4.7. References

[1] Ira B. Bernstein, Phys. Rev. 109 10 (1958)

[2] Linlor W I, Appl Phys Lett 3 210 (1963)

[3]William I. Linlor, Phy Rev lett 12 383 (1964)

[4]M Mattioli and D Veron, Plasma Phys 11 684 (1969)

[5] Haught A F, Polk D H and Fader W J, Phys Fluids 13 2842 (1970)

[6] Tuckfield R G and Schwirzke F, Plasma Phys 11 11 (1969)

[7] Sucov E W, Pack J L, Phelps A V and Engelhardt A G, Phys Fluids 10 2035 (1967)

[8] F F Chen, Introduction to plasma physics (Plenum, New york, 1974)

[9] V N Rai, M Shukla and H C Pant, Pramana, J Phys 52 49 (1999)

[10] T. A. Peyser, C. K. Manka, B. H. Ripin, and G. Ganguli, Phys Fluids B 4 2448 (1992)

[11] B. H. Ripin, J. D. Huba, E. A. McLean, C. K. Manka, T. Peyser, H. R. Burris and J. Grun, Phys Fluids B 5 3491 (1993)

[12] M. VanZeeland, W. Gekelman, S. Vincena, and J. Maggs, Phys Plasmas 10 1243 (2003)

[13] A A Harms, K F Schoepf, G H Miley, Principles of Fusion Energy (World scientific, Singapore, 2000)

[14] J D Huba, N R L Plasma Formulary (Naval Research Laboratory, Washington D C, 2002)

[15] S. S. Harilal, M. S. Tillack, B. O'Shay, C. V. Bindhu, and F. Najmabadi, Physical Review E 69 026413 (2004)

[16] X. K. Shen, Y. F. Lu, T. Gebre, H. Ling and Y. X. Han, J Appl Phy 100 053303 (2006)

[17] V. N. Rai, J. P. Singh, F. Y. Yueh, R.L.Cook, *Laser and Particle Beams 21* 65 (2003)

[18] C. Timmer, S.K. Srivastava, T.E. Hall and A. Fucaloro, J. Appl. Phys. 70 1888 (1991)

[19] H. P. Gu, Q.H. Lou, N.H. Cheung, S.C. Chen, Z. Y. Wang and P.K. Liu, Appl. Phys. B 58 143 (1994)

[20] J. Gonzalo, F. Vega and C.N. Afonso, J. Appl. Phys. 77 6588 (1995)

[21] S. S. Harilal, C. V. Bindhu, V. P. N. Nampoori and C. P. G. Vallabhan, Appl Phys Lett 72(2) 167 (1998)

[22] A Anders, S Anders and I Brown, J Appl Phys 75 (10) 4900 (1994)

[23] R Jordan and J Lunney, Appl Surf. Sci.109/110 403 (1997)

[24] S. S. Harilal, C. V. Bindhu, M. S. Tillack, F. Najmabadi and A. C. Gaeris, J Appl Phys. 93 2380 (2003)

CHAPTER 5

Tomographic reconstructions of optical emissions from laser induced plasma

5.1. Introduction

Imaging techniques are used on a routine basis in fusion research to provide much information about the plasma emissivity, plume shape, emission positions relative to the laser spot etc. Possible fluctuations in the spatial and temporal distribution of different plasma parameters can be monitored by this technique. Another possibility is the production of wavelength dependent emissivity maps of plasma which are always desirable in its diagnostics. Under proper assumptions, spectral emissivity could be expressed as a function of electron temperature and density. This proves to be a useful tool to study edge fluctuations and plasma instabilities in the visible and X-ray wavelengths.

5.2. Tomography of laser induced plasma

The development of the theoretical basis for image reconstruction or tomography is credited to Alan Cormack in the mid 1960's [1, 2]. His research and its subsequent application by Godfrey Hounsfied resulted in the creation of computer-assisted tomography, or the CAT scan and a Nobel Prize in physiology and medicine in 1979. The CAT scan method involves radiating an object with an external X-ray source and combining 2-D profiles into a single 3-D image. It is extensively used in the scientific and medical fields allowing for internal profile of objects through the use of external viewing probes.

But the tomographic reconstruction of plasma is slightly different. Since the plasma is a radiating body, the measuring probe can be a passive collector instead of an irradiating source. The use of photodiodes to collect radiated data is a well known technique in the field. The possible lack of symmetry also demands

the use of multiple detectors in various viewing axes to deconvolve the plasma profile. This introduces the possibility of generating a profile of the visible emissivity along the viewing chords. Experiment described in this section make use of the translation of a single photodiode along various viewing axes to obtain chord integrated emissivity as well as to tomographically create radial profiles of the plasma interior.

In plasma physics, there is a strong demand to reconstruct plasma cross-section from the projection measurements even though they are not complete. Therefore special methods of computer tomography (CT) are developed, which include different physical assumptions. In this chapter, we present results of LIP tomography based on pixel method code, which is best suitable if the plasma cross-section is smooth in polar coordinates with a zero level near the origin.

5.3. Plasma bremsstrahlung and line radiation

In order to gain an accurate understanding of the plasma from tomographic data, it is important to describe exactly what sort of lights the photodiodes detect, how they affect the resulting current and their relationship to plasma density and temperature (mean thermal energy). Energy radiates from plasma in many forms, but for tomography experiments, the two of great interest are bremsstrahlung and line radiation. Bremsstrahlung or braking radiation results from the interaction of ions and electrons undergoing coulomb collisions. As fast moving electrons approach the relatively stationary ions, the long-range coulomb field deflects them into a hyperbolic orbit. This deflection is determined from the point of closest approach in the absence of any electromagnetic forces called the impact parameter (b), and the deflection angle (θ), governed by the following equation [3]:

$$\sin\ \theta = \frac{2\left(\frac{b}{b_0}\right)}{1+\left(\frac{b}{b_0}\right)^2} \tag{5.1}$$

where, b_0 is the relative impact parameter when deflection is 90^0. Electron gets accelerated as it orbits the ion during coulomb collision, resulting in the

production of bremsstrahlung radiation. The power radiated (W) from the interaction between acceleration and the coulomb force is

$$W = \frac{2Z_{eff}^2 e^6}{3(4\pi\varepsilon_0)^3 m^2 c^3 r^4} \tag{5.2}$$

In this equation, Z_{eff} is the effective ion charge, e the electron charge in Coulombs, ε_0 the permittivity of free space, m the ion mass, c the speed of light and r the instantaneous radius of the electron from the ion. Integrating this value over the interaction time produces the following amount of emitted radiation per collision:

$$W_{rad} \approx \frac{\pi Z_{eff}^2 e^6}{3(4\pi\varepsilon_0)^3 m^2 c^3 v b^3} \tag{5.3}$$

where, v is the electron velocity relative to the ion (electron thermal speed). The summation of this equation for all Coulomb collisions represents the total amount of energy emitted from the plasma bremsstrahlung. Manipulating this equation yields the power radiated per unit volume of the plasma, given by:

$$P_{br} \approx \frac{2\pi^2 n_i n_e Z_{eff}^2 e^6 T_e^{1/2}}{3^{1/2}(4\pi\varepsilon_0)^3 m^{3/2} c^3 \hbar} \tag{5.4}$$

where T_e is the electron temperature, $\hbar$ is the Planck's constant, n_i and n_e are the ion and electron densities respectively. Therefore, bremsstrahlung from plasma increases linearly with temperature and density due to the higher rate in coulomb collisions per unit volume.

Line radiation on the other hand, arises from the transitions of bound electrons between energy levels. The power produced per unit volume relates to the combination of electron density and ion density as well as electron temperature [3]. The distinct energy levels of different ions result in line radiation occurring at specific wavelengths that superimpose over the bremsstrahlung radiation.

5.4. Plasma density from chord - integrated emissivity

Chord integrated emissivity from the photodiodes is also useful for comparison of the electron density in the plasma. The radiation per unit volume for each unit of frequency is,

$$\int dP \Big/ d\nu \quad f(\nu) d^3\nu \tag{5.5}$$

where, P is the power per electron and $f(v)$ the electron distribution. If $f(v)$ is isotropic, emissivity in terms of electron and ion density defined by the term j(ν) is [4]

$$j(\nu)\, 4\pi = n_e n_i Z_{eff}^{\ 2} \left(\frac{e^2}{4\pi\varepsilon_0} \right)^3 \frac{32\pi^2}{3\sqrt{3} m^2 c^3} \left(\frac{2m}{\pi T} \right)^{\frac{1}{2}} e^{-h\nu/T}\ \hat{g} \tag{5.6}$$

This equation represents the spectral power emitted over a full spherical solid angle per unit of frequency per unit volume. n_e and n_i represent number densities, Z_{eff} the effective ion charge, e the electron charge in coulombs, T the temperature at thermal equilibrium, hv the quantum of energy and ĝ the Maxwell averaged Gaunt factor. Taking the emissivity over areas of low line radiation and low photon energy reduces this equation to simply the number densities multiplied by a constant so that [5],

$$E \quad \propto \quad n_e^{\ 2} \tag{5.7}$$

Therefore by viewing the wavelength region of the plasma with significant emission through bremstrahlung, it is possible to determine a general density profile of the plasma.

5.5. Pixel method for tomographic reconstruction

The pixel method for tomographic inversion can be effectively used to get information about the laser energy dependent emission characteristics of LIP expanding into vacuum. A photo detector (silicon PIN detector having 1ns rise time) which responds to the wavelength range, 350nm-1000nm, is used to detect the visible emissions. The detector of diameter 0.8mm is made to observe the plasma through a cone of small solid angle, and the axis of this cone is designated as the chord. A hollow cylindrical structure of length 5cm is fixed in front of the

detector such that the cross sectional area of the cylinder is the same as the detector. This collimated geometry is implemented so that the detector does not see a trapezoidal area of the plasma. The desired field of view is covered by linearly translating the detector-aperture system.

The emitting region is divided into pixels, within which the emissivity is assumed to be constant. A number of such pixels are always seen by the detector and the local emissivity values are calculated from the system of simultaneous linear equations formed, when all the detector positions are taken into account [6, 7]. A radial profile of emissivity distribution within the LIP is generated and an analysis of the results is presented.

Light pulses from a nanosecond laser have been focused on a solid target of titanium kept inside an evacuated metal chamber. The detector is translated in equal steps to collect the emissions from the expanding plasma. Data perpendicular to this also has been used to tomographically recreate an emissivity map stretched along a plane which is perpendicular to the plane of the solid target used. Fig.5.1 shows the schematic diagram for the chord selection and the geometry of data collection.

The tomography problem consists of solving the system of integral equations [8-10],

$$\int_s f(x,y) = \int_L g(\alpha,\beta)dL \qquad \text{(where, } s = 1, 2, 3...M\text{)} \qquad (5.8)$$

where each chord sees the plasma through a cone of small solid angle and the axis of this cone designated as the chord is defined by *(x,y)*. Here *x* is the perpendicular distance of the detector from the plasma centre, *y* is its distance from the plasma centre along the target normal, *f(x,y)* is the chord brightness in $W/m^2/Sr$ and *g* is the local emissivity in $W/m^3/Sr$. The integral is along the line of sight and *M* is the number of available measurements (number of detector positions). Here the origin of co-ordinate system is the plasma centre which is the laser hit point on the target. The pixel system for tomographic inversion is shown in Fig.5.2.

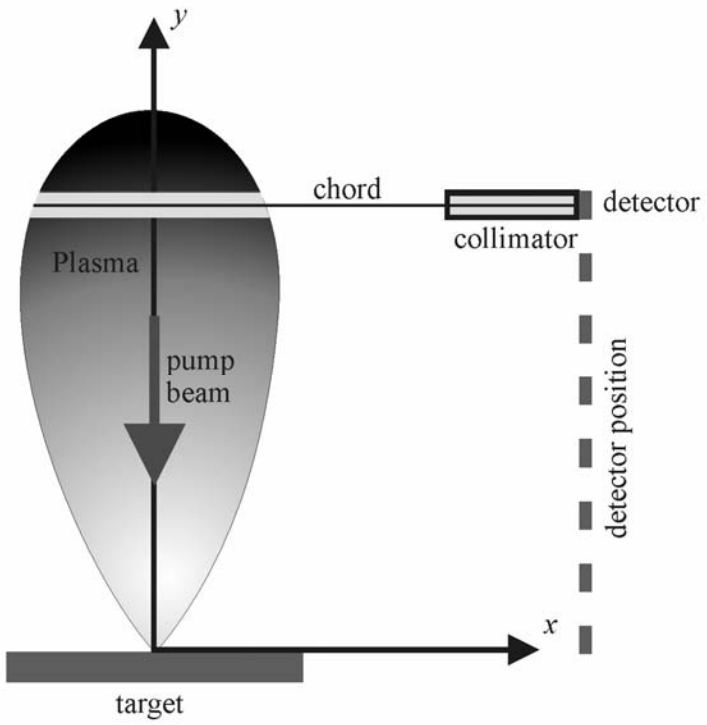

Fig.5.1: Geometry of data collection and co-ordinate system for tomographic inversion problem.

The pixel shapes may be of different types like square pixels, concentric pixels, etc [11, 12]. In our study, square pixels are assumed. Each detector sees a number of these pixels. The brightness *f* measured by detector 1 from *N* pixels is,

$$I_{11}g_1 + I_{12}g_2 + ...I_{1N}g_N = f_1 \tag{5.9}$$

where I_{11} is the fraction of the emission incident on detector 1 from pixel 1, g_1 is the emissivity at pixel 1 and so on. Similarly, emissions measured by other detectors will follow the same equation. In compact form, the set of simultaneous linear equations can be written as,

$$I * g = f \tag{5.10}$$

where, * denotes the usual matrix multiplication. The matrix element I_{lj} is assumed to be proportional to the chord length of the detector *l*, passing through the pixel number *j*. So, the

order of the matrix is the number of detectors (detector positions) times the number of pixels (*M x N)*. An inversion of *I* in equation (8) yields the emissivity contours.

Direct inversion is not always possible if the system is under-determined (the number of equations are less than the number of unknowns)or over-determined (the number of equations are more than the number of unknowns). In the case of *over-determined system*, we could try to minimize chi-squared $\left(\chi^2\right)$ value using the well-known equation given in equation 5.11.

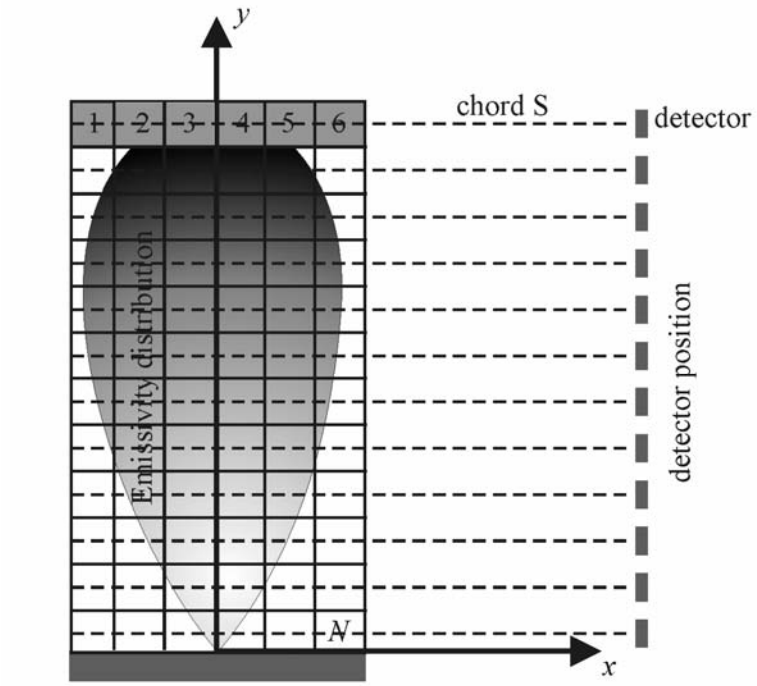

Fig 5.2: Pixel system for the tomographic inversion problem.
The pixels that contribute to chord S are shaded

$$\chi^2 = \left(\tilde{I} * g - \tilde{f}\right)^T * \left(\tilde{I} * g - \tilde{f}\right) \tag{5.11}$$

The subscript *T* denotes transposition and $\tilde{I}_{li} = \frac{I_{li}}{\sigma_l}$, $\tilde{f}_{li} = \frac{f_{li}}{\sigma_l}$, where σ_l is the standard deviation of the detector *l* measuring f_{li}. The solution of (8) in terms of least square fit for over-determined system is,

$$\tilde{I}^{T} * \tilde{I} * g = \tilde{I} * \tilde{f} \tag{5.12}$$

In the case of *under-determined* system, we can always get $\chi^2 = 0$, because the number of solutions is infinite. Hence to find a unique and acceptable solution, instead of minimizing χ^2 alone, one can look for the minimization of function *f*, which can be defined as [13, 14],

$$\phi = \chi^2 + \lambda \Re \tag{5.13}$$

$\Re$ is called the regularizing operator, whereas λ is called the regularization parameter, whose value is always positive and lies between 0 and ∞, i.e., $0<\lambda<\infty$. In fact, regularization parameter λ does the work of a trade-off between the goodness of the fit represented by χ^2 and requirements imposed on the solution *g* by the regularizing operator, $\Re$. Hence to get the correct value of λ for a given regularizing operator, a subjective criterion is to pick up any value of λ in between 0 and ∞ and find out the value of χ^2, which should lie in twin acceptable choices $N \pm (2N)^{1/2}$, where *N* is the number of measurements.

5.6. Linear Regularization

The linear regularization method smooths the solution apart from providing a reasonable fit to the data [13, 15].

5.6.1. First order linear regularization

First order linear regularization minimizes the gradients. So the regularization operator $\Re$, which measures the "roughness", can be expressed in two dimensions as

$$\Re = \left\| g'_x \right\|^2 + \left\| g'_y \right\|^2 \tag{5.14}$$

where $\|\otimes\|$ denotes the Euclidian vector norm, g'_x and g'_y are the partial derivatives with respect to *x* and *y*. If g'_x and g'_y can be represented by finite-difference matrix representation with the symbol ∇_{xg} and ∇_{yg} respectively, then the regularization operator, $\Re$ in (14) takes the form,

$$\begin{aligned} \Re &= \left(\nabla_{xg}\right)^T * \nabla_{xg} + \left(\nabla_{yg}\right)^T * \nabla_{yg} \\ &= g^T \left(\nabla_x^T * \nabla_x + \nabla_y^T * \nabla_y\right) g \end{aligned}$$

$$= g^T * H * g \text{ , where, } H = \nabla_x^T * \nabla_x + \nabla_y^T * \nabla_y \tag{5.15}$$

Combination of Eqs. (11), (13) and (15) gives,

$$\phi = \left(\tilde{I} * g - \tilde{f}\right)^T * \left(\tilde{I} * g - \tilde{f}\right) + \lambda g^T * H * g \tag{5.16}$$

setting all partial derivatives $\partial\phi / \partial g_i$ to zero, to minimize (16), the solution of (8) takes the form,

$$\left(\tilde{I}^T * I + \lambda H\right) * g = \tilde{I}^T * \tilde{f} \tag{5.17}$$

5.6.2. Second order linear regularization

Second order linear regularization selects the solution with least curvature. The regularization operator, $\Re$ in this case can be written as,

$$\Re = \left\| \nabla^2 g \right\|, \tag{5.18}$$

where ∇^2 is the Laplacian operator in two dimensions. If the finite difference matrix representation of the Laplacian is Δ, then (18) takes the form,

$$\begin{aligned} \Re &= (\Delta g)^T * \Delta g \\ &= g^T \left(\Delta^T * \Delta\right) g \\ &= g^T (H) g \end{aligned}$$

$$\text{where, } H = \Delta^T * \Delta \tag{5.19}$$

5.7. Irradiance dependence of LIP emissivity by pixel method

The collected intensity which always falls with distance (y) from the target, follows an approximate 1/y dependence in some cases, as given in Fig.5.3. The perpendicular data (along x) which falls rapidly on either side of the plasma centre, always peaks at the centre. Fig.5.4 shows the tomographic reconstruction of the collected data. Square pixels of size 1mm are used for the reconstruction. In each scan, the first chord (lowermost detector) passes through the point where the laser hits the target. Otherwise, the upper detectors may not see the hot plasma and background emissions can make the reconstructed profile unclear.

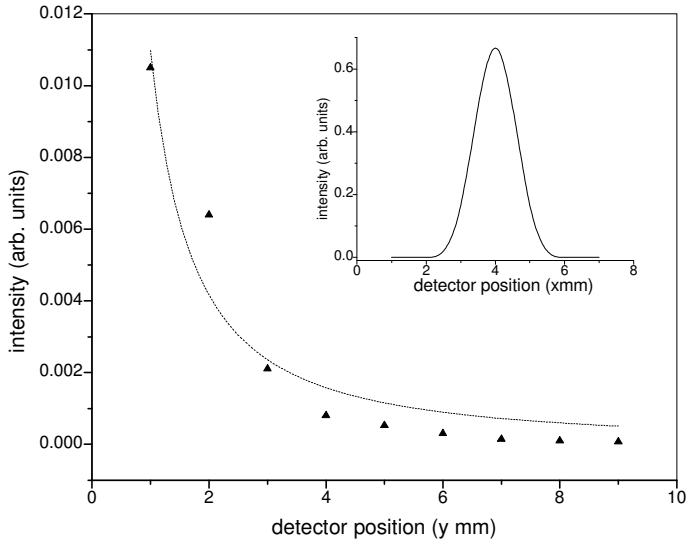

Fig. 5.3: intensity variation at the detector. The solid curve shows the 1/y fit for the data. Inset shows a measurement along the perpendicular direction.

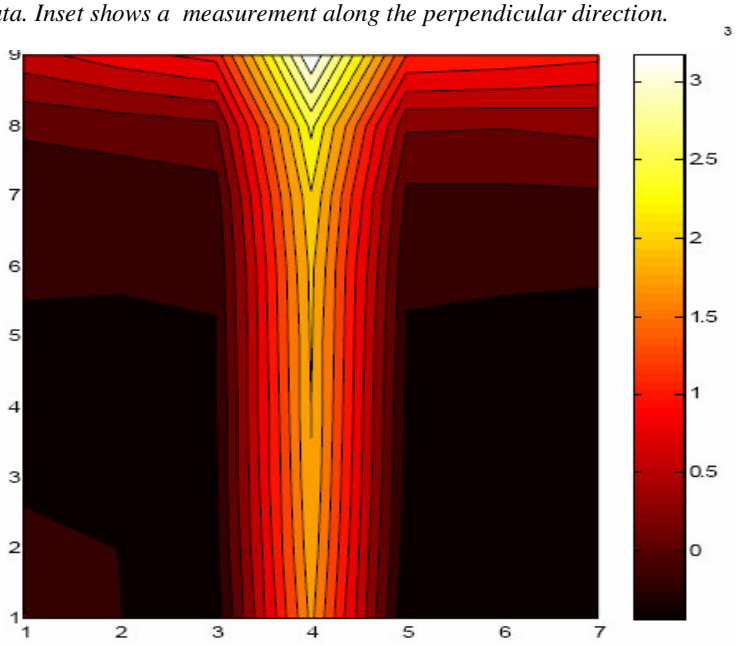

Fig.5.4: tomographic reconstruction of 1/y variation of intensity data. The perpendicular data in the inset of fig: 3 is also used. Vertical axis is along y (cm) and horizontal axis is along x (cm).

Fig.5.5 gives the results of a successful tomographic attempt to recreate the laser irradiance dependent variation of LIP emissivity. This has been done under an assumption that the plasma remains more or less the same under the translation of the detector. The irradiance at the focal spot is varied between 1 $GWcm^{-2}$ and 7 $GWcm^{-2}$. The emissivity contours at four different laser irradiances

(1.3 GW cm^{-2}, 2.6 GW cm^{-2}, 5.2 GW cm^{-2} and 6.5 GW cm^{-2}) are presented. Information from a spatial point very near to the target (at 2 cm from the target) up to 6 cm is included in the map.

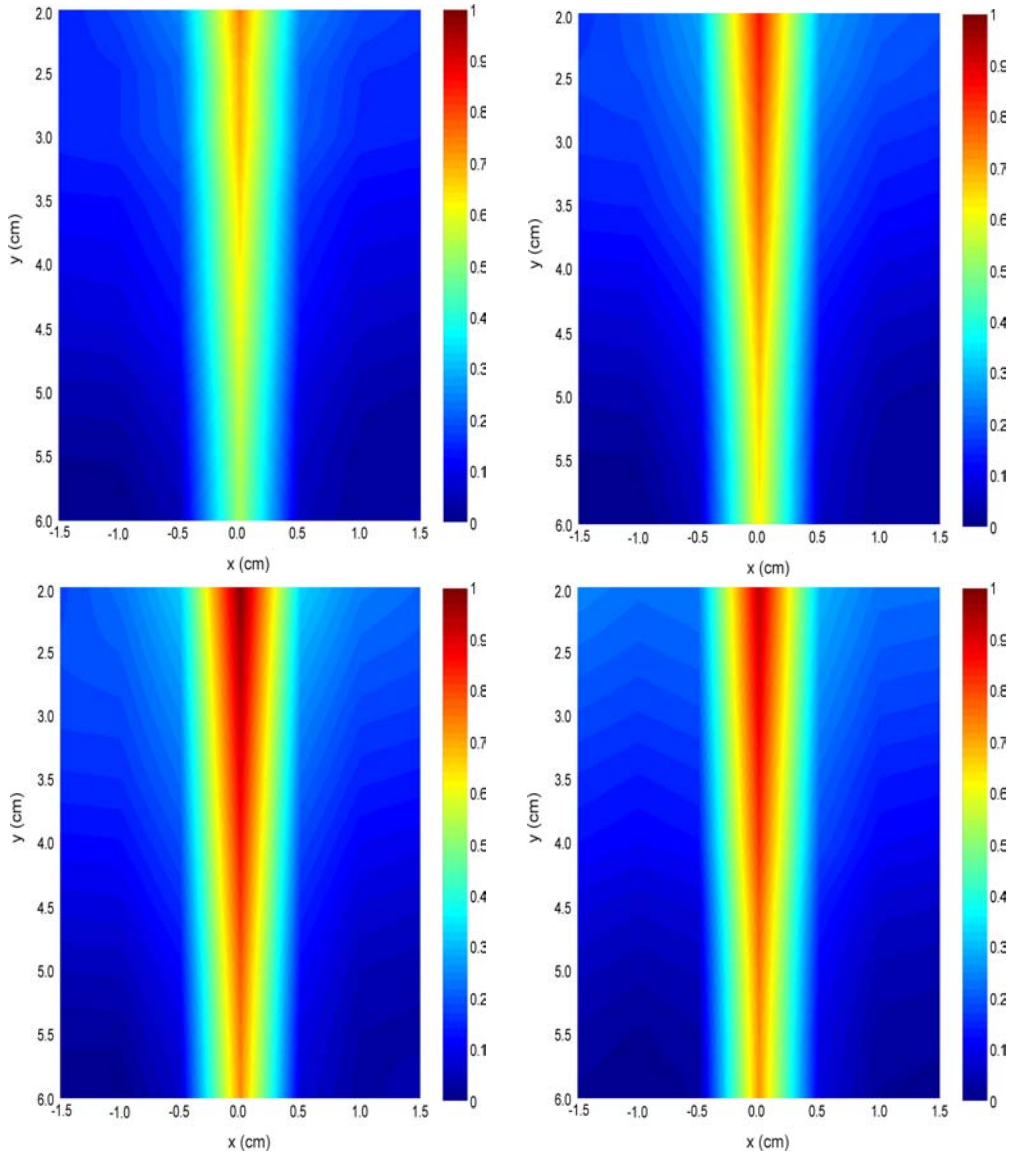

Fig.5.5 : Emissivity maps of LIP with different laser irradiances(Clockwise from top left). The respective fluences are 1.3 GW cm^{-2}, 2.6 GW cm^{-2}, 5.2 GW cm^{-2} and 6.5 GW cm^{-2}.

The dimensions of the plume region giving the emissions increase with the increase in laser irradiance. The emissions are highly directed towards the laser pulse direction, similar to the orientation of the expanding cone of LIP. An emissivity gradient is symmetrically located with respect to the axis. The highest values are concentrated along the axis of the expanding cone. At low irradiances, the region having highest emissivity is confined to distances less than 2 cm. But, in the emissivity map for an irradiance of 6.5 $GWcm^{-2}$, this can be clearly seen even after 3 cm. The emission tail for a comparatively colder plasma region is at 4cm when the irradiance is 1.3 GW cm^{-2} and reaches 5.5 cm with 2.6 $GWcm^{-2}$.

5.8. Reconstruction of time evolution of LIP emissions by pixel method

The time evolution of the emissions is also reconstructed using the intensity data collected at different times. For this, light from different spatial locations of titanium plasma has been collected using a spectrometer, whose photo-multiplier tube (PMT) output is fed to a gated boxcar averager. The light collection is effected with a one-to-one imaging procedure using two lenses, as explained in section 2.2. The spectrometer being tuned at 350.5nm (Ti II transition with the configuration, $3d^2.4s$-$3d^2.4p$), the intensity data collected at the boxcar output has spectral and time resolution and can be used to study the time evolution of Ti II emissions. The results are presented in Fig.5.6. The bottom border of each picture is near the target surface.

The strong emissions at 100ns have sharp contours but become weaker as the plasma expands and beyond 300ns, a progressive degradation of emission strength is observed. It can be clearly seen that with increase of delay, the whole plume is expanded. During the initial period, e.g., 100 and 300 ns delay, the plume remains just above the origin and the expansion is normal to the target surface. The tomographic inversions show that the plume edge (near the target) remains stationary in time during the initial expansion phase (t <300 ns) and subsequently expands laterally, with a radial velocity. At 500ns, its center moved to the top-right direction and an apparent horizontal shift of the center of the plasma can be seen. Such non-normal plume direction has been reported before [16-18].

After the laser strikes the target, the plume is produced from its surface and expands. Then, the remaining part of the laser pulse will interact with the evaporated

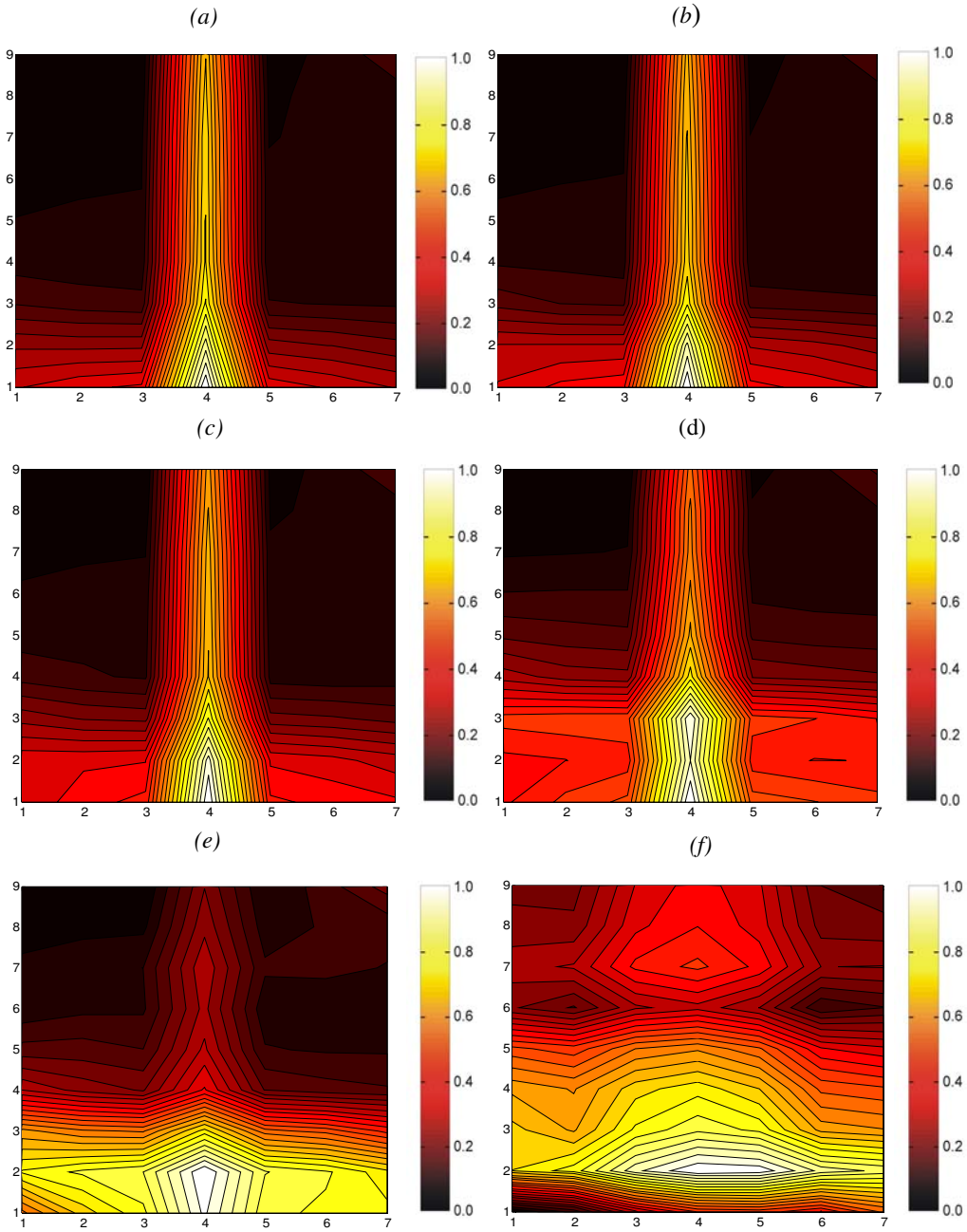

Fig.5.6: Tomographic reconstructions of visible emissions of Ti II at different times with respect to the laser pulse.(a) 100ns (b)150ns (c) 200ns (d) 300ns (e) 400ns (f) 500ns.Horizontal axis is along x (cm) and vertical axis is along y(cm).

materials in the plume and the breakdown will start at the point where the power density of the laser beam reaches the threshold for inducing plasma [19]. The possible asymmetry in the breakdown of the plume contributes a lot to the determination of the plasma direction. In our experiment, the plume is found to expand quite perpendicular to the target surface, from the reconstructions at small delays. It is reasonable to assume that the breakdown will not happen at the exact center of the plume due to the possible inclination of the incident laser or the inhomogeneities in its energy distribution. In such situations, the exact direction of the movement of the plasma center will be determined also by the interaction between the plasma and the target, and the morphology of the target surface [20]. It is really worth noting that the plume remains mostly confined around the axis constituting the target normal, with a velocity component (longitudinal) along this axis larger than the velocity component (radial) perpendicular to the target normal.

With small delays, a bright core (yellow contour) and its blur ambient (red contour) can be observed. This may be considered as arising from the hot plasma core and the vapourous ambient inside the chamber.

5.9. Summary

We have investigated the technical aspects of tomographic imaging on laser produced plasmas using pixel method. The irradiance dependence of emissivity contour and the time evolution of Ti II line emission has been reconstructed by the tomographic inversions of visible emissions. This powerful tool has been proven to provide detailed information that can be used to optimize the different experimental setups and to improve analytical performance.

5.10. References

[1] A.M. Cormack, Journal of Applied Physics Vol. 35(10) 2908 (1964)

[2] A.M. Cormack, Journal of Applied Physics Vol. 34(9) 2722 (1963)

[3] R.J. Goldston and P.H. Rutherford, Introduction to Plasma Physics (Institute of Physics Publishing Institute of Physics, London, 1995) pg 167, 181-183

[4] I. H. Hutchinson, Principles of Plasma Diagnostics (Cambridge University Press, 2nd edition, 2002) pg. 195-196

[5] A. Holland and G.A. Navratil, Review of Scientific Instruments 57(8) 1557 (1986)

[6] Asim Kumar Chattopadhyay, Arun Anand, and C. V. S. Rao, Rev. Sci. Instrum. 76 063502 (2005)

[7] Santanu Banerjee, Asim Kumar Chattopadhyay and P. Vasu, Plasma and Fusion Research: Regular Articles Volume 2 S1120 (2007)

[8] R. S. Granetz and J. M. Camacho, Nucl. Fusion 25 727(1985)

[9] R. S. Granetz and J. M. Camacho, Rev. Sci. Instrum. 57 417 (1986)

[10] R. S. Granetz and P. Smoulders, Nucl. Fusion 28 457 (1988)

[11] J. Mlynar, Czech. J. Phys. 45 799 (1995)

[12] J. H. Williamson and D. E. Evans, IEEE Trans. Plasma Sci. PS-10 82 (1982)

[13] W. H. Press, S. A. Teuklosky, W. T. Vetterling and B. P. Flannery, Numerical Recipes in Fortran: The Art of Scientific Computing, 2nd ed. (Cambridge University Press, Cambridge, 1992)

[14] W. von der Linden, Appl. Phys. A: Mater. Sci. Process. 60 155 (1994)

[15] M. Anton and H. Weison, Plasma Phys. Controlled Fusion 38, 1849 (1996).

[16] S. R. Foltyn, Pulsed Laser Deposition of Thin Films, D. B. Chrisey and G. K. Hubler (Wiley, New York, 1994) p. 109

[17] R. Pinto, S. P. Cai, C. P. D'Souza, L. C. Gupta and R. Vijayaraghavan, Physica C 196, 264 (1992)

[18] Y. Ito, I. Oguro, Y. Fukuzawa and S. Nakamura, Proc. SPIE 4065, 461 (2000)

[19] R. K. Singh and J. Narayan, Phys. Rev. B 41, 8843 (1990)

[20] William Whitty, Jean-Paul Mosnier, Applied Surface Science 127–129 1035 (1998)

CHAPTER 6

Study of plasma dynamics using reconstruction of digital interferograms

6.1. Introduction

Refractive index is one of the basic parameter that characterizes plasma. Therefore, measurement and mapping of the refractive index distribution with fine spatial and temporal resolution is of primary interest in plasma diagnostics [1]. Mapping of the refractive index will provide information on spatial as well as temporal distribution of density, temperature, impurity concentration etc existing in the system. Plasma acts as a phase object which introduces a phase change to the probe wavefront passing through it. A convenient way to image or gain information on the state of the system is to find this change in phase. Usually optical interferometry is used for this phase measurement.

Interferometric methods could be used to determine the electron density distributions existing in plasma [2]. With the advent of CCD cameras and fast computers, it has become possible to record interferograms digitally and reconstruct them numerically [3, 4]. The wave field passing through the object under study and a coherent background radiation, interfere and produce micro-interference patterns [5]. These are recorded and the amplitude and phase of the wave field are reconstructed. Chord integrated density information is retrieved from the phase maps and the chord integrated measurement is tomographically inverted using an Abel inversion method to determine the radial electron number density profile of the plasma. The main advantage of this digital technique over conventional methods is that, as the numerical reconstruction procedures are adopted, the amplitude and phase of the wave field are directly obtained without the conventional phase stepping techniques.

6.2. Basic theory of the technique

6.2.1. Introduction

Dennis Gabor [5-7] invented holography in 1948 as a method for recording and reconstructing the amplitude and phase of a wavefield. Hologram is the photographically or otherwise recorded interference pattern between a wavefield scattered from the object and a coherent background, called the reference wave. The recording is usually made on a flat surface, but contains information about the entire three-dimensional wavefield. This information is coded in the form of bright and dark micro-patterns which are usually not visible to the human eye due to the high spatial frequencies. The object wave can be reconstructed by illuminating the hologram with the reference wave. This reconstructed wave is indistinguishable from the object wave. An observer sees a three dimensional image which exhibits all the effects of perspective and depth of focus.

One major application of holography is holographic interferometry (HI) developed in the late 1960s by Stetson and Powell[8, 9]. With HI, it became possible to map the displacements of rough surfaces with an accuracy of a fraction of a micrometer. It is also possible to make interferometric comparisons of stored wavefronts that exist at different times.

The development of computer technology made it possible to transfer either the recording process or the reconstruction process into the computer. The first approach led to computer generated holography (CGH), which allows us to generate artificial holograms by numerical methods. These computer generated holograms are then optically reconstructed [10, 11].

Numerical hologram reconstruction was initiated by Yaroslavskii et al [12-14] at the early 1970s. They sampled optically enlarged parts of in-line and Fourier holograms recorded on a holographic plate. These digitized conventional holograms were reconstructed numerically. Onural and Scott [15-17] improved the reconstruction algorithm and applied this method to particle measurements. Haddad et al [18] described a holographic microscope based on numerical reconstruction of Fourier holograms.

A big step forward was the development of direct recording of Fresnel holograms with charged coupled devices (CCDs) by Schnars and Juptner [19, 3]. This method which enables full digital recording and numerical hologram reconstruction, is called digital holography. Digital hologram reconstruction offers much more possibilities than conventional

(optical) processing. The phases of the stored light waves can be calculated directly from the digital holograms, without generating phase-shifted interferograms [20]. Other methods of optical metrology such as shearography or speckle photography can be derived numerically from digital holograms. This means that, after hologram recording, one can choose the interferometric technique (hologram interferometry, shearography or other technique) by mathematical methods.

Since the mid-1990s, digital holography has been modified, improved and applied to several measurement tasks. Important steps are:

- improvements in the experimental steps and reconstruction algorithm [21-37]
- applications in encrypting information [38, 39]
- measurement of refractive index distributions within transparent media [40]
- Development of comparative digital holography [41]

6.2.2. Hologram recording and reconstruction

In the general setup for recording off axis holograms [42, 43], light with sufficient coherence length is split into two partial waves by a beam splitter. One wave illuminates the object and get scattered and reflected to the recording medium. The second wave called the reference wave directly illuminates the recording medium. The interference pattern is recorded on a suitable recording medium. During optical reconstruction, the hologram is illuminated with the reference wave and the original object wave is reconstructed. The holographic process is described mathematically as follows:

$$O(x,y) = o(x,y)\exp(i\varphi_o(x,y)) \tag{6.1}$$

is the complex amplitude of the object wave with real amplitude *o* and phase φ_0 .

$$R(x,y) = r(x,y)\exp[i\varphi_r(x,y)] \tag{6.2}$$

is the complex amplitude of the reference wave with real amplitude r and phase φ_r .

Both waves interfere at the surface of the recording medium. The intensity is calculated by,

$$\begin{aligned} I(x,y) &= [O(x,y) + R(x,y)]^2 \\ &= [O(x,y) + R(x,y)]\ [O(x,y) + R(x,y)]^* \\ &= R(x,y)R^*(x,y) + O(x,y)O^*(x,y) + O(x,y)R^*(x,y) + R(x,y)O^*(x,y) \end{aligned} \tag{6.3}$$

where * denotes the complex conjugate. The amplitude transmission *h(x,y)* (also called the hologram function) is proportional to *I(x,y)*,

$$h(x,y) = \beta\tau I(x,y) \tag{6.4}$$

where β is a constant and τ is the exposure time.

For hologram reconstruction, the amplitude transmission has to be multiplied with the complex amplitude of the reference wave:

$$R(x,y)h(x,y) = \left[\beta\tau\left(r^2 + \sigma^2\right)\right]R(x,y) + \beta\tau r^2 O(x,y) + \beta\tau R^2(x,y)O^*(x,y) \tag{6.5}$$

The first term on the right side of this equation is reference wave multiplied by a factor. It represents the undiffracted wave passing through the hologram (zero diffraction order). The second term is the reconstructed object wave, forming the virtual image. The factor $\beta\tau r^2$ only influences the brightness of the image. The third term produces a distorted real image of the object. For off-axis holography, the virtual image, the real image and the undiffracted wave are spatially separated.

6.2.3. Holographic interferometry (HI)

HI is an optical method to observe deformations of opaque bodies or refractive index variations in transparent media, like fluids, gases or plasmas. HI is a non-contact, non-destructive method with very high sensitivity. Optical path changes up to $1/100^{th}$ of the wavelength are resolvable.

Two coherent wave fields, which are reflected from two different states of the object are interfering. In double exposure holography, two wave fields are recorded on a single photographic plate. The first exposure represents the object in its initial state and the second exposure represents the object in an intermediate state. During reconstruction, as a result of the two holographic recordings with slightly different object waves, an image superimposed by interference fringes is obtained. From this holographic interferogram, the observer can determine optical path changes due to different reasons. The following mathematical description is valid for the technique:

The complex amplitude of the object wave in the initial state is,

$$O_1(x,y) = o(x,y)\exp\left(i\varphi(x,y)\right) \tag{6.6}$$

where o is the real amplitude and φ is the phase of the object wave.

Optical path changes due to deformations of the object surface can be described by a variation of the phase from φ to $\varphi + \Delta\varphi$. $\Delta\varphi$ is the difference between the initial and actual phase, and is called the interference phase. The complex amplitude of the actual object wave is therefore denoted by,

$$O_2(x, y) = o(x, y)\exp[i(\varphi(x, y) + \Delta\varphi(x, y))] \tag{6.7}$$

The intensity of a holographic interference pattern is described by the square of the sum of the complex amplitudes. It is calculated as follows:

$$I(x, y) = |O_1 + O_2|^2 = (O_1 + O_2)(O_1 + O_2)^*$$

$$= 2o^2(1 + \cos\Delta\phi) \tag{6.8}$$

The interference phase is the key to calculate refractive index changes within transparent media.

6.2.4. Digital holography

In the general setup [44] for digital recording of off-axis holograms, a plane reference wave and the object wave are interfering at the surface of a CCD. In fact, any light sensitive device which can make digital images can be used to record digital holograms. The resulting hologram is electronically recorded and stored. The object is a three dimensional body, with diffusely reflecting surface, located at a fixed distance, *d*, from the CCD. The reconstruction of the object wave field is numerically performed using scalar diffraction theory, by simulating the diffraction process happening in the hologram, when illuminated with the reference wave. During reconstruction, the virtual image appears at the position of the original object and the real image also is formed at a distance, *d,* but in the opposite direction from the CCD. The diffraction of a light wave at an aperture which is fastened perpendicular to the incoming beam is described by the Fresnel – Kirchoff diffraction integral.

6.2.5. Digital holographic interferometry (DHI)

In conventional HI, two waves scattered from an object in different states are superimposed. The resulting holographic interferograms carry the information about the phase change between the waves. However, the interference phase cannot be extracted unequivocally from a single interferogram. The interference phase is usually calculated from three or more phase-shifted interferograms by a phase-shifting algorithm. This requires additional experimental effort. In digital holography, a completely different way of processing is possible [20]. In each state of the object, a digital hologram is recorded. Instead of superimposing these holograms, the digital holograms are reconstructed separately. After the phase retrieval, the difference between the individual phases are taken to obtain the interference phase, $\Delta\phi$.

6.3. Relation between interference phase and free electron density

Interference phase ($\Delta\varphi$) is proportional to the integral of the refractive index along the path of the laser light:

$$\Delta\varphi = \int_0^s \frac{2\pi}{\lambda}(n - n_0)dz \tag{6.9}$$

where s is the size of the plasma and λ is the wavelength of the probe pulse, n is the refractive index distribution in the plasma, and $n_0 \approx 1$ is the refractive index of the background medium. This change of index $[(n - n_0 = \Delta n)]$ is related to the density of free electrons (n_e) as,

$$(n_0 + \Delta n) = n = \sqrt{\varepsilon} = \sqrt{1 - \frac{\omega_p^2}{\omega^2}} = \sqrt{1 - \frac{n_e}{n_{cr}}} \tag{6.10}$$

where, ε is the dielectric permittivity of plasma, ω is the frequency of the probe pulse, n_{cr} is the plasma cut-off density above which no electromagnetic wave can propagate through plasma and,

$$\omega_p = \sqrt{n_e e^2 / \varepsilon_0 m} \tag{6.11}$$

is the plasma frequency. From the above relation, we obtain the density of free electrons as [45],

$$n_e = -2\Delta n n_{cr} \tag{6.12}$$

Ions and neutral particles also shift the phase of the probe beam but their contribution is small enough that it can be safely neglected as the plasma density is small compared to the cut-off density. The cut-off density in the plasma,

$$n_{cr} \equiv \left(\frac{2\pi c}{\lambda}\right)^2 \frac{m_e \varepsilon_0}{e^2}, \tag{6.13}$$

is $2 \cdot 78 \times 10^{21} cm^{-3}$ at the wavelength $(632 \cdot 8nm)$ of the probe laser.

6.4. Scalar diffraction theory using angular spectrum propagation

In MKS units and in the absence of free charge, the Maxwell's equations are given by,

$$\nabla \times \vec{E} = -\mu \frac{\partial \vec{H}}{\partial t} \tag{6.14}$$

$$\nabla \times \vec{H} = \varepsilon \frac{\partial \vec{E}}{\partial t} \tag{6.15}$$

$$\nabla \cdot \varepsilon \vec{E} = 0 \tag{6.16}$$

$$\nabla \cdot \mu \vec{H} = 0 \tag{6.17}$$

Here, $\vec{E}$ is the electric field, with rectilinear components (E_x, E_y, E_z), and $\vec{H}$ is the magnetic field, with components (H_x, H_y, H_z). μ And ε are the permeability and permittivity respectively, of the medium in which the wave is propagating. $\vec{E}$ and $\vec{H}$ are functions of both position P and time t. The symbol $\nabla = \frac{\partial}{\partial x}\hat{i} + \frac{\partial}{\partial y}\hat{j} + \frac{\partial}{\partial z}\hat{k}$, where $\hat{i}, \hat{j}, \hat{k}$ are unit vectors in the x, y and z directions respectively. The propagation is assumed to be in a linear, isotropic, homogenous, non-dispersive and non-magnetic medium.

Taking the curl of Eq. (14), and making use of the vector identity,

$$\nabla \times \left(\nabla \times \vec{E}\right) = \nabla\left(\nabla \cdot \vec{E}\right) - \nabla^2 \vec{E} \tag{6.18}$$

we write,

$$\nabla^2 \vec{E} - \frac{n^2}{c^2}\frac{\partial^2 \vec{E}}{\partial t^2} = 0 \tag{6.19}$$

where n is the refractive index of the medium defined by,

$$n = \left(\frac{\varepsilon}{\varepsilon_o}\right)^{1/2} \tag{6.20}$$

ε_0 is the vacuum permittivity and c is the velocity of propagation in vacuum, given by;

$$c = \frac{1}{\sqrt{(\mu_0 \varepsilon_0)}} \tag{6.21}$$

The magnetic field also satisfies an identical wave equation. Since the vector wave equation is obeyed by both $\vec{E}$ and $\vec{H}$, an identical scalar wave equation is obeyed by all components of those vectors. Thus, for example, E_x obeys the equation,

$$\nabla^2 E_x - \frac{n^2}{c^2}\frac{\partial^2 E_x}{\partial t^2} = 0 \tag{6.22}$$

and similarly for E_y, E_z, H_x, H_y, H_z. Therefore, it is possible to summarize the behavior of all components of $\vec{\varepsilon}$ and $\vec{\mathrm{H}}$ through a single scalar wave equation,

$$\nabla^2 u(P,t) - \frac{n^2}{c^2}\frac{\partial^2 u(P,t)}{\partial t^2} = 0 \tag{6.23}$$

where, $u(P,t)$ represents any of the scalar field components.

From the above discussion, we conclude that in a dielectric medium that is linear, isotropic, homogeneous and non-dispersive, all components of the electric and magnetic field behave identically and their behavior is fully described by a single scalar wave equation.

But if the medium is inhomogenous, non-isotropic etc, there will be coupling between various components of the electric field with the result that E_x, E_y and E_z may not satisfy the same wave equation. Similar conditions are encountered when boundary conditions are imposed on a wave that propagates in a homogenous medium. At the boundaries, coupling is introduced between the electric and magnetic fields as well as between their various components. Therefore, even when the medium of propagation is homogenous, the scalar diffraction theory introduces some degree of error. This error will be small as the boundary conditions have effects over very small area compared to the total area of propagation. In diffraction by an aperture, the electric and magnetic fields are modified only at the edges, where the light interacts with the material of which the edges are composed, and the effects extend only over a few wavelengths into the aperture itself. If the aperture is large compared to the wavelength of incident radiation, the coupling effects of the boundary conditions on electric and magnetic fields can be ignored.

The scalar field for monochromatic waves can be represented as [46],

$$u(P,t) = A(P)\cos[2\pi\nu t + \phi(P)] \tag{6.24}$$

where $A(P)$ is the amplitude and $\phi(P)$ is the phase of the wave at position P. ν is the optical frequency. Eq. (6.19) can also be written in complex form as,

$$u(P,t) = \mathrm{Re}\{U(P)e^{-i2\pi\nu t}\} \tag{6.25}$$

where Re{ } is the real part of the complex function $U(P)$ which is also called the complex amplitude.

$$U(P) = A(P)e^{-i\phi(P)} \tag{6.26}$$

The disturbance given in Eq. (6.25) also satisfies the scalar wave equation given by Eq. (6.23). Since monochromatic waves are considered here, the time dependence is known a priori. Hence, $U(P)$ represents the disturbance adequately and it follows that, U must obey the time independent equation,

$$\left(\nabla^2 + k^2\right)U = 0 \tag{6.27}$$

where, $k = 2\pi/\lambda$ is the wave number with λ as the vacuum wavelength of the radiation. Eq. (6.27) is known as the Helmholtz equation. The complex amplitude of the optical disturbance propagating in vacuum or in homogenous dielectric medium should obey such a relationship. Knowing the complex disturbance at any other point, the calculation of the complex disturbance U at any observation point in space is the central theme of scalar diffraction theory.

6.5. Numerical reconstruction by angular spectrum approach

Conventional phase retrieval methods utilize very few constraints and thus suffer from precarious uniqueness, poor accuracy and slow convergence of the phase calculation or it may require large propagation distances to use the Fresnel approximation to the wavefront which is based on the Fresnel – Kirchhoff diffraction integral [47-49]. The numerical reconstruction process can also be based on the diffraction theory, formulated in a framework called angular spectrum propagation method. Basically, this is a convolution approach available from the Fresnel-Kirchoff diffraction integral. Each of these approaches which describe the diffraction of the reconstructing wave at the micro structure of the hologram yields the complex amplitude, which contains information about the amplitude and phase.

In the case of small transparent or phase objects the angular spectrum approach will be useful since it describes the wavefront propagation over short distances from the object, whereas, Fresnel-Kirchoff integral assumes propagation distances much larger than the object dimensions. This makes compact experimental setup possible with angular spectrum propagation integral. Another advantage of this method is that it can separate out the different diffracted beams in the frequency spectrum and hence there will not be any overlap between any of the three beams in the reconstructions [50].

Fig 6.1: shows the coordinate system for reconstruction of digital holograms utilizing angular spectrum approach. For the reconstructions, the filtered angular spectrum of the hologram illuminated by the reference beam is used.

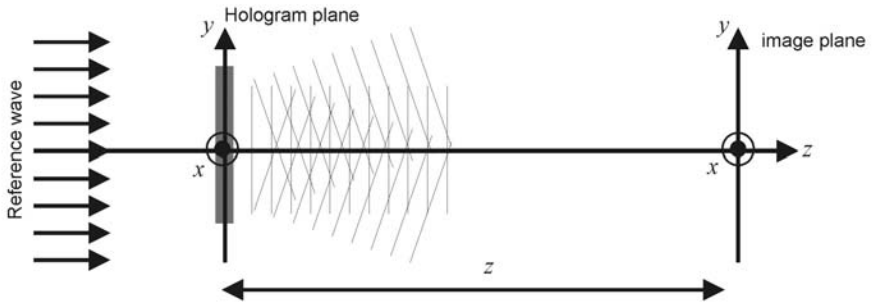

Fig.6.1: Coordinate system for digital holographic reconstruction using angular spectrum method.

If $U(x, y, 0)$ is the wave field at the hologram plane $(x, y, 0)$ then its angular spectrum is given by the Fourier transform

$$\hat{U}(f_X, f_Y; 0) = \int_{-\infty}^{\infty}\int U(x, y, 0) e^{-i[2\pi(f_X x + f_Y y)]} dx dy \tag{6.28}$$

where f_X, f_Y are the spatial frequencies in the x and y directions respectively. Filtering can be applied to the resulting spectrum so that the unwanted terms in Eq. (6.5) can be removed. By this filtering, the spectrum corresponding to the object only can be selected. Fourier transform operation decomposes the complicated function into a series of simple complex exponential functions. Hence, the inverse Fourier transform of the filtered spectrum of Eq. (6.28) provides the modified complex amplitude at $(x, y, 0)$, containing the information about only the object,

$$\overline{U}(x, y, 0) = \int_{-\infty}^{\infty}\int filt\left[\hat{U}(f_X, f_Y; 0)\right] e^{i2\pi(f_X x + f_Y y)} df_X df_Y \tag{6.29}$$

where $\overline{U}(x, y, 0)$ is the modified wave field or complex amplitude at the hologram plane and $filt\left[\hat{U}(f_X, f_Y; 0)\right]$ is the filtered angular spectrum of $U(x, y, 0)$. If the complex amplitude at a plane parallel to the (x, y) plane but at a distance z from the $(x, y, 0)$ plane is known, then the angular spectrum at this plane is,

$$\hat{U}(f_X, f_Y; z) = \int_{-\infty}^{\infty}\int U(x, y, z) e^{-i[2\pi(f_X x + f_Y y)]} dx dy \tag{6.30}$$

If the relationship between the angular spectra at (x, y, 0) and (x, y, z) can be found, the effect of wave propagation on the angular spectrum can be determined. Now, the complex amplitude at (x, y, z) can be written as,

$$U(x,y,z)=\int_{-\infty}^{\infty}\int\hat{U}(f_X,f_Y;z)e^{i2\pi(f_X x+f_Y y)}df_X\,df_Y \tag{6.31}$$

This wave field should satisfy the Helmholtz equation (Eq.6.27).

Then, we can write for a wave propagating in the z direction,

$$\frac{d^2}{dz^2}\hat{U}(f_X,f_Y;z)+k^2\left[1-\lambda^2 f_X^2-\lambda^2 f_Y^2\right]\hat{U}(f_X,f_Y;z)=0 \tag{6.32}$$

A solution to the above equation may be written as

$$\hat{U}(f_X,f_Y;z)=filt\left[\hat{U}(f_X,f_Y;0)\right]e^{ikz\sqrt{1-\lambda^2 f_X^2-\lambda^2 f_Y^2}} \tag{6.33}$$

The effect of propagation over a distance z is simply a change in the relative phases of the various components of the angular spectrum. Each plane wave components propagate at a different angle and hence travel different distances between the parallel planes in introducing relative phase delays. Inverse Fourier transform of Eq. (6.33) will yield the complex amplitude at (x, y, z),

$$U(x,y,z)=\int_{-\infty}^{\infty}\int\hat{U}(f_X,f_Y;z)e^{i2\pi(f_X x+f_Y y)}df_X\,df_Y \tag{6.34}$$

This can be computed by first Fourier transforming the wave field at the hologram plane, then filtering it and multiplying with the free space propagation function and then inverse Fourier transforming this. This can be written as,

$$U(x,y,z)=\Im^{-1}\left\{filt[\Im\{U(x,y,0)\}]e^{ikz\sqrt{1-\lambda^2 f_X^2-\lambda^2 f_Y^2}}\right\} \tag{6.35}$$

As mentioned earlier the angular spectrum method allows the frequency domain filtering, which can be used to remove the unwanted zero order or twin image components. The intensity of the wavefront is calculated from absolute square of the complex amplitude as,

$$I(x,y)=\left|U(x,y)\right|^2 \tag{6.36}$$

and phase is calculated from the angle between the complex amplitude and the real axis.

i.e., $$\varphi(x,y)=\arctan\frac{\mathrm{Im}[U(x,y)]}{\mathrm{Re}[U(x,y)]} \tag{6.37}$$

6.6. Details of the experiment

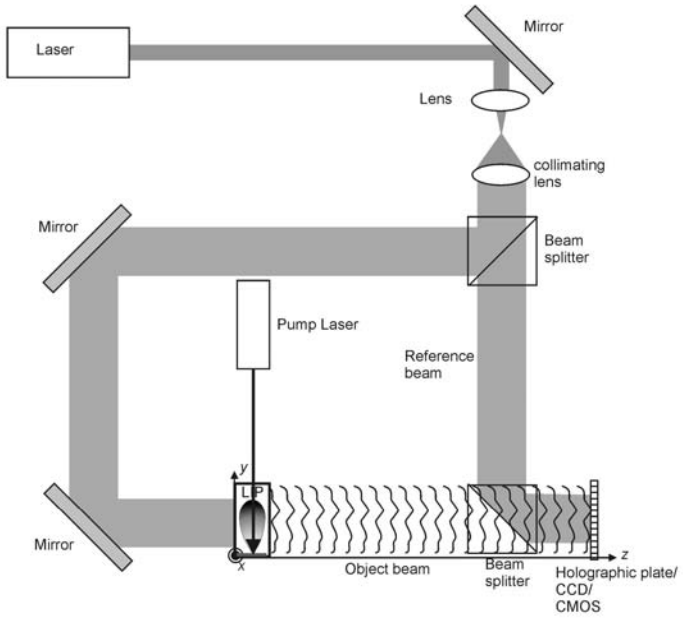

Fig 6.2: schematic diagram for the experimental setup.

The setup is very similar to a conventional Mach-Zehnder interferometer. The difference is that the resultant pattern is interpreted as a hologram, which can be reconstructed with the previously discussed theory. Two holographic exposures are made before and after the plasma formation. Density information in the plasma could be recorded only during the second exposure. But the holographic pattern recorded during the first exposure takes into account phase shifts due to windows of the plasma chamber, unwanted path length differences and other experimental irregularities.

Fig.6.2 shows the laboratory setup used for the experiment to map the phase information contained in the plasma. The laser beam from a He - Ne laser is expanded and divided into reference and object beams. The plasma is induced with a pulsed Nd:YAG laser (10ns, 275mJ) from a metallic target of Aluminium, fitted inside a vacuum chamber. The plasma serves as the transparent phase object. The chamber is at rotary vacuum (nitrogen ambient) and the irradiance at the target has been set at $10.2 GWcm^{-2}$.

The object beam passes through the plasma and illuminates the CCD while the reference beam impinges directly on the CCD. Both beams interfere and the hologram is recorded. The photo sensitive material for recording holograms must resolve the complicated intensity distributions resulting from interference between the waves scattered from the entire plasma points and the reference wave. The maximum spatial frequency which has to be resolved, is determined by the maximum angle ($\theta_{\max}$) between these waves [51]:

$$f_{\max} = \frac{2}{\lambda}\sin\left(\frac{\theta_{\max}}{2}\right) \tag{6.38}$$

where λ denotes the wavelength. According to the sampling theorem, the maximum spatial frequency that can be resolved by the CCD target is limited by the distance between neighbouring pixels. In our experiment, we have used a monochrome CMOS sensor (Lumenera, Lu 170; 100fps at 640 X 480 resolution) with square pixels of size 5.2μm, so that,

$$f_{\max} = \left(2\times 5.2\mu m\right)^{-1} \tag{6.39}$$

Therefore, the angle θ between the reference and the object wave should not be greater than 61mrad.

6.7. Retrieval of plasma phase maps from digital interferograms

The phases of the two recordings (without and with LIP) are computed individually from their respective complex amplitudes, $U_1(x, y)$ and $U_2(x, y)$ [52].

If φ_1 is the phase without plasma and φ_2 is phase in the presence of the plasma, then the phase takes values between $-\pi$ and π, the principal values of the arctan function. The interference phase (or phase difference) is now calculated directly from the digital holograms without the generation and evaluation of an interferogram:

$$\Delta\varphi = \begin{cases} \varphi_1 - \varphi_2, if, \varphi_1 \geq \varphi_2 \\ \varphi_1 - \varphi_2 + 2\pi, if, \varphi_1 < \varphi_2 \end{cases} \tag{6.40}$$

The obtained phase differences are chord integrated values or are due to the cumulative effect of the local refractive index changes occurring in the medium. Fig.6.3

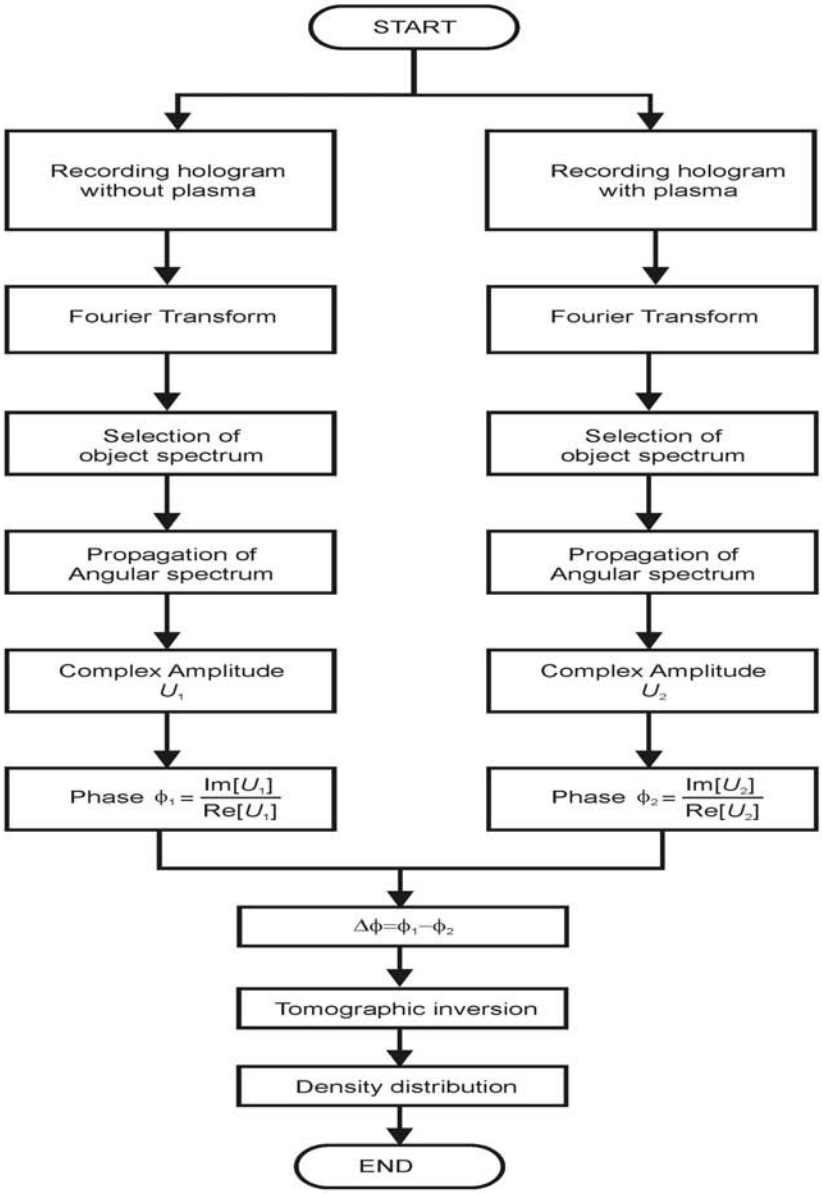

Fig 6.3: Flow chart of the wavefront reconstruction process from phase retrieval using ASP integral.

shows the detailed flow chart for phase retrieval from digital holographic interferograms using angular spectrum propagation (ASP).

The phase unwrapping procedure is coded in MATLAB. During reconstruction, the holograms act as amplitude gratings. Numerically inputted reference beam will get diffracted from the holograms in the direction of the object.. The difference between the phase information on the two holograms carries only the phase contributions from LIP. The phase obtained contains information about the optical path length at different locations on the plasma, providing us with the information about the state of the plasma.

Fig.6.4 shows the digital holograms recorded with and without the phase object (plasma). The phase maps for the two exposures are also given. The object beam is not seeing the hot plasma and passes through the periphery. This can be identified from the phase difference map which does not carry the sharp contours of a dense plasma. Hence, it is not giving proper phase information.

Fig.6.5 shows another set of digitally recorded holograms and their respective phase maps. This gives a perception of free electron density distribution in the plasma. A portion of this phase map with appreciable phase shift has been used for further data processing and reconstruction procedures.

6.8. Determination of chord-integrated electron density

The chord integrated electron density is calculated from the fringe shift using the relation,

$$f = \frac{\Delta\phi}{2\pi} = \frac{1}{2\lambda n_c}\int n_e dl \tag{6.41}$$

where f is the fringe order, n_e is the electron density and λ is the He-Ne laser wavelength.
The above equation simplifies to

$$N_e = \int n_e dl = 3.524\times10^{17} f \tag{6.42}$$

where N_e is the chord-integrated electron number density in cm^{-2} [1]. A 3D profile of the chord integrated density distribution is shown in Fig.6.6.

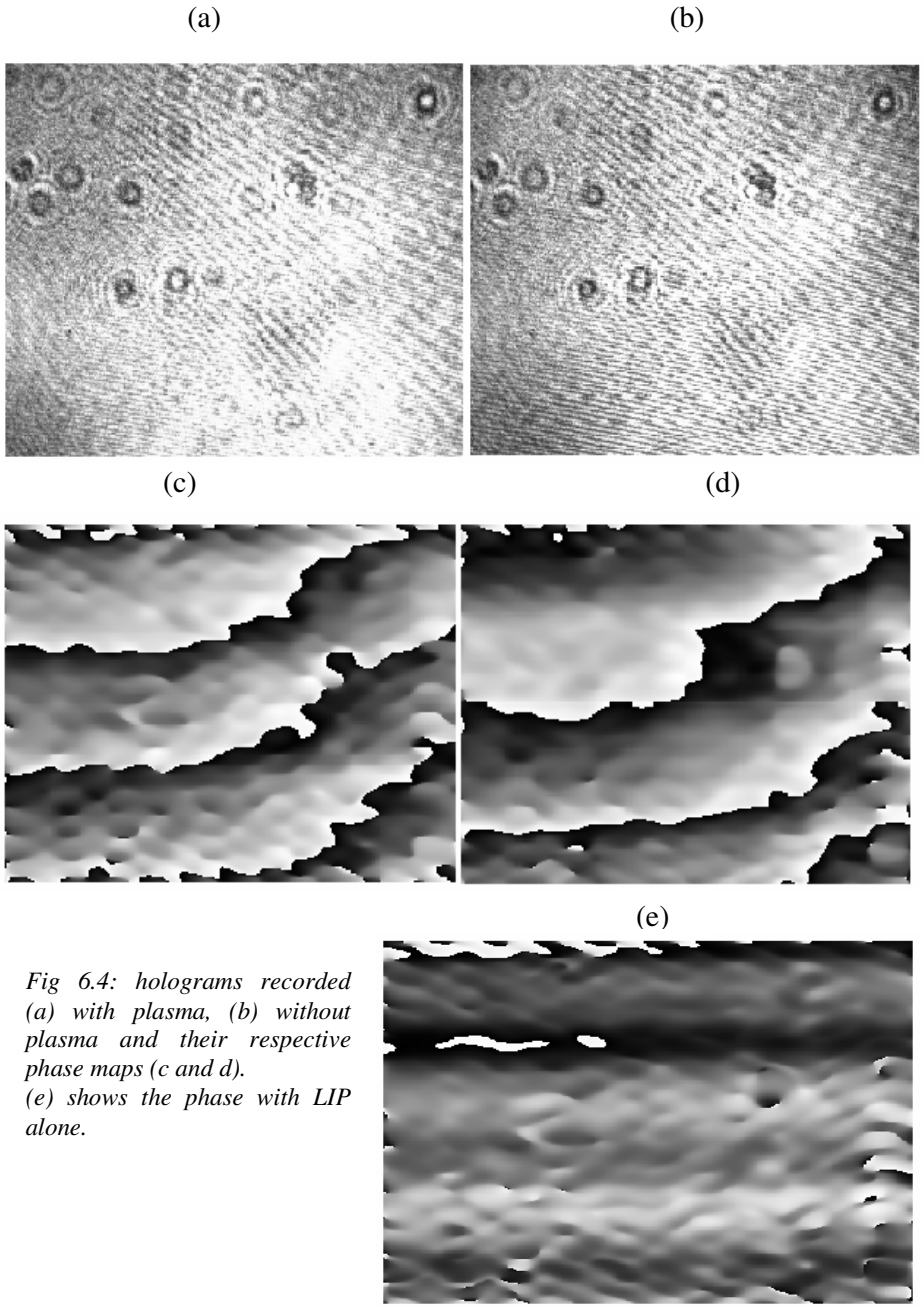

Fig 6.4: holograms recorded (a) with plasma, (b) without plasma and their respective phase maps (c and d).
(e) shows the phase with LIP alone.

(a) (b)

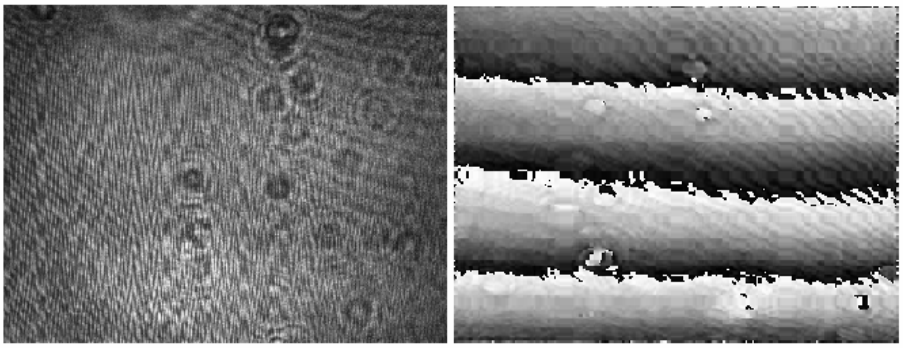

(c) (d)

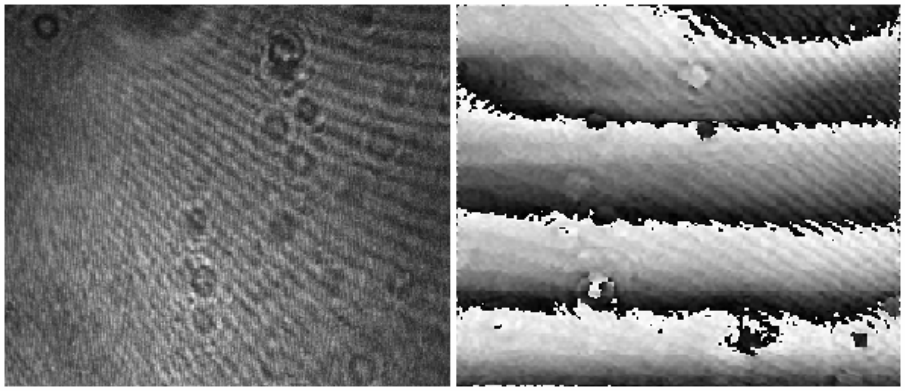

(e)

Fig 6.5: (b) is the phase map of hologram (a); (d) is the phase map of hologram c; (e) is the phase distribution contributed entirely by LIP at the irradiance 10.2 GWcm^{-2}.

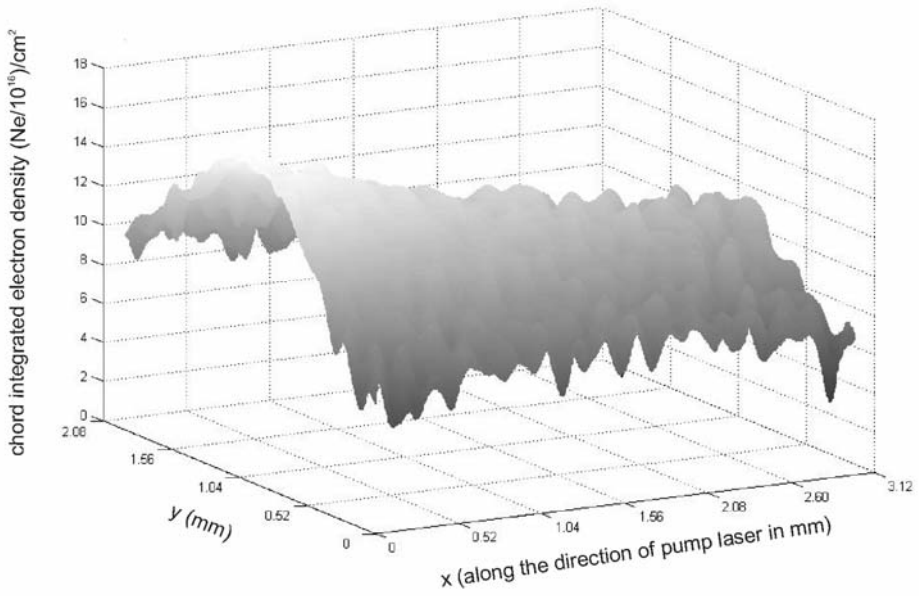

Fig 6.6: 3D profile of the chord integrated density distribution in LIP

6.9. Inversion method for determining radial electron density profile

6.9.1. Abel inversion

The chord-integrated electron number density is inverted using a discrete Abel inversion method to yield the radial electron density profile. During the initial expansion stages, the plasma is assumed to be radially symmetric so that the chord integrated number density along a given chord is given by the Abel transform equation. The local densities viewed by each chord is merely the integration of all the radial profiles $n_e(r)$ over the viewed length *x*, or

$$N_e(y) = \int n_e(r)dx. \tag{6.43}$$

Taking the advantage of the geometry of the path lengths through the plasma allows this integral to reduce to only chord *y* and radial *r* geometry.

$$N_e(y) = 2\int_y^\infty \frac{n_e(r) r dr}{\sqrt{r^2 - y^2}} \tag{6.44}$$

Inverting this relationship to solve for $n_e(r)$ requires determining the change in chord-integrated density with respect to *y*, resulting in the following equation,

$$n_e(r) = -\frac{1}{\pi}\int_r^\infty \frac{\frac{d}{dy} N_e(y)}{\sqrt{y^2 - r^2}} dy \tag{6.45}$$

The Abel inversion follows the general equation $Ln = N$, where *L* is a path length matrix, *n* the radial density and *N* the chord integrated density.

6.9.2. Discrete Abel transform

To discretize the integral at each of *I* pixels across the fringe, the plasma is modeled as I concentric cylindrical cells. The number density across shell *i* is assumed to be constant from r_i to r_{i+1}. the path length geometry and the shell model used in obtaining radial electron density profile from chord integrated electron density values is given in Fig 6.7. The chord integrated electron number density at y corresponding to radius r_i depends on the density at shell *i* and all the shells outside it [53]:

$$N_{ei} = 2\sum_{k=i}^{I-1} n_{ek} \int_{r_k}^{r_{k+1}} \frac{r dr}{\left(r^2 - r_i^2\right)^{1/2}} \tag{6.46}$$

where n_{ek} is the electron number density throughout each shell k, from $k = i$ to $k = I$-1. Simplifying and substituting $r_i = i\Delta r$, where, Δr is the shell width, which is the radial distance between two shells,

$$N_{ei} = 2\Delta r \sum_{k=i}^{I-1} n_{ek} A_{ki} \tag{6.47}$$

The co-efficients given as,

$$A_{ki} = \left\{ \left((k+1)^2 - i^2\right)^{1/2} - \left(k^2 - i^2\right)^{1/2} \right\} \tag{6.48}$$

are half the path lengths through each shell, normalized by Δr.

The above given discrete Abel transform can be used to arrive at the discrete Abel inversion formula,

$$\sum_{k=i}^{I-1} n_{ek} A_{ki} = \frac{1}{2\Delta r} N_{ei} \tag{6.49}$$

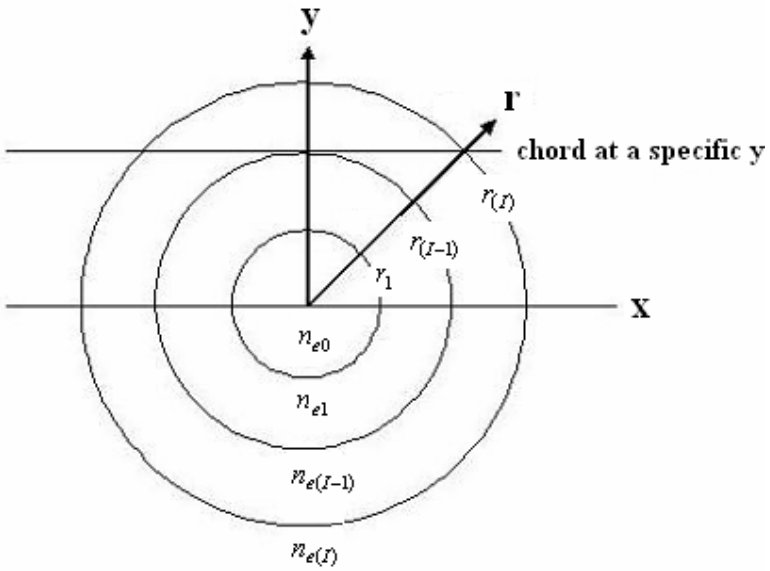

Fig 6.7: Shell model used to obtain the radial electron density profile from the chord-integrated density using discrete Abel inversion method.

6.9.3. Discrete Abel inversion method

The Abel inversion method is equivalent to the following process:

The electron density of the outermost shell (shell I) is calculated by dividing the chord integrated density at the first chord (outermost chord) by the path length through the shell situated at the corresponding y:

$$n_{e(I-1)} = \frac{1}{A_{(I-1)(I-1)}} \frac{1}{2\Delta r} N_{e(I-1)} \tag{6.50}$$

The electron density of the second outermost shell (shell I-1) is calculated in a similar manner using chord integrated density at the second chord, except there are two shells involved. The contribution of the outermost shell can be calculated, since the electon density and the path length through the outermost shell are known. This contribution is then subtracted from the chord integrated density to yield the

chord integrated density due to the second outermost shell alone. This value is divided by the path length through the second outermost shell to yield the electron density of that shell:

$$n_{e(I-2)} = \frac{1}{A_{(I-2)(I-2)}}\left[\frac{1}{2\Delta r}N_{e(I-2)} - A_{(I-1)(I-2)}n_{e(I-1)}\right] \tag{6.51}$$

This process may be repeated, working inward, until the innermost shell is reached and the electron density at any shell can be determined [54, 55]. The interferograms contain enough information to produce two radial density profiles by this method: one is based on the lower part of the interferogram, and the other is based on the upper part.

6.10. Reconstruction of radial density profiles from plasma phase maps

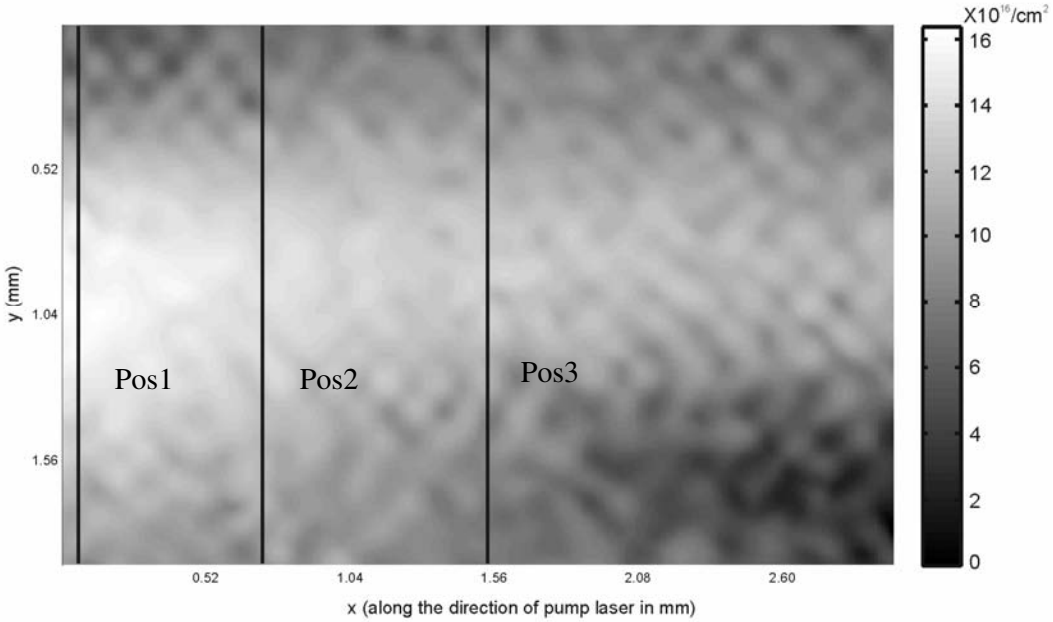

Fig 6.8: Chord integrated density distribution. Abel inversion is done at the three marked positions.

Abel inversion is performed at three different positions in the 2D chord integrated electron density distribution as shown in Fig. 6.8.

The chord integrated density profiles as well as the electron density distributions at the three positions shown in Fig. 6.8 are shown in Fig. 6.9 to 6.11.

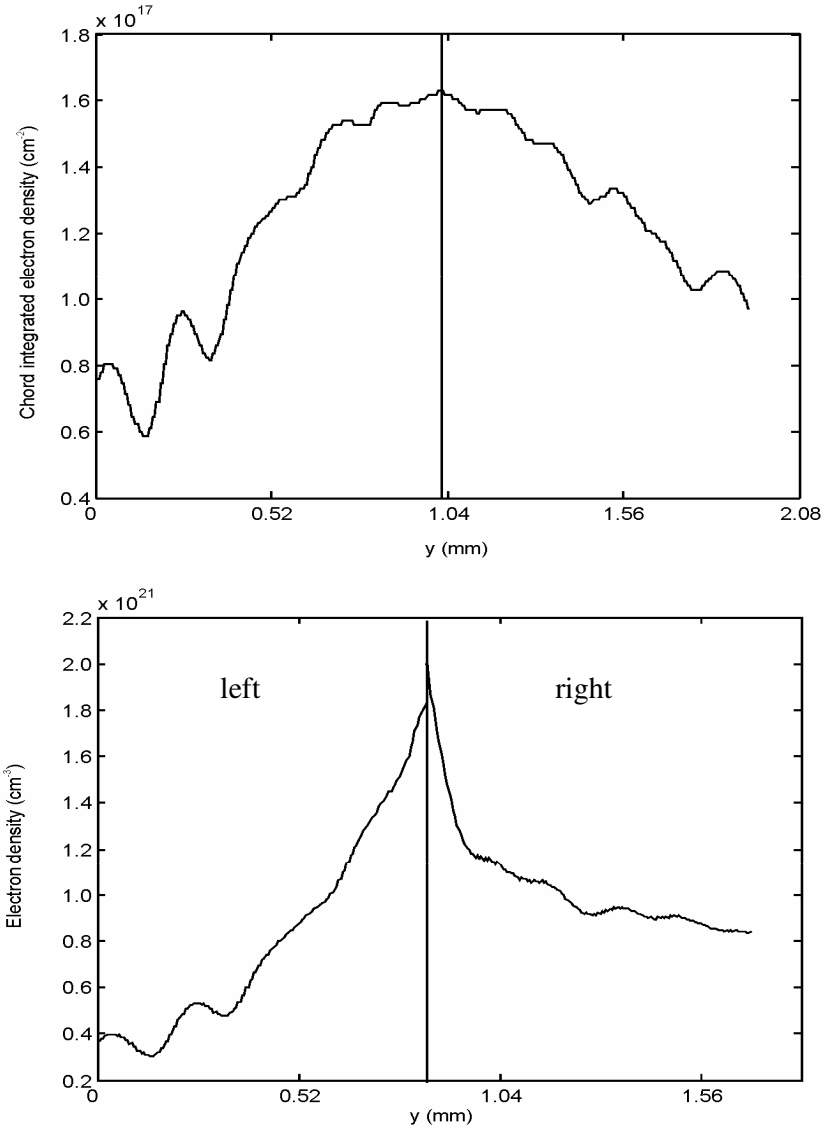

Fig. 6.9: Chord integrated as well as local electron density distribution for pos1.

The left part of the chord integrated density profile is used to find the local density profile (or electron density) on the left side and right part on the chord integrated curve for finding the electron density on the right side. The line along which the distribution is divided is also shown.

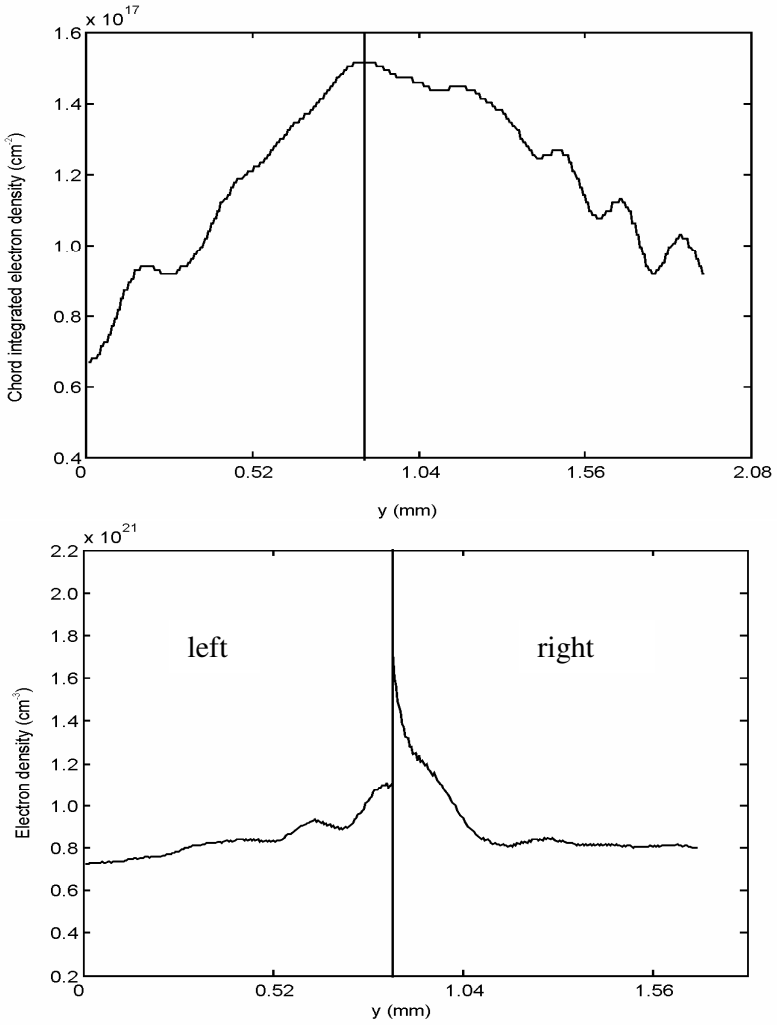

Fig. 6.10: Chord integrated as well as local electron density distribution for pos2.

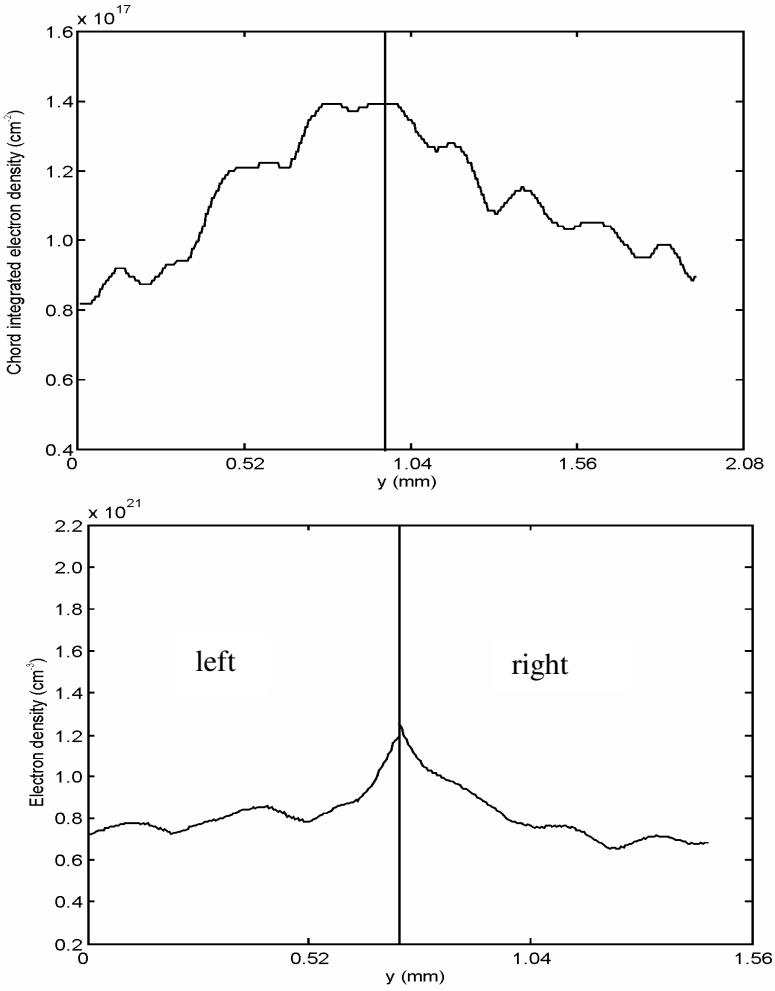

Fig. 6.11: Chord integrated as well as local electron density distributions for pos3.

The local electron density at the plasma centre i.e., pos1 (close to the target), is 2 x 10^{21}cm^{-3} whereas, its value is 1.3 x 10^{21}cm^{-3} at pos3 (1.5mm away from the target). The range of time integrated electron density variation along the respective cross section (at pos1, pos2 and pos3) of the expanding plume decreases, as we go from Fig.6.9 to Fig.6.11. This observation was apparent from the spectroscopic density evaluations presented in section 2.3.2, 2.4.2 and 2.5.2.

6.11. Summary

The phase distribution in laser produced plasma has been obtained from digitally recorded interferograms. The phase maps are reduced to chord integrated density maps and the chord integrated electron density values at different points are plotted. The local electron density values are evaluated and the radial electron density profiles are mapped by inverting the chord integrated data using a discrete Abel inversion method.

6.12. References

[1] IH Hutchinson, Principles of plasma diagnostics (Cambridge, 2002)

[2] K Muraoka, M Maeda, Laser-aided diagnostics of plasmas and gases, (IOP publishers, 1999)

[3] U Schnars, W Juptner, Appl. Opt. 33 179 (1994)

[4] U Schnars, W Juptner, Meas. Sci. Technol. 13 R85 (2002)

[5] D Gabor, Nature 161 777 (1948)

[6] Gabor D, Proc. R. Soc. 197 454 (1949)

[7] Gabor D, Proc. Phys. Soc. 64 449 (1951)

[8] Powell R L and Stetson K A, J. Opt. Soc. Am. 55 1593 (1965)

[9] Stetson K A and Powell R L, J. Opt. Soc. Am. 55 1694 (1965)

[10] Lee W H, Prog. Opt. 16 120 (1978)

[11] Bryngdahl O and Wyrowski F, Prog. Opt. 28 1 (1990)

[12] Kronrod M A, Yaroslavski L P and Merzlyakov N S, Sov. Phys.–Tech. Phys. 17 329 (1972)

[13] Kronrod M A, Merzlyakov N S and Yaroslavski L P, Sov. Phys.–Tech. Phys. 17 333 (1972)

[14] Yaroslavskii L P and Merzlyakov N S, Methods of Digital Holography (New York: Consultants Bureau, 1980)

[15] Onural L and Scott P D, Opt. Eng. 26 1124 (1987)

[16] Liu G and Scott P D, J. Opt. Soc. Am. A 4 159 (1987)

[17] Onural L and Ozgen M T, J. Opt. Soc. Am. A 9 252 (1992)

[18] Haddad W, Cullen D, Solem J C, Longworth J M, Mc Pherson A, Boyer K and Rhodes C K, Appl. Opt. 31 4973 (1992)

[19] Schnars U and Juptner W, Proc. 2nd Int. Workshop on Automatic Processing of Fringe Patterns ed W Juptner and W Osten (Berlin: Akademie, 1993) pp 115–20

[20] Schnars U J, Opt. Soc. Am. A 11 2011 (1994)

[21] Schnars U, Kreis T and Juptner W, Opt. Eng. 35 977 (1996)

[22] Schnars U, Kreis T and Juptner W, Proc. SPIE 2544 57 (1995)

[23] Pedrini G, Fr¨oning P, Fessler H and Tiziani H J, Appl. Opt. 37 6262 (1998)

[24] Cuche E, Bevilacqua F and Depeursinge C, Opt. Lett. 24 291 (1999)

[25] Pedrini G, Schedin S and Tiziani H, Opt. Commun. 171 29 (1999)

[26] Wagner C, Seebacher S, OstenW and Juptner W, Appl. Opt. 38 4812 (1999)

[27] Cuche E, Marquet P and Depeusinge C, Appl. Opt. 39 4070 (2000)

[28] Papp Z and Janos K, Proc. SPIE 4416 112 (2001)

[29] Xu L, Miao J and Asundi A, Opt. Eng. 39 3214 (2000)

[30] Kreis T and Juptner W, Proc. 3rd Int. Workshop on Automatic Processing of Fringe Patterns ed W Juptner and W Osten (Berlin: Akademie, 1997) pp 353–63

[31] Kreis T and Juptner W, Opt. Eng. 36 2357 (1997)

[32] Kreis T, Juptner W and Geldmacher J, Proc. SPIE 3407 169 (1998)

[33] Kreis T, Juptner W and Geldmacher J, Proc. SPIE 3478 45 (1998)

[34] Kim S, Lee B and Kim E, Appl. Opt. 36 4784 (1997)

[35] Lai S, Kemper B and von Bally G, Opt. Commun. 169 37 (1999)

[36] Yang S, Xie X, Thuo Y and Jia C, Opt. Commun. 159 29 (1999)

[37] Grilli S, Ferraro P, De Nicola S, Finizio A, Pierattini G and Meucci R, Opt. Express 9 294 (2001)

[38] Javidi B and Nomura T, Opt. Lett. 25 28 (2000)

[39] Tajahuerce E and Javidi B, Appl. Opt. 39 6595 (2000)

[40] Kebbel V, Grubert B, Hartmann H J, JuptnerW and Schnars U, Proc. 49th Int. Astronautical Cong. (Melbourne) (Paris: IAF) Paper no. IAF-98-J.5.03 (1998)

[41] Osten W, Baumbach T, Seebacher S and Juptner W, Proc. 4th Int. Workshop on Automatic Processing of Fringe Patterns ed W Juptner and W Osten (Berlin: Akademie, 2001) pp 373–82

[42] Harriharan P, Optical Holography (Cambridge: Cambridge University Press, 1984)

[43] Kreis T, Holographic Interferometry (Berlin: Akademie, 1996)

[44] Schnars U and Juptner W, Appl. Opt. 33 179 1994

[45] Martin centurion, Ye Pu, Zhiwen Liu and Demetri Psaltis, Theodor W Hansch, Optics Letters, 29 7 (2004)

[46] J W Goodman, Introduction to Fourier Optics (McGraw-Hill, New York, 1996)

[47] J R Fienup, Appl. Opt. 21 2758 (1982)

[48] E. Kolenovic, J. Opt. Soc. Am. A. 22 899 (2005)

[49] P Cloetens, W Ludwig, J Baruchel, D Van Dyck, J Van Landyut, J P Guigay, M Schlenker, Appl. Phys. Lett. 75 2912 (1999)

[50] M K Kim, L Yu, C J Mann, J. Opt. A: Pure Appl. Opt. 8 S518 (2006)

[51] Y. I. Ostrovsky, M. M. Butusov, and G. V. Strovskaya, Interferometry by Holography (Springer-Verlag, New York, 1980) Chap. 1, p. 11.

[52] Arun Anand, Vani K Chhaniwal and C S Narayanamurthy, Applied Optics 45 (5) 1 (2006)

[53] S L Jackson and U Shumlak, Rev. Sci. Instrum. 77 083502 (200651)

[54] Stuart Lee Jackson, Holographic Interferometry on the ZaP Flow Z-Pinch (M.Sc. thesis, department of aeronautics and astronautics, University of Washington, 2003)

[55] Adam Matthew Madson, Optical Tomography of the ZaP Flow Z-Pinch Plasma (M.Sc. thesis, department of aeronautics and astronautics, University of Washington, 2005)

CHAPTER 7

Concluding remarks and some outlooks

7.1. Conclusions

Laser induced plasma (LIP) emissions from some metal oxide targets were studied with corresponding metal targets of pure quality as a reference. Atomic emissions in the visible region were used in the spectroscopic procedures of LIP characterization. The studies were meant to throw light into LIP dynamics and they provided many experimental results which improved the general awareness of plasma state.

When target materials were photo-ablated with an energetically suitable laser pulse, they developed electric charges in them. An electrical signal which was delivered from the target served as an alternative probe signal for the diagnostics of LIP and to track different charged states in the plasma. The signal showed a double peak distribution with positive polarity and a modified time of flight with various voltage levels of a given polarity. When the ambient pressure was decreased, the multiple structure of the peak became clearer. The expansion dynamics of LIP in magnetic field were also investigated by monitoring the voltage transients generated at the target. The signal was analyzed in the presence and absence of magnetic field to investigate on the plasma responses to the field. The field confined the plasma and the charged particles entered into newly defined territories, with modified trajectories and kinetics. Signs of a transverse expansion were evident. An increased plume lifetime was observed in the presence of the field.

Another set of experiments were presented to investigate the behaviour of LIP under the influence of a perpendicular magnetic field. A pulsed magnetic field was applied to plasma using a Helmholtz coil. The plasma was spectroscopically examined and found that the magnetic field does not much affect the arrival time distribution of the ejected species but modulated the intensity of visible radiation. Neutrals in LIP were greatly affected by the recombination behavior induced by the field and the modified collisions in the plasma.

The technical aspects of tomographic imaging of LIP were investigated using pixel method. This is a powerful tool which can provide detailed information that are useful in optimizing experimental setups for different plasma applications and to improve their analytical performance.

The phase distribution in LIP was obtained from digitally recorded interferograms, using the methods of digital holographic interferometry (DHI) and the angular spectrum propagation approach. The phase maps were reduced to chord integrated density maps and the chord integrated electron density values at different spatial points were plotted. The local electron density values were evaluated and the mapping of radial electron density profiles was done, by inverting the chord integrated data using a discrete Abel inversion method.

7.2. Future prospects

The data derived from spectroscopic methods are reliable and the validity of the assumptions made during the measurements on LIP has been verified. Besides this, spectroscopic imaging and modelled data can give extended support to test and verify the inferences made about plasma dynamics. Both laser induced fluorescence (LIF) and optical emission spectroscopic techniques can be coupled to study LIP formation and propagation. Different ion densities in plasmas can be measured by LIF imaging spectroscopy. In this, tunable laser pulses from an optical parametric oscillator (OPO) are injected into plasmas and the wavelength is tuned to excite plasma ions at different charge states. A charge coupled camera with a gated image intensifier can be used to take the images of fluorescence. Interference filters will separate the fluorescence from stray lights and self emissions of plasmas. LIF can be used as a nondestructive technique to measure the ion velocity distribution. Such diagnostic steps can overcome the existing sensitivity limitations**,** improve the time and space resolution, and simplify the modelling assumptions.

Combining femtosecond pump–probe techniques with optical microscopy, laser induced breakdown in optically transparent solids can be studied with high temporal and spatial resolution. A weaker probe pulse at normal incidence illuminates the surface region overlapping the area of the pump pulse. A microscope objective will pick up the reflected probe light and produce an image of the surface on a digital CCD camera.

With all the measurements and the experimental results presented, the self derived signal from plasma source target is still unexplored, compared to the complexity of the information underlying it. It seems that the diagnostic method of probe signals derived from plasma source target, when implemented together with suitably designed Langmuir probes can throw more light on the hidden aspects of this technique. The electron and ion currents from LIP target can be correctly calibrated with a series of properly arranged Langmuir probes.

A full understanding of the magnetic field effects on plasma dynamics can be effected if the applied variable field is increased to higher values, in which plasma is confined to points near the target. ICCD imaging of field confinements are progressing in the lab as a second phase of our study.

Pixel method for LIP tomography can be improved if light can be collected from more viewing chords at different positions with respect to the normal expansion of the plume. An interfaced photodiode array is the best candidate for the light collection. Monochromatic light collection from suitable wavelength regions, using optical filters, can give wavelength dependent emissivity maps. Time resolved density maps can be obtained from DHI, if the probe beam is from a pulsed laser having good coherence length, instead of a continuous laser beam. If the pulse has picosecond or femtosecond pulse duration, a dynamic picture of the time evolution of plasma density can be derived. A femtosecond pulse has the capability to capture a sequence of frames (from the evolution of LIP) in a single experiment.

When two expanding plasmas collide, several interactions can arise. These interactions may be either of collisionless type, in which case collective plasma effects should occur or, in contrast they may be collision dominated. For example, considering two extreme cases where the ion-ion mean free path is either bigger or smaller than the typical dimension of the system, we can expect two different behaviours to occur during the interaction of the two plasma plumes. In the first case, the expanding plasma plumes should interpenetrate and therefore the heating processes should be mostly driven by binary collisions between the species. In the second case a quite different scenario is expected to occur, once the two plasmas collide. In this case, the region of interpenetration should be relatively small and the two plumes will decelerate rapidly and stagnate. A stationary plasma should then be formed at the interface, if the translational

(kinetic) energy of the plasma streams is converted into thermal energy. This localized heated region is frequently referred as the stagnation layer. This stagnation layer emits strongly in the visible region of the spectrum, for some hundreds of nanoseconds. The time and space evolution of the stagnation layer using optical imaging and spectroscopy is another direction to the future studies. Laser induced colliding plasmas find potentially attractive applications in the field of x-ray lasers, in stimulated Raman scattering experiments, and they are of relevance for the design of inertial confinement fusion (ICF) reactors.